

https://dspace.org/

High temperature casting of pyrophyllite using calcium oxide and zirconia additives and subsequent comparison with cast basalt tiles

Marongwe, Tichaona Nyasha

2021

https://hdl.handle.net/10539/35756

Downloaded from a DSpace repository. https://dspace.org/

HIGH TEMPERATURE CASTING OF PYROPHYLLITE USING CALCIUM OXIDE AND ZIRCONIA ADDITIVES AND SUBSEQUENT COMPARISON WITH CAST BASALT TILES

Prepared by

Tichaona Nyasha Marongwe

A dissertation submitted to the Faculty of Engineering and the Built Environment, University of the Witwatersrand, Johannesburg, in fulfilment of the requirements for the degree of Master of Science in Engineering.

18 January 2021

DECLARATION

I declare that this dissertation is my own unaided work. It is being submitted for the degree of Master of Science in Engineering to the University of the Witwatersrand, Johannesburg. It has not been submitted before for any degree or examination to any other university.



Tichaona Nyasha Marongwe

18th day of January in the year 2021

ABSTRACT

A fundamental part of the petrurgy industry is the use of materials such as basalt, which have considerably low melting points as compared to other alumino-silicates. These materials, however, are available in some regions but scarce in others including South Africa. Pyrophyllite ($Al_2Si_4O_{10}(OH)_2$), a material abundant in South Africa, has the potential to be a substitute for casting of basalt due to its favourable material properties. From the ternary phase diagrams of the SiO_2-Al_2O_3-CaO system, calcium oxide additives formed from decomposed calcium carbonate were used to lower the melting point of pyrophyllite ($Al_2Si_4O_{10}(OH)_2$) powder. The mixed powders were successfully molten at a temperature of 1400°C, approximately 350°C lower than the melting point of pyrophyllite. The molten powders were cast into pyrophyllite sand moulds and produced amorphous samples with fracture toughness values comparable to cast basalt but with a lower hardness. Heat treating the samples at 900°C for phase separation and 1040°C to crystallise them produced samples with hardness and fracture toughness values comparable to cast basalt. Using an additional 1 wt. % yttria-stabilized zirconia as a nucleating agent, crystallised samples of pyrophyllite with comparable hardness and fracture toughness to the cast basalt were produced using a single heat treatment step at 1100°C. XRD analysis indicated gehlenite was the major phase formed, together with phases of anorthite and wollastonite. This final material had a density of 2,83g/cm³ with hardness and fracture toughness values of 6,18 GPa and 1.12 MPa.$m^{1/2}$ respectively and therefore, in conclusion, crystallised samples of pyrophyllite with comparable hardness and fracture toughness to the cast basalt were indeed produced using calcium oxide and zirconia additives. In addition to this further work may be done to explore additional additives to eliminate the nucleation step entirely and produce crystallised samples as cast.

ACKNOWLEDGEMENTS

True to the spirit of ubuntu, ‘it takes a village’.

Firstly, I would like to thank my supervisors, Prof I Sigalas and Dr D J Whitefield, for their guidance, suggestions, assistance and encouragement in completion of this research and dissertation.

Many thanks to all my colleagues and friends in the entire university family for helping to create an atmosphere that actively promotes the pursuit of knowledge.

Last, but certainly not least, I would like to thank my family for their sacrifices, support, encouragement, patience and love throughout this amazing journey. Your love is what motivated me constantly and I could never have done this without you. Thank you so much.

Dedicated to

my mother

TABLE OF CONTENTS

DECLARATION ..... *ii*

ABSTRACT ..... *iii*

ACKNOWLEDGEMENTS ..... *iv*

LIST OF FIGURES ..... *ix*

LIST OF TABLES ..... *xii*

NOMENCLATURE ..... *xiii*

CHAPTER 1: INTRODUCTION *1*

1.1. Motivation **1**

1.2. Problem statement **2**

1.3. Research objectives **2**

1.4. Scope of research **2**

1.5. Structure of Dissertation **3**

CHAPTER 2: LITERATURE REVIEW *4*

2.1. Wear-resistant parts **4**

2.2. Petrurgy **6**

2.2.1. Basalt casting 7

2.2.2. Basalt production 8

2.2.3. Basalt applications 9

2.3. Pyrophyllite **10**

2.3.1. Pyrophyllite admixtures 12

2.4. CaO and Na_2O **16**

2.5. Sand Casting **17**

2.5.1. Method of sand casting 18

2.5.2. Sand and mould characteristics 19

2.5.3. Melting of raw materials 21
2.5.4. Crystallisation and glass ceramics 22

CHAPTER 3: METHODOLOGY 24

3.1. Materials and chemicals 24

3.2. Facilities and machinery used 25

3.3. Material Preparation 25

3.3.1. Powder property measurement and composition 25
3.3.2. Compaction and mixing of powders 27
3.3.3. Thermogravimetric Analysis 27

3.4. Casting 28

3.4.1. Casting apparatus 28
3.4.2. Casting bed 29
3.4.3. Quenching process and recrystallization 30

3.5. Material Characterisation 32

3.5.1. Particle size analysis 32
3.5.2. Density 33
3.5.3. Cutting of Samples 34
3.5.4. XRD 34
3.5.5. SEM 34

3.6. Mechanical properties 35

3.6.1. Hardness and fracture toughness 35

CHAPTER 4: RESULTS 36

4.1. Differential thermal analysis / Thermogravimetric analysis (DTA-TG) 36

4.2. Sample casting and crystallography 41

4.3. Mechanical Tests 46

4.3.1. Yttria-stabilised zirconia 48

4.4. SEM 52

4.5. Mechanical properties 64

CHAPTER 5: DISCUSSION 67

5.1. Properties of pyrophyllite raw material 67

5.1.1. Thermal behaviour 67
5.1.2. Effects of admixtures on thermal behaviour 68
5.2. Phase and Microstructural analysis 69
5.2.1. XRD Analysis 69
5.2.2. SEM analysis 76
5.3. Mechanical Properties 79
CHAPTER 6: CONCLUSION 86
CHAPTER 7: REFERENCES 88

LIST OF FIGURES

Figure 2.1: Pyrophyllite crystal structure ((Gaidoumi, et al., 2019)). 10
Figure 2.2: Diagram showing the different required starting forms of pyrophyllite for different desired output properties (Bentayeb, et al., 2003). 11
Figure 2.3: Eutectic point of a two component mixture (Nichols, 2019). 13
Figure 2.4: Binary phase diagram of a generic two-component system based on different compositions (Nichols, 2019). 13
Figure 2.5: Binary phase diagram of the SiO_2-Al_2O_3 system (Li, et al., 1999). 14
Figure 2.6: Ternary phase diagram of the SiO_2-Al_2O_3-CaO system (Chunlin, 2015). 15
Figure 2.7: Ternary phase diagram of the SiO_2-Al_2O_3-Na_2O system (Chartrand & Pelton, 1999). 16
Figure 2.8: Diagram showing sand casting process (Groover, 2011). 19
Figure 3.1: Ternary phase diagram of the SiO_2-Al_2O_3-CaO system (Chunlin, 2015). 26
Figure 3.2: Ternary phase diagram of the SiO_2-Al_2O_3-Na_2O system (Chartrand & Pelton, 1999). 26
Figure 3.3: Setup of melting crucible with ceramic blanket. 29
Figure 3.4: Pyrophyllite casting bed. 30
Figure 3.5: Casting of melted pyrophyllite. 30
Figure 3.6: Cast samples cooling in pyrophyllite bed. 31
Figure 3.7: Measurement of cracking around hardness indentation (Rocha-Rangel, 2011). 35
Figure 4.1: DTA-TG curves of pure pyrophyllite. 36
Figure 4.2: DTA-TG curves of pyrophyllite mixed with 48 wt. % calcium carbonate. 38
Figure 4.3: DTA-TG curves of pyrophyllite mixed with 39 wt. % calcium carbonate. 39
Figure 4.4: DTA-TG curves of pyrophyllite mixed with 15 wt. % sodium carbonate. 40
Figure 4.5: DTA-TG curves of pyrophyllite mixed with 19 wt. % sodium carbonate. 41
Figure 4.6: a) Placement of pyrophyllite mixture in crucible, b) pyrophyllite sand casting mould. 42
Figure 4.7: Molten samples in casting bed. 43

Figure 4.8: a) Cast sample being held against light b) Cast sample placed on pyrophyllite casting bed. 43
Figure 4.9: a) XRD pattern of cast pyrophyllite sample, b) SEM backscatter image of cast pyrophyllite. 45
Figure 4.10: Expected composition vs analysed composition of samples with CaO additives 46
Figure 4.11: Crystallized cast pyrophyllite. 47
Figure 4.12: XRD pattern of crystallized cast pyrophyllite. 48
Figure 4.13: XRD pattern of crystallized cast pyrophyllite a) without zirconia and with added zirconia of b) 1 wt. % c) 3 wt. % d) 5 wt. % e) 8 wt. %. 51
Figure 4.14: SEM Micrographs of crystallized cast pyrophyllite at a) low magnification b) high magnification. 53
Figure 4.15: Overall EDX analysis of crystallized cast pyrophyllite. 54
Figure 4.16: EDX analysis of crystallized cast pyrophyllite at a) point scan of dark grey phase b) point scan of light grey phase. 55
Figure 4.17: SEM Micrographs of cast pyrophyllite crystallized with 1% zirconia at a) low magnification b) high magnification. 56
Figure 4.18: EDX analysis of crystallized cast pyrophyllite with 1% zirconia at a) point scan of bright spot b) area scan of dark grey phase c) area scan of light grey phase.... 57
Figure 4.19: a) SEM backscatter of cast pyrophyllite with 10% zirconia b) XRD pattern of cast pyrophyllite sample 10% zirconia. 58
Figure 4.20: SEM Micrographs of crystallized cast pyrophyllite with added zirconia of ..
a) 1 wt. %, b) 3 wt. % and c) 5 wt. %. 59
Figure 4.21: SEM Micrographs of crystallized cast pyrophyllite with added zirconia of ..
a) 1 wt. %, b) 3 wt. % and c) 5 wt. %. 60
Figure 4.22: SEM Micrographs of crystallized cast pyrophyllite with 1% added zirconia heated at 1100°C for a) 2hr, b) 3 hr and c) 4hr. 62
Figure 4.23: a) XRD pattern of crystallized cast pyrophyllite with added 1% zirconia and heated at 1100°C for a) 2hr, b) 3hr and c) 4hr. 63

Figure 5.1: Ternary phase diagrams of the CAS system at a)1300C isotherm (Ball, et al., 1993) b) three phase equilibria (Mao, et al., 2006). An/Ano – anorthite; Pse-Wol/Wol – wollastonite; Geh/Mel gehlenite; Cor/Crn – corundum; Cri – cristobalite; Ran/Ra – rankinite; Mul – mullite; Tri/Trd – tridymite; Hat – hatrurite. 72
Figure 5.2: DTA profiles of glass samples doped with 6 wt. % zirconia (SZ6); 6, 9 & 22 wt. % titanium oxide (ST6, ST9 & ST22); 6, 9 & 12 wt. % calcium fluoride (SF6, SF9 & SF12) (Banijamali, et al., 2009). 75
Figure 5.3: Ternary phase diagram of the CaO-SiO_2-ZrO_2 system (Mirhadi & Mehdikhani, 2011). 78
Figure 5.4: a) Hardness and b) Fracture toughness of cast pyrophyllite samples (without zirconia) before and after crystallisation. 80
Figure 5.5: Hardness values of cast samples crystallized with added zirconia. 81
Figure 5.6: Fracture toughness of cast samples crystallized with added zirconia. 82
Figure 5.7: SEM Micrographs of indentations made to crystallized cast pyrophyllite with added zirconia of a) 1 wt. %, b) 3 wt. %, c) 5 wt. % and d) 10 wt. %. 84
Figure 5.8: Mechanical properties of crystallized cast pyrophyllite with added 1% zirconia and heated at 1100°C from 2 to 4 hours. 85

LIST OF TABLES

Table 2.1: Chemical composition of industrial basalt (weight %), (Kopecky, 1965). 8

Table 2.2: Materials used for sand casting moulds (Campbell, 1984). 19

Table 3.1: Table of materials used in research and source. 24

Table 3.2: Table of facilities used in research and location. 25

Table 3.3: Compositions of pyrophyllite with $CaCO_3$ or Na_2CO_3 additives. 27

Table 3.4: Compositions of pyrophyllite with $CaCO_3$ and Zirconia additives. 32

Table 3.5: Densities and refractive indices of powders. 33

Table 4.1: Compositions of pyrophyllite with $CaCO_3$ or Na_2CO_3 additives. 37

Table 4.2: Material properties of cast samples vs basalt. 46

Table 4.3: Crystallization matrix. 49

Table 4.4: Material properties of cast samples vs basalt. 64

Table 4.5: Material properties of cast samples crystallized with added zirconia. 65

Table 4.6: Material properties of cast samples crystallized with 1% added zirconia at 1100°C with increasing time. 66

Table 5.1: Calculation of weight loss due to dehydroxilation reaction. 68

NOMENCLATURE

°C	Degrees Celsius
Al_2O_3	Alumina
$Al_2Si_4O_{10}(OH)_2$	Pyrophyllite
$CaCO_3$	Calcium Carbonate
CaO	Calcium Oxide
CAS	$CaO\text{-}Al_2O_3\text{-}SiO_2$ – Calcium oxide alumino-silicate
DTA	Differential thermal analysis
Na_2CO_3	Sodium Carbonate
Na_2O	Sodium Oxide
SEM	Scanning electron microscopy
SiO_2	Silica
$SiO_2\text{-}Al_2O_3$	Alumino-silicate
TG/TGA	Thermogravimetric analysis
XRD	X-Ray Diffraction analysis

CHAPTER 1: INTRODUCTION

1.1. Motivation

Petrurgy is the processing of non-metallic ores by melting and casting. It has been used for centuries to produce various essential products including pipes, casings, tiles and linings (Kopecky, 1965). These cast materials are of significant importance due to their primarily uses as electrical insulators, chemically resistant castings and, to a lesser extent, abrasion-resistant materials.

A fundamental part of the petrurgy industry is the use of material such as basalt, which have considerably low melting points as compared to other alumino-silicates. Raw materials traditionally used in the casting industry such as basalt, however, are available in some regions but scarce in others including South Africa.

Pyrophyllite ($Al_2Si_4O_{10}(OH)_2$), a material abundant in South Africa, has the potential to be a substitute for casting of basalt due to its favourable material properties. It has a relatively high melting point of approximately 1750°C (Bentayeb, et al., 2003), when compared to materials such as basalt which melts at 1350°C. The higher melting point of pyrophyllite had previously proven to be a limiting factor in the viability of its casting.

Phase diagrams of pyrophyllite suggest that the melting point of pyrophyllite could be lowered by using calcium oxide (CaO) or sodium oxide (Na_2O) as additives (Chunlin, 2015) (Chartrand & Pelton, 1999). Hence, the microstructural evolution and mechanical properties of calcium carbonate and sodium carbonate doped pyrophyllite prepared by high temperature casting were further investigated in this research.

1.2. Problem statement

Despite pyrophyllite having comparable mechanical properties to basalt, its high melting point has proven to be a limiting factor in its viability for industrial applications. The mechanical properties of cast pyrophyllite must also have their mechanical properties measured to determine if there are comparable to mechanical properties of cast basalt.

1.3. Research objectives

The aim of this research was to successfully melt and cast pyrophyllite powder at temperatures comparable to the melting point of basalt using calcium carbonate and or sodium carbonate additives. The secondary aim was to achieve similar properties in the cast pyrophyllite to those of cast basalt. The following objectives were set out to achieve this aim:

- Investigate the effect of using different amounts of calcium carbonate and sodium carbonate as additives on the melting point of pyrophyllite and determine the optimum mixture composition.
- High temperature cast melted pyrophyllite into sand moulds and analyse the microstructure and phase compositions of the cast pyrophyllite samples.
- Determining the mechanical properties of cast pyrophyllite and compare them to those of cast basalt.

1.4. Scope of research

This research will involve the characterisation of pyrophyllite powder sourced from wonderstone, calcium carbonate and sodium carbonate using a mastersizer particle size analyser and X-ray diffraction analysis (XRD). The melting characteristics of powdered

mixtures based on ternary phase diagrams will be analysed using thermogravimetric analysis to determine their melting points. Based on these results melting and high temperature casting will be attempted with admixtures of pyrophyllite and calcium carbonate or sodium carbonate additives. If the casting proves successful samples will be analysed using scanning electron microscopy and X-ray diffraction.

The limitations of the study will therefore be on whether the melting temperatures determined in the thermogravimetric analysis will be within the design specifications of the muffle furnaces that will be used in the study and can be maintained sufficiently during the casting phase to allow for successful casting. To mitigate these potential limitations mixtures with a target melting temperature well within the design specification of the muffle furnace will be selected and thermally insulating ceramic blankets will be used during the casting phase.

1.5. Structure of Dissertation

In Chapter 2 a review of the current literature on petrurgy and the cast basalt industry is detailed. Literature on pyrophyllite and the different additives selected for this research is also presented in this section.

Chapter 3 describes the experimental procedures used in this research together with the equipment and materials utilized, as listed in Sections 3.1 and 3.2. Results are presented in Chapter 4 and discussed whilst the conclusions drawn from this work are presented in Chapter 5.

CHAPTER 2: LITERATURE REVIEW

In this chapter literature on wear resistant parts was reviewed and current developments in basalt casting are compared to the potential viability of casting pyrophyllite. Literature on using admixtures in casting was also explored together with the process of sand casting

2.1. Wear-resistant parts

Wear can in general be described as the continuous material loss from the surface of a solid body by mechanical, thermal or chemical impact of another solid, liquid or gas in contact with the body (Dong, 2010) (Micronz Ltd, 2019). Wear is dependent on multiple different characteristic of a material including the geometrical shape of the surface, intensity and frequency of load, atmospheric conditions, mechanical properties, thermal properties and metallurgical characteristics of the material (Bhadauria, et al., 2020).

Material wear may be abrasive, adhesive, fretting, erosive, fatigue or corrosive. Abrasive wear results from a harder material rubbing or sliding over softer materials resulting in removal of material from the softer surface. This harder material may be on the surface of one of the materials or may be third body introduced from outside (Ko, 1987).

Adhesive wear is similar to abrasive wear however materials undergoing adhesive wear slide over each other with a force pressing them together (Garcia-Cordovilla, et al., 1996). When materials rub against each other cyclically this is known as fretting whilst erosion is caused by solid or liquid particles hitting the surface of a material (Bhadauria, et al., 2020). Surface fatigue or fatigue wear occurs when a material is weakened by cyclical loading that results in crack formation. These cracks then propagate and ultimately lead to failure (Bhadauria, et al., 2020).

Corrosive wear or corrosion is a chemical process involving a chemical substance or a material and a base material that results in the destruction of the base material; the most common form of corrosion is oxidation (Ko, 1987). In general corrosion occurs concurrently with other types of wear. This combined effect is more than additive in nature and results in material failure and additional destructive processes.

Failure due to wear results in industrial costs of hundreds of billions of Dollars yearly (Davis, 2010). This is due to the reduced efficiency of running with worn parts and breakdowns that are experienced. Studies in the United States alone have attributed up to $80 billion annually to wear failures (Davis, 2010).

In South Africa wear resistant parts are equally as essential for all industries including the electrical generation industry which is heavily dependent on coal fired power plants (93% as of 2001) (Winkler, 2005). Unplanned shutdowns due to failure of wear parts can cause massive societal disruptions similar to the country's 2008 electricity crisis when rampant blackouts resulted in damaging effects to the economy and decrease of growth by over 70% (Inglesi & Pouris, 2010). This highlights the local necessity of adequate wear resistant parts.

Various industrial processes and applications require the use of wear resistant parts and materials to prevent or reduce wear loss and the associated downtime of the equipment thereby maintaining performance (Medvedovski, 2001). Traditionally used hard irons, steels and some polymers, however, may prove particularly susceptible to wear and corrosion if materials are transported in liquid corrosive environment, at high velocities and pressures, or if the working parts are employed at elevated temperatures and subjected to thermal shocks (Medvedovski, 2001).

Ceramics are non-metallic materials which have high hardness, good chemical inertness and are brittle (Myra, 2016). This high hardness results in higher wear resistance of ceramic materials (Švec, et al., 2008). Good chemical inertness allows for different

ceramic parts (bearings, valves, seats, cable, wire and thread-guides, dies, and some others), as well as prosthesis and dental ceramics, to be subjected to continued friction from various materials, often in strong corrosive environments (Medvedovski, 2001).

Common wear-resistant ceramic materials currently used in industry include zirconia, alumina, cubic boron nitride, silicon nitride, boron carbide, silicon carbide and basalt. Uses for wear parts range extensively from aerospace construction, to power plant components (Bhadauria, et al., 2020).

Cast basalt in particular is ideal for use in wet material handling applications with lower impacts, such as coal chutes, ash sluiceways, ash pipelines at power stations and hydraulic granulated slag or sand conveying (Multotec, 2019) where it gives high resistance to wear and corrosion at temperatures up to 400°C.

2.2. Petrurgy

Although metals have been cast for thousands of years, non-metallic ores and materials only have a more recent history. Petrurgy is defined as the processing of non-metallic ores by melting at high temperatures (generally > 1300°C) and casting into moulds. These moulds can be manufactured from something as simple as sand with pours and rises to accommodate the molten liquid infill. More complex dies made from heat resistant steels can also be used where multiple similar castings are to be manufactured. The process has been used for centuries to produce various essential products including pipes, casings, tiles and linings (Kopecky, 1965).

The large-scale industry of re-fused rock manufacturing was however only created in the 20th century as an independent branch of the silicate industry (Karamanov, et al., 2009).

2.2.1. Basalt casting

Basalt is a naturally forming igneous rock that comprises over 90% of all volcanic rocks (Barresi, et al., 2014) (The University of Auckland, 2005). It has a lifespan of millennia and has a significantly high hardness. This hardness, however, hindered its ability to be processed and limited its wider adoption, to as late as the 20th century. This was despite theoretical hypotheses suggesting the viability of basalt casting from as early as 1777 (Voldan, 1964) and the first practically aimed melting tests of basalt carried out in 1852 (Adcock, 1853).

These early successes did not initially lead to wider adoption, with the development of practical petrurgical technology beginning only in 1911 (Kopecky, 1965). This followed the work of F. Ribbé who filed several patents for the petrurgical treatment of basalt (Ribbe, 1914). Large scale manufacturing followed with casting of basalt as various components resistant to electrical conduction, chemical attack, wear and abrasion.

In its raw material state, basalt shows slight variations in its composition (Table 2.1). The predominant materials within basalt, however, are silica (SiO_2), calcium oxide (CaO), alumina (Al_2O_3) and magnesia (MgO). These compounds lower the melting point of basalt allowing it to be one of the few alumino silicate materials that can be melted and cast without the use of additives or admixtures (Kopecky, 1965).

Table 2.1: Chemical composition of industrial basalt (weight %), (Kopecky, 1965).

Source / Composition	France	Germany	Russia & CIS	Czech Republic	Poland
SiO_2	42,8	44,7	49,9	45,5	46,1
CaO	11,1	10,5	9,8	10,1	10,0
Al_2O_3	11,0	11,9	12,5	11,7	11,3
MgO	10,0	8,5	6,0	10,1	10,4
FeO	6,3	16,6	3,0	5,6	4,4
Fe_2O_3	7,0		11,0	7,1	7,3
TiO_2	3,6	1,0	2,5	1,1	3,6
Other materials	8,1	6,9	5,4	8,8	6,8

Basalt related igneous rocks can be classified into two main categories, subalkaline and alkaline (Karamanov, et al., 2009). Subalkaline rocks are comprised of tholeiitic and calc-alkaline basalts (Sheth, et al., 2002). Alkaline rocks on the other hand include both alkaline and alkaline olivine basalts (Karamanov, et al., 2009). The materials are categorized on the basis of the differences of their silica, calcium oxide and sodium oxide content.

Currently the majority of the petrurgy industry uses tholeiitic basalts and diabasic rocks. This is due to their higher silica and alumina content which results in a more homogenous crystallisation profile (Karamanov, et al., 2009) as compared to low viscosity alkaline basalts whose crystallisation results in materials that are coarse and inhomogeneous.

2.2.2. Basalt production

The production procedure to cast basalt can be divided into three main segments. These are the fusing stage, casting stage and cooling stage of the castings.

In the fusing stage, crushed basalt is heated to between 1320°C and 1350°C in a furnace similar to a blast furnaces used in steel plants. The resulting molten mixture is then discharged by a spout into a homogenizing drum kept at 1200°C. During homogenisation the melt is mixed thoroughly and forms nuclei that will aid crystallization during cooling.

The homogenized melt is then cast into either sand or steel moulds. The mould selection is dependent on both financial and finished material considerations (Bownes & Beadle, 1971). Sand moulds although more economical, are not able to provide a precision finish. Further machining is required to achieve a final product.

In the moulds the cast material cools and solidifies during crystallisation (Kopecky, 1965). In contrast to this property of basalt more acidic rocks such as pyrophyllite may require admixtures and higher temperatures for fusing.

2.2.3. Basalt applications

Despite industrial application of cast basalt having only started in the 20th century there are several industrial units dedicated to petrurgy manufacturing in various countries including Bulgaria, the Czech Republic, Russia, Germany and the United States (Karamanov, et al., 2009).

Cast basalt is ideally used to manufacture parts where high wear due to abrasion by sharp particles exist (Kopecky, 1965). These include pavements, pipes, bends and building tiles. Basalt may also be used as linings for conveyors, exhausts, cyclones and crushed material separators.

More recently, due to the high chemical durability of basalt, iron rich glass and glass ceramics have also been developed from basalt composite materials for nuclear waste

disposal as well as for vitrification of hazardous industrial wastes and effluents (Bickford & Jantzen, 1986).

2.3. Pyrophyllite

Pyrophyllite is a naturally abundant mineral found in large reserves in the USA, New Zealand, China, Australia, Brazil and South Africa (Mukhopadhyay, et al., 2010). It is mined in the Ottosdal region of the North West province from pyrophyllite veins and is generally referred to as 'wonderstone' due to its favourable properties of strength and workability in industrial applications (Jackson, 1992).

Discovered in 1829, pyrophyllite occurs in both hydrothermal veins and in bedded deposits in schistose metamorphic rocks (Gruner, 1934). As a chemically inert hydrous alumino-silicate, pyrophyllite exists naturally either as a monoclinic structure with three axes of unequal length and only one being perpendicular to both the other two or as a triclinic structure with three axes of unequal length at non perpendicular angles (Brindley, 1970) (Augustyn, et al., 2018).

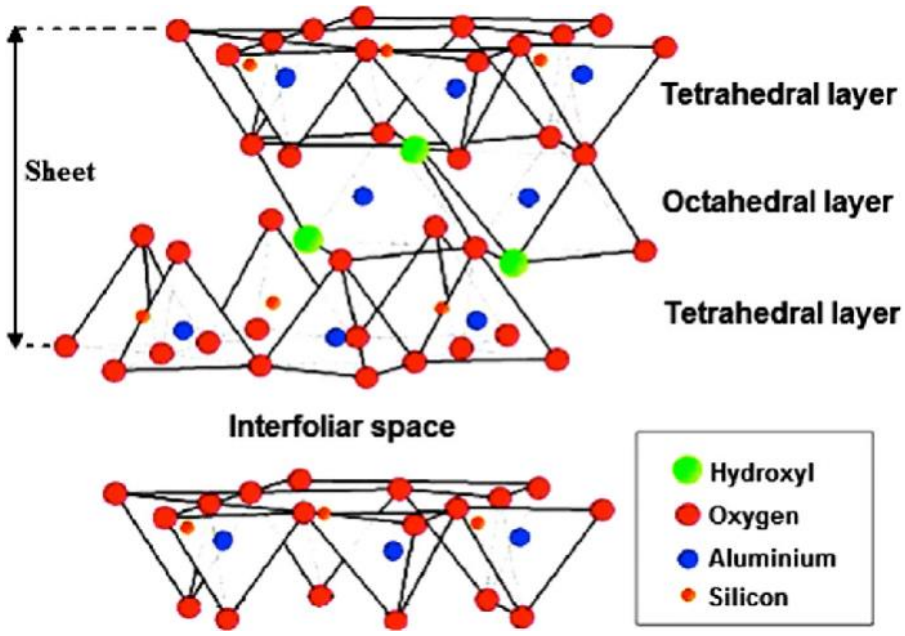

Figure 2.1: Pyrophyllite crystal structure ((Gaidoumi, et al., 2019)).

Its atomic structure is a di-octahedral without interlayer cations (Figure 2.1) (Bentayeb, et al., 2003) and its molecular formula is $Al_2Si_4O_{10}(OH)_2$ giving it a composition of 67% silicone dioxide, 28% aluminium oxide and 5% water (Mukhopadhyay, et al., 2010).

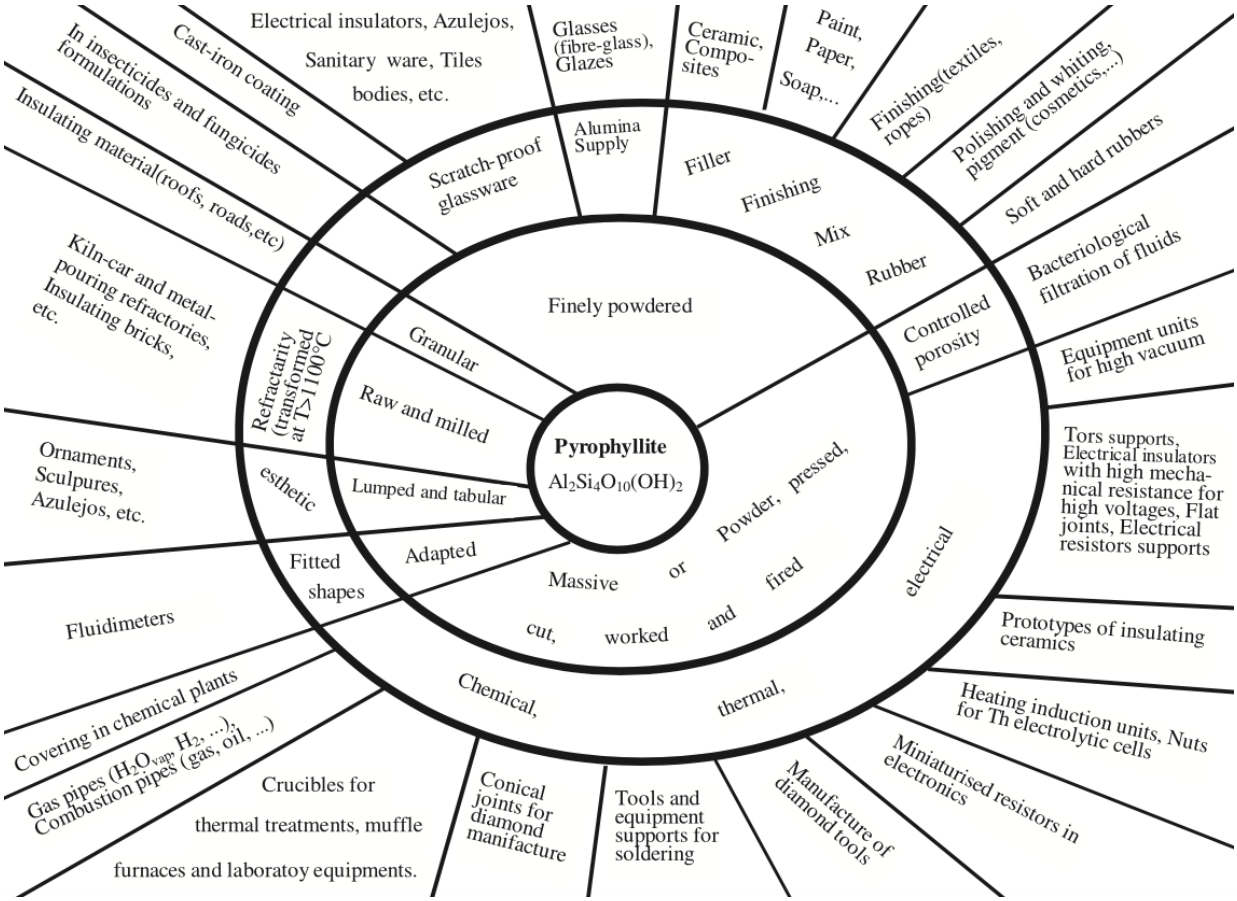

Figure 2.2: Diagram showing the different required starting forms of pyrophyllite for different desired output properties (Bentayeb, et al., 2003).

Pyrophyllite has a variety of uses, as shown in Figure 2.2 due to its numerous desirable characteristics. This including its high refractive behaviour, low thermal and electrical conductivity, low expansion coefficient, low hot-load deformation, low reversible thermal expansion, low bulk density, excellent reheating stability and high resistance to corrosion by molten metals and basic slags (Rieger, 1997). These properties allow pyrophyllite to be used in industrial refractories (Harben, 1995) and in the manufacture

of ceramics and ceramic tiles**Invalid source specified.**. Pyrophyllite is also suitable for production of fibreglass (Auborg & Wolf, 1997).

2.3.1. Pyrophyllite admixtures

As described by Kopecky (1965), materials such as pyrophyllite have higher melting points when compared to basalt. As a mineral known for its refractory behaviour (resistance to high temperature changes), pure “wonderstone” pyrophyllite has a melting point between 1630°C (Uygun & Solakoglu, 2002) and 1750°C (Bentayeb, et al., 2003). This is significantly higher than the melting point of basalt at 1300°C. The higher melting point of pyrophyllite had previously proven to be a limiting factor in the viability of its casting.

Despite limited work on the high temperature casting of pyrophyllite previous studies had analysed the properties of pyrophyllite with increasing temperatures (Sanchez-Soto & Perez-Rodriguez, 1989). The average dehydroxilation temperature of pyrophyllite was determined as being between 560°C and 580°C (Kwon & Newton, 2016) (Mukhopadhyay, et al., 2010). Major transformations included formation/crystallisation of mullite (Sanchez-Soto & Perez-Rodriguez, 1989) at 1200°C and cristobalite at 1300°C (Pérez-Maqueda, et al., 1993).

A solid mixture of two pure compounds (Figure 2.3) typically possesses a melting point lower than its starting compounds. The lowest melting point possible of different compositional mixtures of the two solids is known as their eutectic point (Nordlie, 1989).

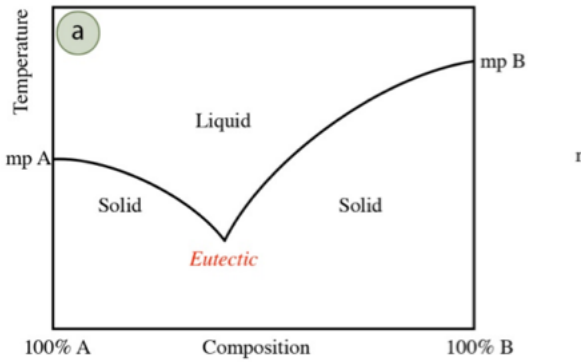

Figure 2.3: Eutectic point of a two-component mixture (Nichols, 2019).

By selecting different compositions of the two or more compounds different melting points can be obtained (Figure 2.4) and depending on the numbers of components binary, ternary, quaternary systems etc. can be made.

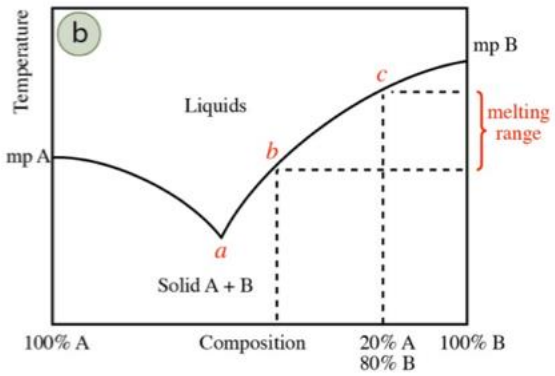

Figure 2.4: Binary phase diagram of a generic two-component system based on different compositions (Nichols, 2019).

Pyrophyllite may be considered a binary phase alumino silicate (Brindley, 1970). Its binary phase diagram Figure 2.5 shows a melting point of approximately 1800°C (red line). To decrease the melting temperatures various admixtures may be used to generate ternary systems with melting temperatures similar to basalt.

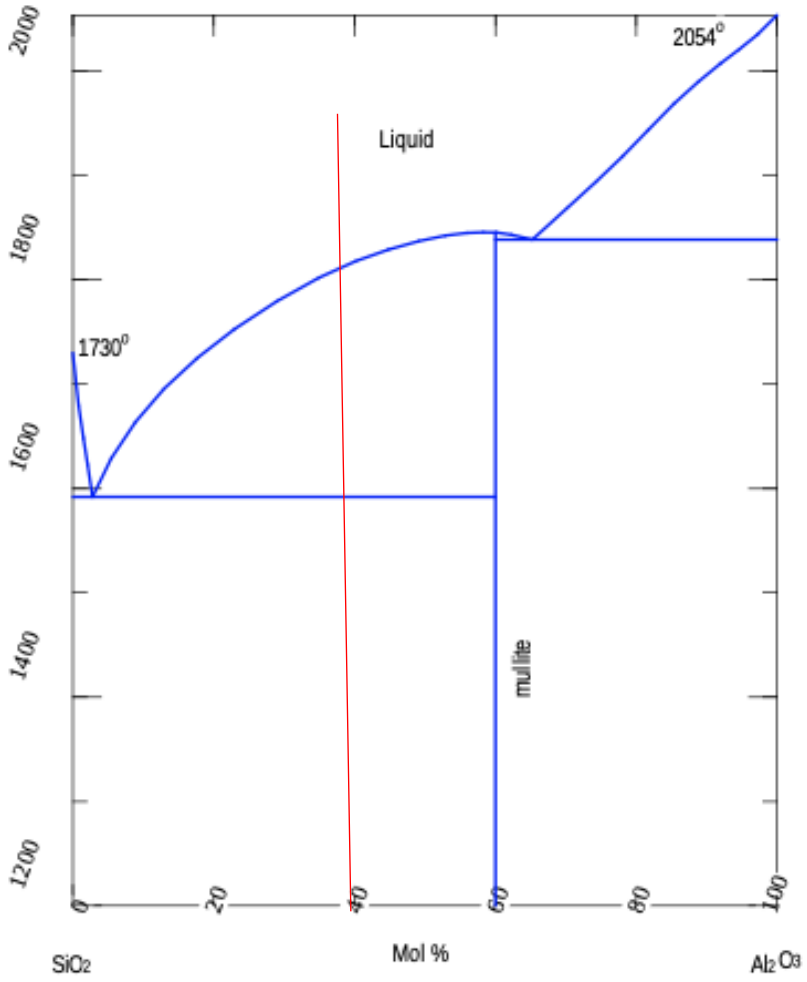

Figure 2.5: Binary phase diagram of the SiO_2-Al_2O_3 system (Li, et al., 1999).

Immediate admixture candidates would be compounds found in basalt such as CaO that enable it to be cast successfully without additional admixtures. In this research CaO and Na_2O were selected.

In Figure 2.6 and Figure 2.7 ternary phase diagrams of pyrophyllite show the effect of different admixture compositions on the melting point temperature of pyrophyllite.

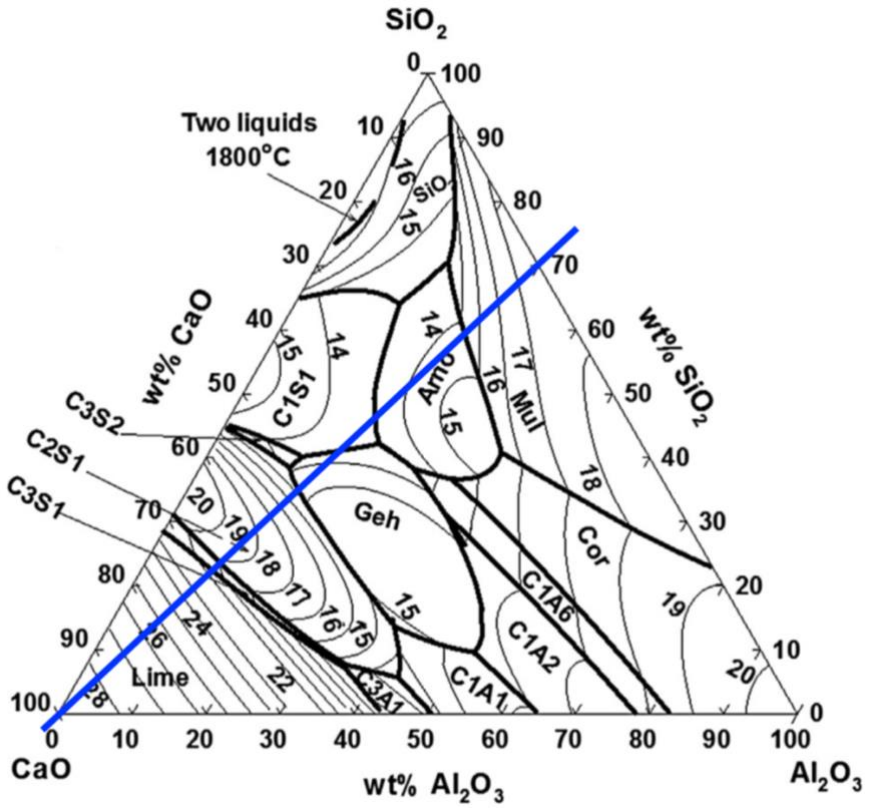

Figure 2.6: Ternary phase diagram of the SiO_2-Al_2O_3-CaO system (Chunlin, 2015).

For both diagrams the starting point was to identify the base composition of pyrophyllite in the SiO_2-Al_2O_3 system. A diagonal line was then drawn in both phase diagrams to represent the composition of pyrophyllite with increasing additions of CaO and Na_2O respectively. These are the compositions that will be investigated in this work.

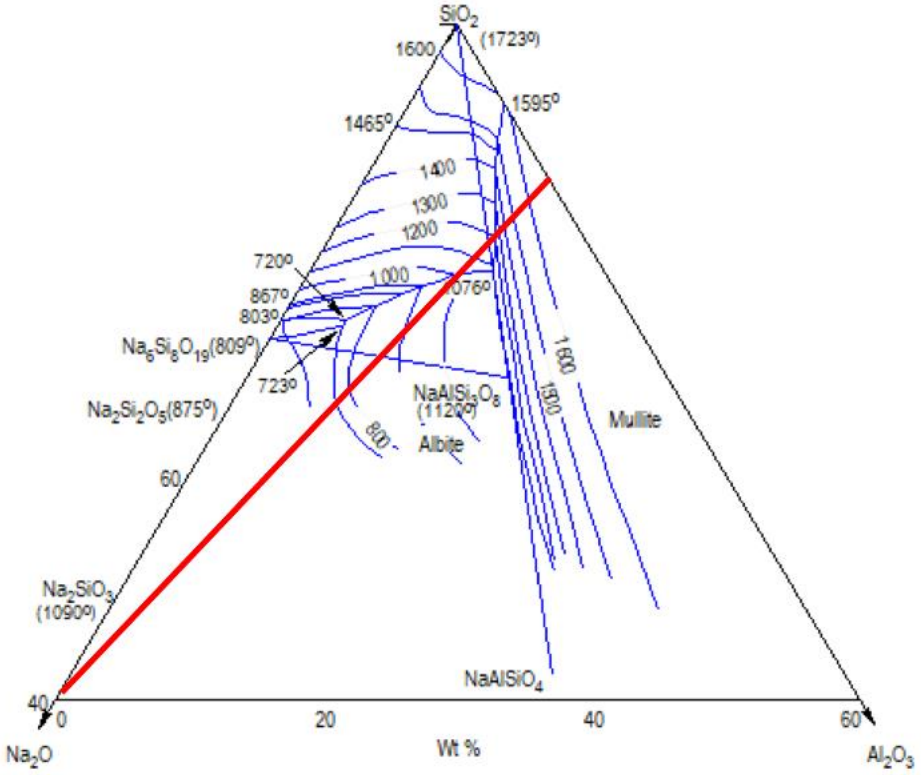

Figure 2.7: Ternary phase diagram of the SiO_2-Al_2O_3-Na_2O system (Chartrand & Pelton, 1999).

From these two figures it was considered possible that either calcium oxide (CaO) or sodium oxide (Na_2O) may be used to lower the melting point of pyrophyllite to temperatures comparable to those used for casting basalt.

2.4. CaO and Na_2O

At room temperature and pressure calcium oxide will spontaneously absorb carbon dioxide from the atmosphere and convert this to calcium carbonate (Pawelec & Fierro, 2003). Calcium carbonate is, however, also known to decompose to CaO (solid) and CO_2 (gas) at elevated temperatures and pressures (Galan, et al., 2013). Decomposition occurs according to the following chemical reaction:

$$CaCO_3\ (s) \rightarrow CaO\ (s) + CO_2\ (g)$$

This reaction occurs at temperatures from 680 to 875°C depending on the heating rate used (Rao, 1996) with decomposition temperature increasing with an increase in the heating rate.

Calcium carbonate is naturally available globally in abundant deposits of limestone, chalkboard of marble (Mallick, 2000). It is white in colour and chemically stable to about 800°C.

Sodium Carbonate (Na_2CO_3) also decomposes to form sodium oxide (Na_2O). This compound, however, only fully decomposes above its melting point of 850°C (Motzfeldt, 1955) according to the following chemical reaction:

$$Na_2CO_3\ (s) \rightarrow Na_2O\ (s) + CO_2\ (g)$$

This means that although Na_2O cannot be as easily obtained from Na_2CO_3 in the same manner that CaO was obtained from $CaCO_3$, the high temperatures associated with casting mean that it can still be used as an additive for pyrophyllite casting.

Sodium carbonate is also known as soda ash and is also widely found and mined throughout the world. It is a white powder and is available in two main grades: light or granular (Brandt & Ratnayaka, 2017).

2.5. Sand Casting

Casting of materials such as metals is amongst the oldest methods of manufacturing dating back to approximately 3 600 BC (Singha & Singh, 2015). Within the field of casting,

sand casting is the oldest and most widely used method, occupying up to 90% of all foundry production cast into moulds (Bownes & Beadle, 1971).

The dominance of sand casting is due to the relative ease of moulding sand particles to a particular shape and the low cost owing to the abundance of sand globally. Sand casting as a process is also flexible as the production can be scaled up or down from a few grams of product to several tonnes. There is also flexibility of application as sand casting may be used for a variety of materials ranging from alloys to metals (Bownes & Beadle, 1971).

Sand casting is also ideal as molten material when poured into a refractory mould where temperatures are gradually decreased as it cools. This results in a reduction of the internal stresses on the molten material as it cools in comparison to steel moulds for example where there is rapid extraction of heat from the mould (Kopecky, 1965).

2.5.1. Method of sand casting

In general sand casting consists of the following basic processes, Figure 2.8 (Groover, 2011):

- A sand mixture is created using a combination of sand, moisture, lime and or clay
- An object or reference pattern (which is a replica of the final product) is created/machined and added to the sand to create the mould/cavity:
- When the mould/cavity is ready, molten material is poured in and left to cool and solidify.
- The solidified product is broken out of the mould and machined if required to remove imperfections.

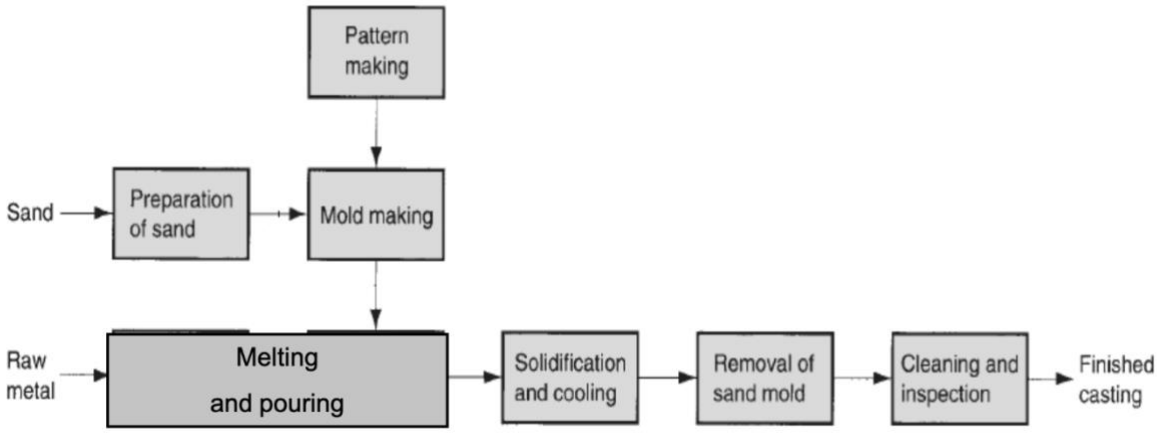

Figure 2.8: Diagram showing sand casting process (Groover, 2011).

2.5.2. Sand and mould characteristics

Sand casting generally uses the materials shown in Table 2.2:

Table 2.2: Materials used for sand casting moulds (Campbell, 1984).

Refractory sand and grains	Facing material	Cushion
Silica	Sea coal	Wood flour
Zircon	Pitch	Cereal hulls
Olivine	Graphite	Cereal
Dolomite	Coke	Cellulose
Magnesite	Silica	Sea coal
Carbon		Coke
Coke		Perlite
Sillimanite		

The most common basic material used in mould production currently is clay bonded silica sand (Bownes & Beadle, 1971). Both natural and synthetic silica sand may be used, and these are generally bonded with bentonite clay. Water is added to plasticise the clay and various other additives may also be added to achieve particular characteristics for example cereal binders to improve toughness.

The following binders may also be used to strengthen the mould (Campbell, 1984):

Clays:

- Fire clay (kaolinite)
- Southern bentonite (calcium montmorillonite)
- Western bentonite (sodium montmorillonite)
- Secondary mica clays (illite)

Oils:

- Vegetables
- Marine animal
- Mineral

Synthetic resins, thermosetting:

- Urea formaldehyde
- Phenol Formaldehyde
- Cereal binders made from corn:
- Gelatinized starch
- Gelatinized corn flour

Wood –product binders:

- Natural resin
- Sulphite binders
- Water-soluble gums, resins, and organic chemicals

Protein binders (containing nitrogen):

- Glue
- Casein

Other binders:

- Portland cement
- Pitch
- Molasses
- Cements
- Sodium silicate (water glass, CO2 hardening binders)

After creating the mould, a good casting mould should have the following characteristics (Sharma, 2010):

- Good dry strength and hardness after baking
- Sufficient green strength to retain the shape before baking
- Refractoriness
- Surface smoothness
- Permeability
- Lowest possible amount of gas created during the pouring of the casting

2.5.3. Melting of raw materials

Furnaces are generally used to heat materials to a molten (liquidous) temperature sufficient for casting. For these materials to reach a molten state sufficient heat energy is required. The total heat energy (H) required would be equal to the sum of:

$$
\begin{aligned}
&H \\
&= \ heat\ energy\ to\ raise\ temperature\ to\ melting\ point \\
&+ heat\ of\ \ fusion\ to\ convert\ \ from\ solid\ to\ liquid \\
&+ heat\ energy\ to\ raise\ temperature\ to\ adequate\ pouring\ visciocity
\end{aligned}
$$

This equation can be expressed as

$$H = \rho V\{C_S(T_m - T_a) + H_f + C_l(T_p - T_m)\}$$ (Groover, 2011)

Where:

H is the total heat required to increase the temperature of the metal to the pouring temp (J)

ρ Density (g/cm^3)

V Volume of material used for heating (cm^3)

C_S Specific heat for the solid (J/g °C)

T_m Melting temperature of the material (°C)

T_a Ambient temperature (or starting) (°C)

H_f Heat of fusion (J/g)

C_l Specific heat of the liquid material (J/g °C)

T_p Temperature of the pouring liquid (°C)

And the following assumptions were used:

- Specific heat and other thermal properties of the solid material are constant and not dependent on temperature.
- A single melting point.
- A single heat of fusion which occurs at this melting point.
- Negligible heat losses to the environment during heating.

2.5.4. Crystallisation and glass ceramics

Glass ceramics are polycrystalline materials formed by controlled crystallisation heat treatments of appropriate parent glasses (Lee, et al., 1993). Their microstructure consists of a high concentration of small crystals, typically 0.1–1 micron, uniformly distributed in a residual glass phase (Partridge, 1994)

The crystalline phases formed, and the crystals' growth rate and final size depend not only on the chosen parent glass but also on the imposed thermal treatment and on the addition of nucleating agents (Guedes, et al., 2001). The heat treatment comprises nucleation and crystallisation temperature hold, and other holding stages may be included in order to develop the desired structure and properties (Partridge, 1994).

Nucleating agents are minor constituents that provide the desired microstructure by supplying the nuclei for subsequent crystal growth or by influencing the structural reorganisation in the glass, so that the desired crystalline phase will grow (Guedes, et al., 2001). In the production of glass ceramics, nucleating agents such as ZrO_2, TiO_2 or P_2O_5 can be used in order to induce bulk crystallisation of the phases. These additions may also decrease the crystallisation time and temperature required for specific phases (Ceylan, et al., 2010).

CHAPTER 3: METHODOLOGY

In this section the experimental procedures used in this research are described together with the equipment and materials utilised.

3.1. Materials and chemicals

This research utilized pyrophyllite sand sourced from Wonderstone and mined in the North West of South Africa. Calcium carbonate, sodium carbonate and zirconia, all of 99,9 wt. % purity, were purchased from Sigma Aldrich. Basalt tiles and silica sand were also purchased from G-Fox and AQUAMAT respectively.

The full list of materials and chemicals used during this research are presented in Table 3.1 together with their supply source.

Table 3.1: Table of materials used in research and source.

Material	Supplier
Pyrophyllite	Wonderstone
$CaCO_3$	Sigma Aldrich (Pty) Ltd.
Na_2CO_3	Sigma Aldrich (Pty) Ltd.
Silica sand	AQUAMAT South Africa (Pty) Ltd.
Basalt	G Fox Johannesburg
Zirconia	Sigma Aldrich (Pty) Ltd.

3.2. Facilities and machinery used

Various equipment and facilities were utilized during the preparation, experimentation and analysis of the samples produced in this research. The full list of facilities and equipment used are listed in Table 3.2.

Table 3.2: Table of facilities used in research and location.

Facility	Location/Department
Bruker D2 Advance XRD	Wits University: MMU
SEM analysis	Wits University: CHMT RW
Sputter coating	Wits University: MMU
TG/DSC analysis	CSIR
Hydraulic press	Wits University: CHMT RW
Particle size analyser Malvern Mastersizer 2000	Wits University: CHMT RW
Turbula T2F Mixer	Wits University: CHMT RW
Struers Secotom-10 precision cutting machine	Wits University: CHMT RW

3.3. Material Preparation

3.3.1. Powder property measurement and composition

The starting materials for the cast material were as supplied 40-micron pyrophyllite powder. The 99,9% purity calcium carbonate and sodium carbonate additives were also used. Particle size analysis of the powders was determined using a particle size analyser (Malvern Mastersizer 2000) with water used as the dispersant.

Using SiO_2-Al_2O_3-CaO (Figure 3.1) and SiO_2-Al_2O_3-Na_2O (Figure 3.2) ternary phase diagrams two different compositions of each additive were selected based on the expected melting points of 1300°C and 1400°C.

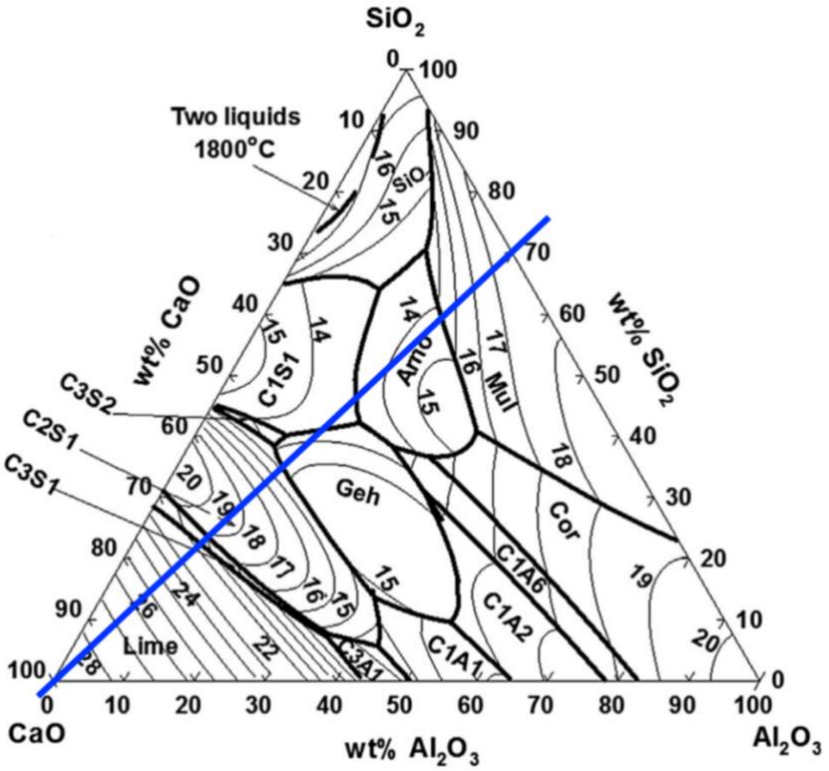

Figure 3.1: Ternary phase diagram of the SiO_2-Al_2O_3-CaO system (Chunlin, 2015).

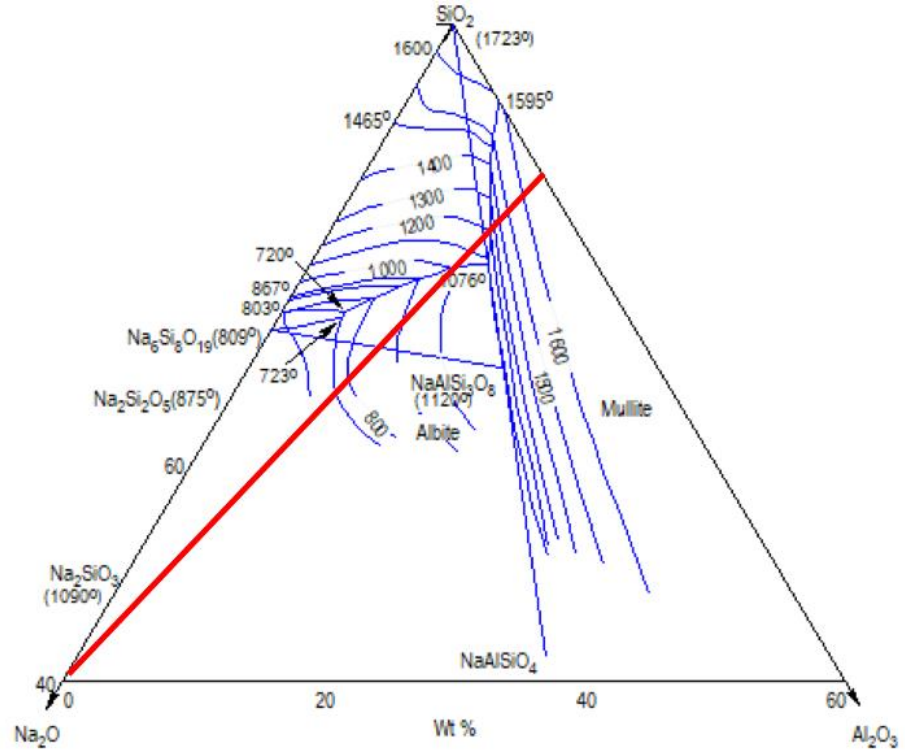

Figure 3.2: Ternary phase diagram of the SiO_2-Al_2O_3-Na_2O system (Chartrand & Pelton, 1999).

The added red lines drawn in both phase diagrams represent the composition of pyrophyllite with different additions of CaO and Na_2O respectively. These compositions are presented in Table 3.3.

Table 3.3: Compositions of pyrophyllite with $CaCO_3$ or Na_2CO_3 additives.

	Temperature (°C)	Pyrophyllite (%)	$CaCO_3$ (%)	Na_2CO_3(%)
Mixture 1	1400	60,32	39,68	
Mixture 2	1300	52,81	47,19	
Mixture 3	1400	83,61		16,39
Mixture 4	1300	81,54		18,46

3.3.2. Compaction and mixing of powders

The selected compositions were mixed in a turbula T2F mixer to ensure even distribution of the additives in the pyrophyllite mix. Batches of 25-grams containing pyrophyllite and additive mixtures were rotated at 60 rpm for 1 hour together with ten, 7 mm diameter alumina balls used to aid homogenisation.

The mixed powders were subsequently compressed in batches of 12,5 grams in a die set of diameter 2 cm to create pellets with a target thickness of 3cm in a hydraulic press. This was to ensure easy handling of the powders and increase precision/reproducibility of each individual melt.

3.3.3. Thermogravimetric Analysis

Thermogravimetric analysis is a technique in which the mass of a substance is monitored as a function of temperature or time as the sample specimen is subjected to a controlled temperature program in a controlled atmosphere (Prime & Bair, 2009) (PerkinElmer, Inc., 2015). The resultant mass loss can be used to predict and or confirm various

properties of the specimen including composition, thermal stability, moisture content, additives and ageing due to thermal and thermo-oxidative processes.

In order to determine the melting behaviour of the selected melting compositions thermogravimetric analysis (TGA) and differential scanning calorimetry (DSC) were performed on pyrophyllite powder samples with and without additives. The scans were performed up to 1500°C without temperature holding using a Netzsch STA449S3 Jupiter simultaneous thermal analyser. The measurements were performed on 35mg samples in alumina crucibles in an atmosphere of inert nitrogen gas.

3.4. Casting

3.4.1. Casting apparatus

Prior to casting, thermal shock tests were performed on both the yttria-stabilized zirconia crucibles and the selected muffle furnace to determine their suitability for casting.

Three empty crucibles were filled with water, pyrophyllite powder or a slightly viscous emulsion of the two materials. The quenching process was then simulated by placing the three crucibles in a furnace and measuring the time it took to open the furnace door and pour the material from within the crucible into a mould. An average time of 30 seconds was obtained from opening the crucible door to closing it after pouring the material out.

The crucibles were then emptied, heated to 1500°C and cooled to room temperature at a heating and cooling rate of 10°C/min. Cooled crucibles were inspected for damage and

or cracking. After inspection, the crucibles were reheated to 1400°C at a heating rate of 10°C/min.

Whilst at 1400°C, the muffle furnace was opened, and the crucibles were removed and exposed to room temperature conditions for a total of 30 seconds. At 30 seconds the crucibles were replaced in the furnace and the furnace was cooled to room temperature at a rate of 10°C/min.

Both the crucibles and muffle furnace were again inspected for damage and after finding no damage deemed suitable for the casting process. To further reduce the effects of thermal shock an additional thermally insulating ceramic blanket was also placed around the crucible prior to casting. This final setup is shown in Figure 3.3.



Figure 3.3: Setup of melting crucible with ceramic blanket.

3.4.2. Casting bed

A mould of pyrophyllite sand was made into a casting bed and 20mm diameter holes of 40mm depth were indented into the bed as casting sites (Figure 3.4). The pyrophyllite

bed was heated and maintained at a temperature of 100°C for 48 hours and graphite foil was used as lining for the casting bed (Figure 3.4) to prevent rapid de-hydroxylation of the uncalcined pyrophyllite during quenching/casting.

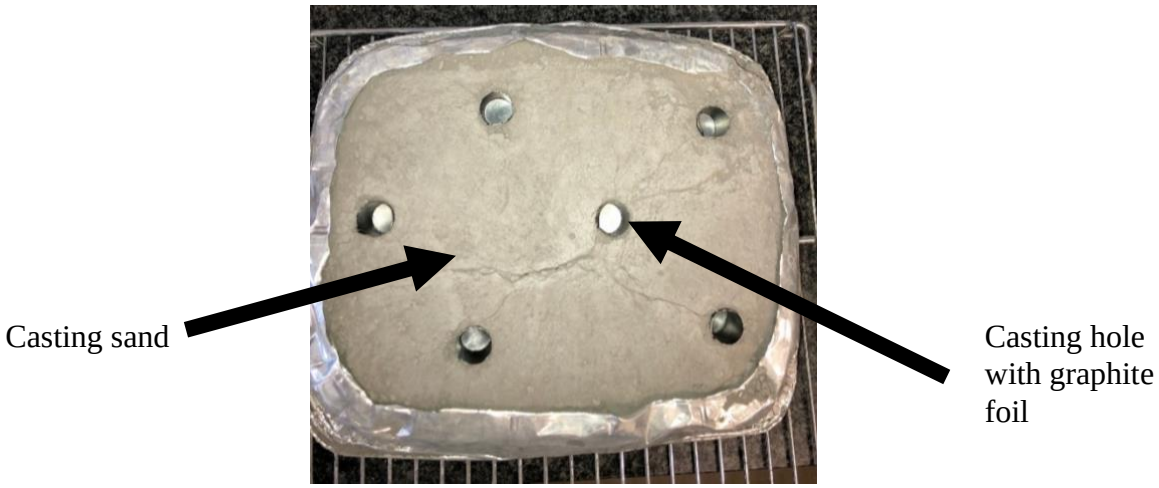

Figure 3.4: Pyrophyllite casting bed.

3.4.3. Quenching process and recrystallization

Pyrophyllite mixtures were placed in yttria-stabilized zirconia crucibles and heated to the expected melt temperature (1300/1400°C) in a muffle furnace. This temperature was held for 1 hour to increase the homogeneity of the melt.



Figure 3.5: Casting of melted pyrophyllite.

After 1 hour the furnace was opened and the melt was poured into the pyrophyllite sand bed (Figure 3.5). The cast material was allowed to cool in the pyrophyllite sand bed to room temperature, (Figure 3.6).



Figure 3.6: Cast samples cooling in pyrophyllite bed.

Upon cooling, these cast samples were found to be amorphous and required 2 additional heat treatment cycles to crystallize. This heat treatment involved heating the samples to 900°C for 2 hours followed immediately by heating to 1040°C for 2 hours based on the crystallization techniques described by (Duan & Liang, 1998).

To resolve the requirement for further complex heating cycles an additional 1, 3, 5, 8 and 10 mass % of zirconia was added to provide nucleation sites for the cast pyrophyllite samples and induce melting and crystallization in a single heating and cooling cycle.

The following compositions in Table 1 were used to induce crystallization in the cast pyrophyllite samples.

Table 3.4: Compositions of pyrophyllite with $CaCO_3$ and Zirconia additives.

	Compositions in wt. %		
	Composition 1	Composition 2	Composition 3
Pyrophyllite	52,28	51,24	50,21
Calcium carbonate	46,72	45,79	44,86
Zirconia	1,00	3,00	5,00
	Compositions in wt. %		
	Composition 4	Composition 5	
Pyrophyllite	48,59	47,57	
Calcium carbonate	43,42	42,50	
Zirconia	8,00	10,00	

These compositions were melted at 1400°C and cast into the pyrophyllite sand moulds. Recrystallization was then attempted for the cast samples at 900°C, 950°C, 1000°C, 1050°C and 1100°C for 2 hours. Samples with calcium oxide additives were the first compositon to be successfully cast. Although the sodium oxide added samples melted within the crucibles they could not be cast as they proved to be too viscous even at high temperature to be poured out of the crucible. Therefore the sodium oxide additive route was considered unsuccessful and was not pursued further.

3.5. Material Characterisation

3.5.1. Particle size analysis

Particle size analysis of the starting powders was done using a particle size analyser (Malvern Mastersizer 2000) with water used as the dispersant. Material densities and diffraction values used were obtained from literature and the safety data sheets (SDS) supplied by the manufacturers, Table 3.5.

Table 3.5: Densities and refractive indices of powders.

	Density (g/cm^3)	Refractive index
Pyrophyllite	2,65-2,90	1,534 – 1,601 (NGL, 2020)
$CaCO_3$	2.93	1,656((SigmaAldrich, 2020)
Na_2CO_3	2,53	1,485 (SigmaAldrich, 2020)

3.5.2. Density

Bulk densities of the samples were measured according to Archimedes principle using a Sartorius balance and distilled water as the liquid media. Samples were placed in continually boiling distilled water for 3 hours to displace air bubbles lodged in sample pores. Boiled samples were cooled to room temperature and 5 measurements of their mass were taken.

- The first measurement was the mass of the sample whilst immersed in water (suspended mass - m_s).
- The second measurement was of the mass of a pat dried sample with the water saturated within its pores (m_{sat}).
- The third measurement involved first drying the samples in a 100°C oven for 24 hours and measuring the dry mass of the sample (m_d)

Five measurements were performed per step for each sample to determine the average and the standard deviation values. The density was then calculated using the formula (Keenan, et al., 1997):

$$\rho = \frac{m_{sat}}{m_{sat} - m_s} \times P$$

Where:

ρ is the density of the sample

P is the density of distilled water at room temperature

3.5.3. Cutting of Samples

Cutting of samples for further analytical tests was performed using a Struers Secotom-10 precision cutting machine and a 200mm diameter Struers diamond cut off wheel.

3.5.4. XRD

Crystal phases of the cast and crystallised materials were identified by X-ray diffraction (XRD) analysis using a diffractometer (D2 Advance, Bruker, Germany) equipped with a copper anode. Radiation was produced at 30kV and 10mA. A scan mode of 0.02° was used with the diffractogram collected over a 2θ range between 10° and 90°.

3.5.5. SEM

The microstructures and morphology of the cast samples were observed with a field emission scanning electron microscope (FESEM, Carl Zeiss) equipped with an Olympus X-Act EDS detector. Samples for SEM were polished to a 1 µm mirror finish and coated with carbon and gold-palladium. This was done to improve the electrical conductivity of the samples and improve the backscatter image quality.

3.6. Mechanical properties

3.6.1. Hardness and fracture toughness

Vickers hardness and fracture toughness test indentations were made with a diamond indenter, at a load of 5kg held for 10 seconds, according to the technique described by (Anstis, et al., 1981). Crack and indentation measurements were taken using an attached optical microscope with both 2a and 2c measured as shown in Figure 3.7.

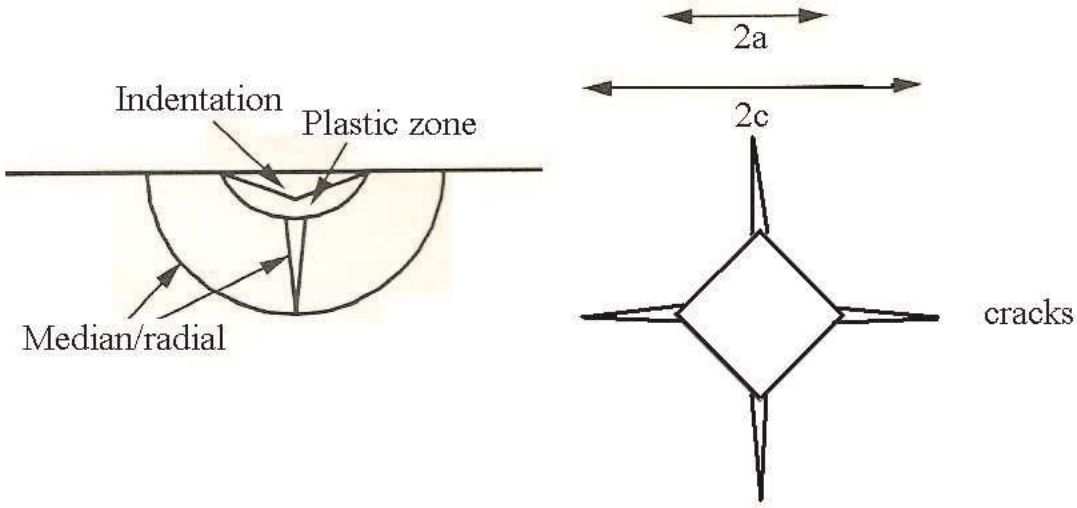

Figure 3.7: Measurement of cracking around hardness indentation (Rocha-Rangel, 2011).

CHAPTER 4: RESULTS

This section presents the results obtained from the experimental method described in Chapter 3.

4.1. Differential thermal analysis / Thermogravimetric analysis (DTA-TG)

The DTA-TG curves of pyrophyllite obtained up to 1500°C are shown in Figure 4.1. The weight loss curve shows a steep decrease at 530°C followed by a gradual decrease with increasing heat from 600°C. This coincides with a sharp endothermic peak at 526°C and a broad endothermic curve that has its inflection point around 730°C. Previous work on the differential thermal analysis of pyrophyllite identify this mass loss as due to the loss of the hydroxyl group.

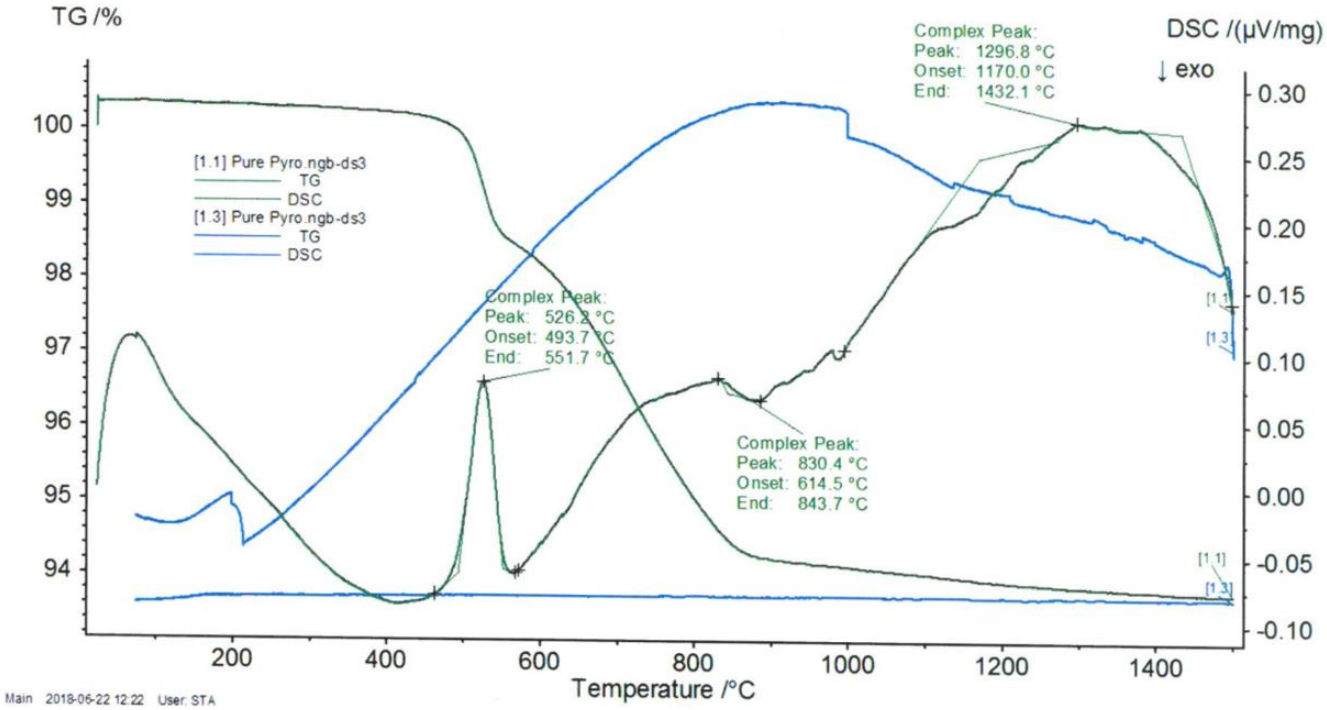

Figure 4.1: DTA-TG curves of pure pyrophyllite.

Minimum weight loss was observed above 900°C and the total weight loss agrees with that of ideal pyrophyllite at 5%. At higher temperatures weak exothermic peaks were produced. The first one occurs at approximately 1200°C with a second at 1300°C. Previous results attribute these peaks to the formation/crystallisation of mullite (Sanchez-Soto & Perez-Rodriguez, 1989) and cristobalite respectively (Pérez-Maqueda, et al., 1993).

The next four DTA-TG curves obtained were of pyrophyllite admixed with calcium carbonate or sodium carbonate. The mixtures by weight % were determined using the ternary phase diagrams of the two additives with pyrophyllite and are presented in Table 4.1.

Table 4.1: Compositions of pyrophyllite with $CaCO_3$ or Na_2CO_3 additives.

	Temperature (°C)	Pyrophyllite (%)	$CaCO_3$ (%)	Na_2CO_3(%)
Mixture 1	1400	60,32	39,68	---
Mixture 2	1300	52,81	47,19	---
Mixture 3	1400	83,61	---	16,39
Mixture 4	1300	81,54	---	18,46

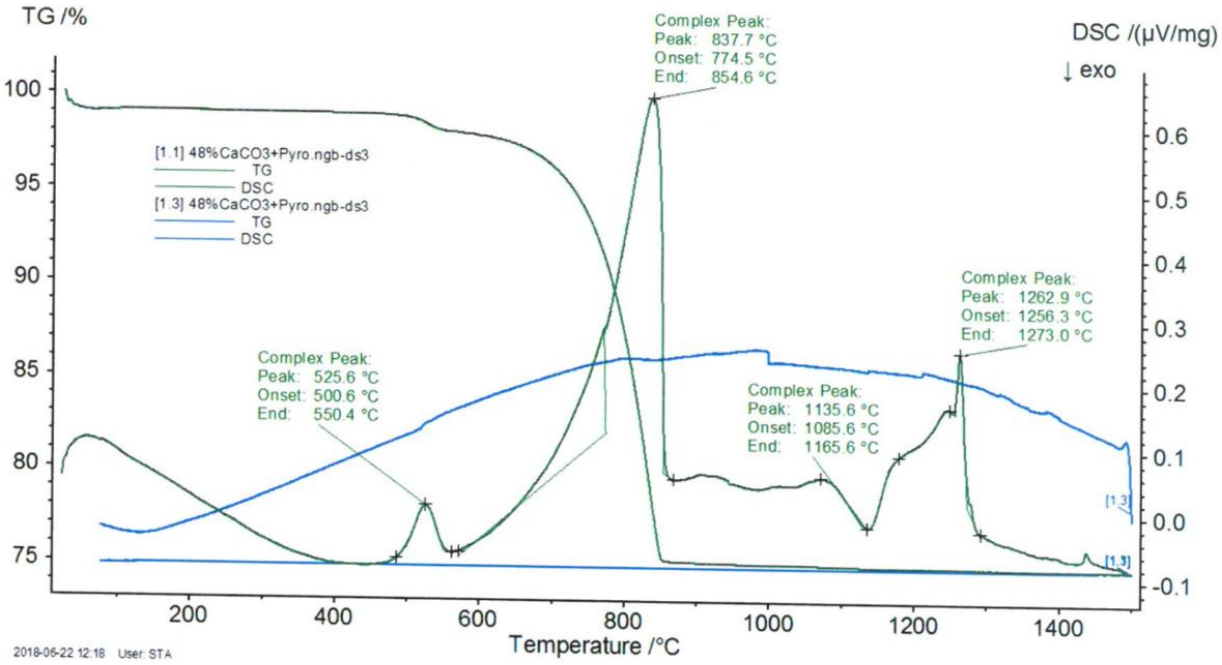

Figure 4.2: DTA-TG curves of pyrophyllite mixed with 48 wt. % calcium carbonate.

The TG graph in Figure 4.2 was of Mixture 2 up to 1500°C. Similar to the TG curve for pure pyrophyllite, a sharp weight loss was observed at 525°C followed by a gradual decrease afterwards. The first Endothermic peak from 500°C is similar to the peak observed in Figure 4.1. From the decomposition reaction this weight loss corresponds to the dehydroxylation of pyrophyllite.

A strong endothermic peak however was also observed from 600°C to 850°C corresponding to an increased rate of mass loss. This peak represents the decomposition reaction of calcium carbonate which was described by Rao (1996) as occurring from 680°C to 875°C and having the following chemical reaction:

$$CaCO_3\ (s) \rightarrow CaO\ (s) + CO_2\ (g)$$

The total weight loss also agrees with the theoretical weight loss predicted for both the decomposition and dehydroxylation reactions combined. The third endothermic peak

which ends at close to 1300°C corresponds to the predicted melting temperature of the mixture from the ternary phase diagram of SiO_2 – Al_2O_3 – CaO.

Similarly, the TG graph for Mixture 1 which contained less calcium carbonate than Mixture 2 showed the same trend, (Figure 4.3). A sharp weight loss and a second gradual decrease that completed around 800°C was also obsevered.

The strong endothermic peak that corelated to the decompostion of calcium carbonate was however less intense and the total mass loss was also lower than for Mixture 2 with about 15% total mass loss.

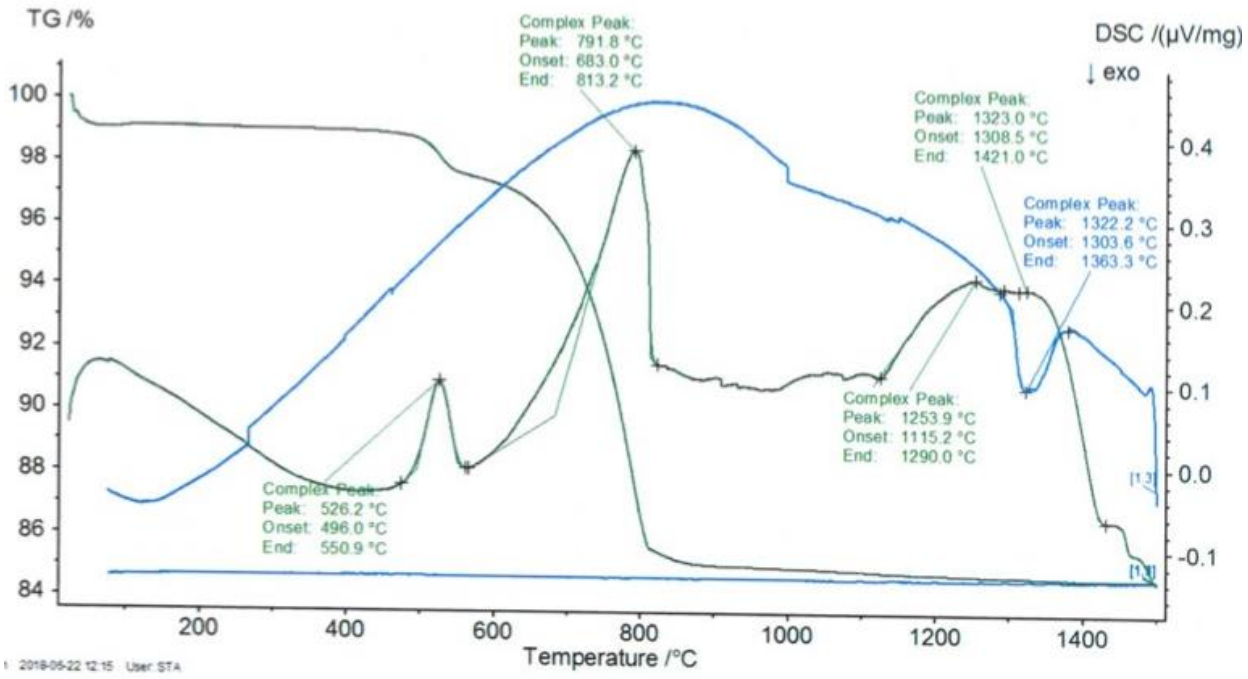

Figure 4.3: DTA-TG curves of pyrophyllite mixed with 39 wt. % calcium carbonate.

Melting which aligned with the third endothermic peak also ended closer to 1400°C as expected for this mixture from the ternary phase diagram of SiO_2 – Al_2O_3 – CaO.

The third and fourth TG graphs of pyrophyllite with admixtures were of Mixture 3 and Mixture 4 (Figure 4.4 and Figure 4.5). These contained sodium carbonate in 15 and 19 wt. % mixtures respectively.

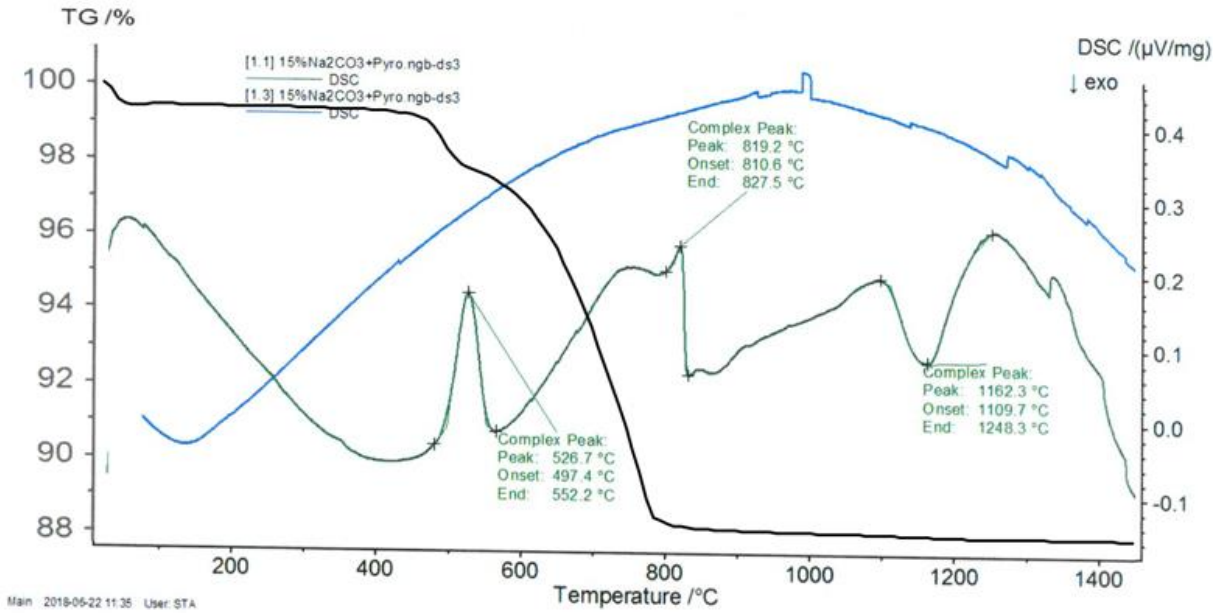

Figure 4.4: DTA-TG curves of pyrophyllite mixed with 15 wt. % sodium carbonate.

Both graphs showed similar curves to pure pyrophyllite and calcium carbonate admixed graphs. They both showed a sharp initial mass decrease around 500°C corresponding to the dehydroxylation reaction. This was followed by a gradual mass loss during the decomposition of sodium carbonate until about 800°C.

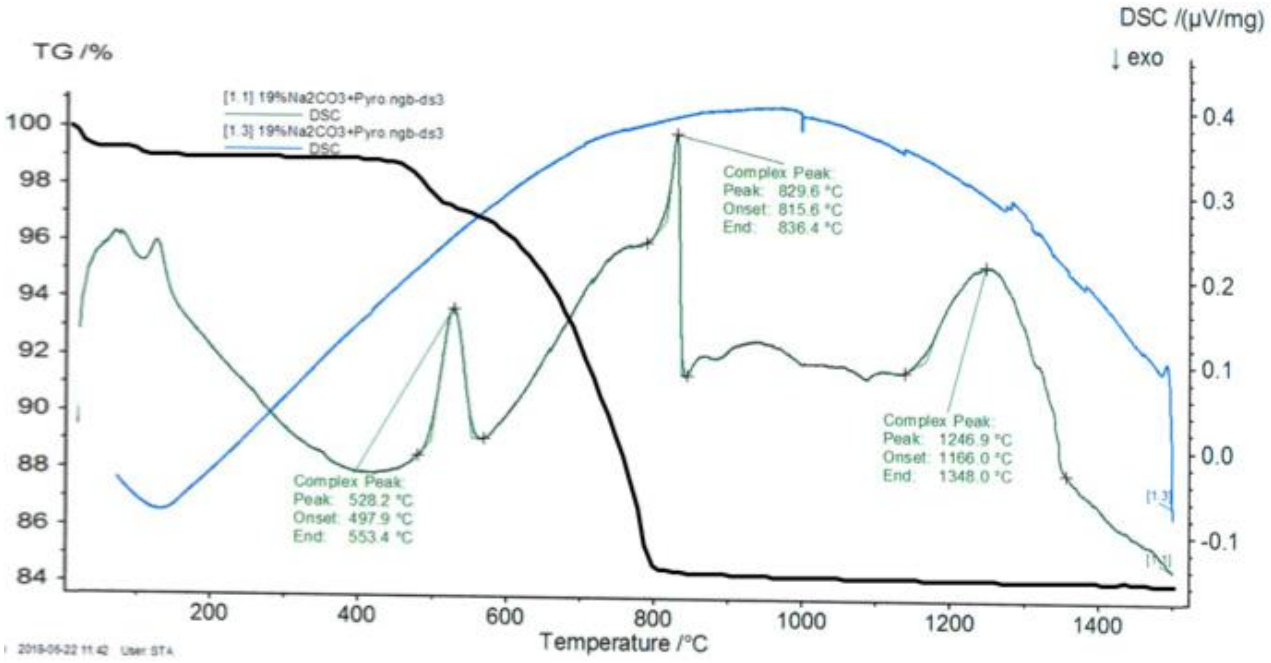

Figure 4.5: DTA-TG curves of pyrophyllite mixed with 19 wt. % sodium carbonate.

Tertiary endothermic peaks were observed around 1300°C for Mixture 3 and 1400°C for Mixture 4 correlating with the expected melting temperatures of both mixtures as determined from their ternary phase diagram.

Based on the thermogravimetric analysis results Mixtures 2 and 3 were selected for further casting based on their expected lower melting temperatures and the operating limits of the muffle furnace used.

4.2. Sample casting and crystallography

As detailed in section 3.4.4 of the methodology, the composites with the lowest melting points were heated to a liquid phase in yttria-stabilized zirconia crucibles. In Figure 4.6 the melting setup is shown with the compressed composite samples placed in the Y_2O_3-stabilized ZrO_2 crucibles. A ceramic blanket heat insulator was placed around the crucible to prevent thermal shock during casting, (Figure 4.6a). The pyrophyllite sand casting mould was also used with a graphite foil lining (Figure 4.6b).

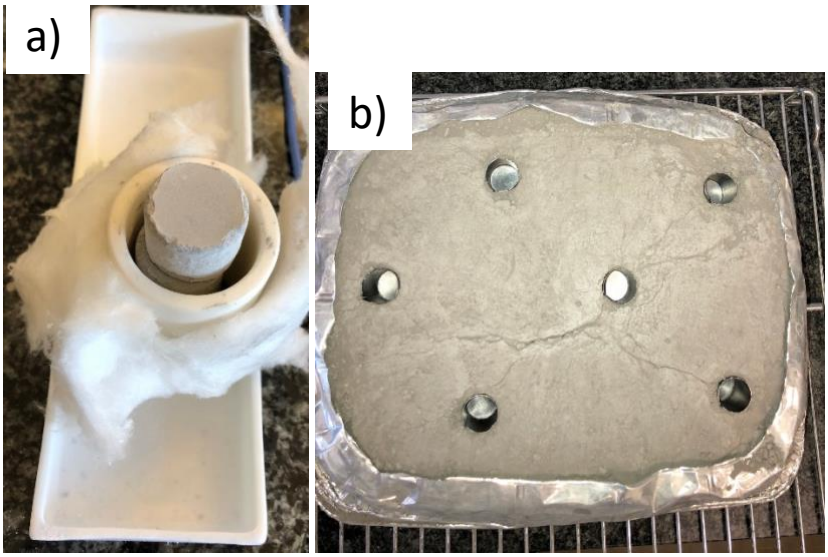

Figure 4.6: a) Placement of pyrophyllite mixture in crucible, b) pyrophyllite sand casting mould.

The resulting molten mixtures were cast into sand moulds and allowed to naturally cool. Figure 4.7 shows cast samples cooling within the mould.

Samples with calcium oxide additives were the first compositon to be successfully cast. Although the sodium oxide added samples melted within the crucibles they could not be cast as they proved to be too viscous at high temperature to be poured out. Results are therefore presented for Mixture 2 which contained 53 wt. % pyrophyllite and 47 wt. % calcium carbonate.



Figure 4.7: Molten samples in casting bed.

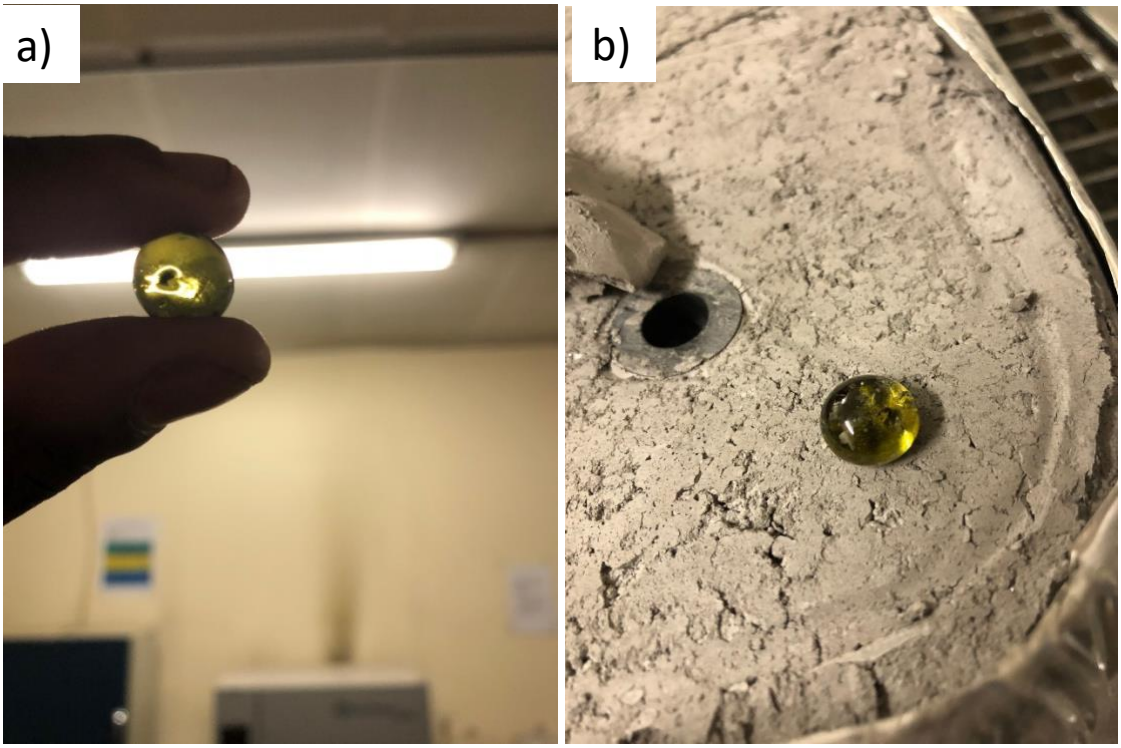

Figure 4.8: a) Cast sample being held against light b) Cast sample placed on pyrophyllite casting bed.

After cooling, cast samples were broken out of the mould for analysis and mechanical testing. Cast samples were glassy, smooth, and transparent, showed no porosity and had a sea green colour as shown in Figure 4.8.

XRD analysis of the samples showed that they were amorphous with no crystalline peaks identifiable, (Figure 4.9a). SEM imagery also did not show any microstructural grains (Figure 4.9b). The cast samples were therefore identified as glass.

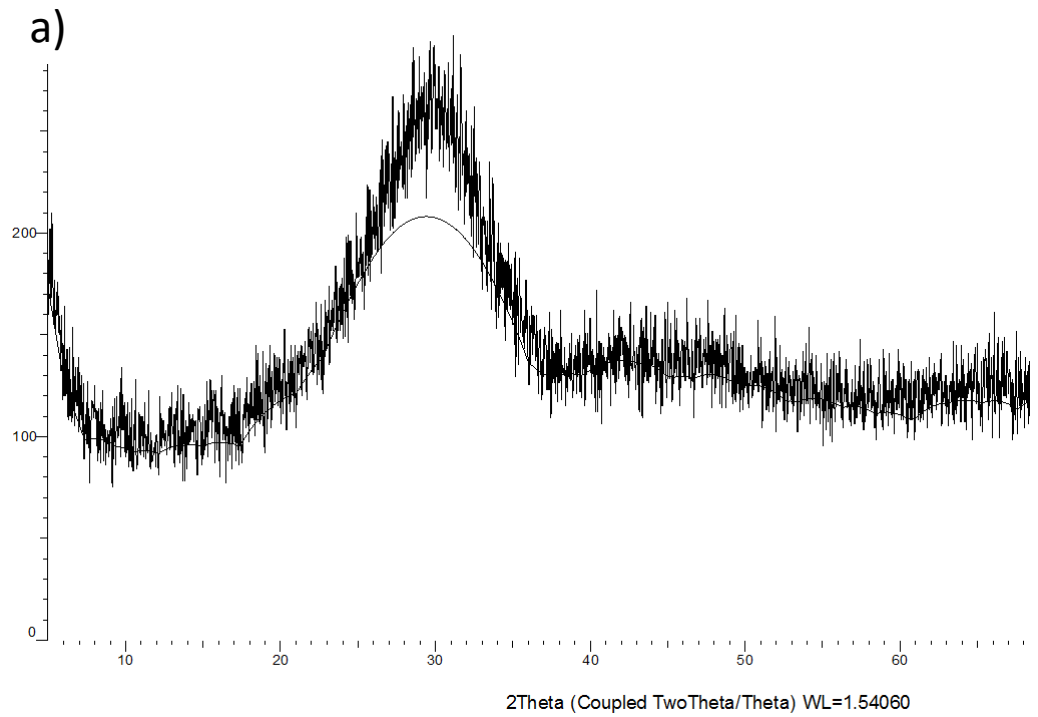

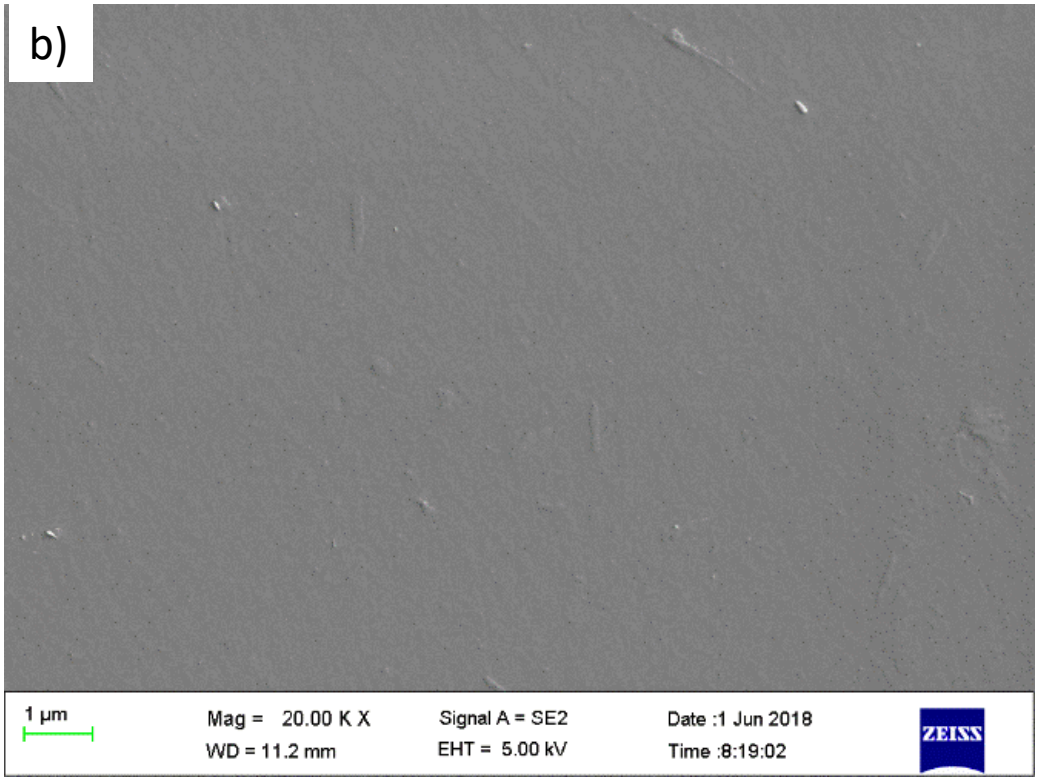

Figure 4.9: a) XRD pattern of cast pyrophyllite sample, b) SEM backscatter image of cast pyrophyllite.

The compositional analysis as determined using EDX (Figure 4.10) correlated to the expected composition calculated in Chapter 3. Figure 4.10 shows the composition in wt. % of Mixture 2 which contained 53 wt. % pyrophyllite and 47 wt. % calcium carbonate.

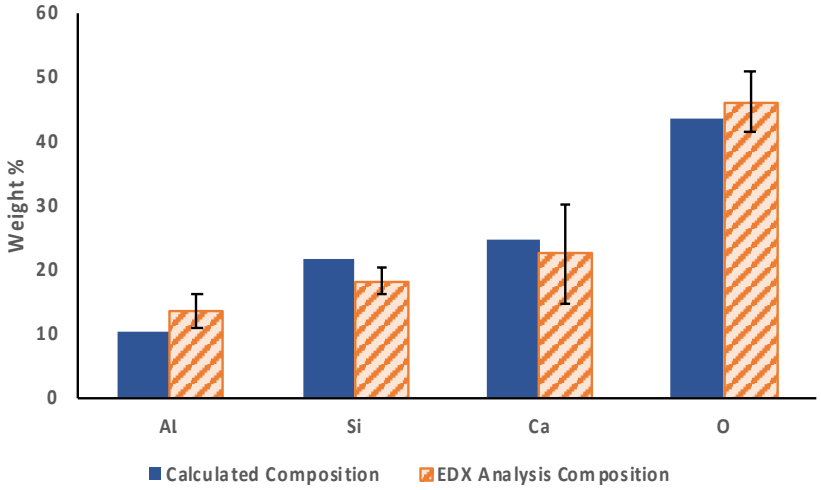

Figure 4.10: Expected composition vs analysed composition of samples with CaO additives.

4.3. Mechanical Tests

Mechanical tests were performed on the cast samples. The results for the hardness of the cast samples, however, was significantly lower than those reported in literature for basalt (BMW Steels Ltd, n.d.).

Table 4.2: Material properties of cast samples vs basalt.

Material	**Pyrophyllite samples with CaO additives, as cast**	**Cast basalt (literature)** (Schultz, 1993) (BMW Steels Ltd, n.d.)
Density g/cm^3	**2,89±0,09**	**2,8-3,0**
Hardness GPa	**5,77±0,31**	**6,87-7,85**

The glass ceramics therefore had to be recrystallized to improve their properties. This was based on experiments by Duan and Liang that proved that heat treatment has a significant effect on the structure and function of glass-ceramics, and by controlling the process of heat-treatment materials having high strength and good toughness can be prepared (Duan & Liang, 1998) .

The recrystallisation technique chosen involved heating the samples to 900°C for 2 hours followed by an increase in temperature to 1040°C for 2 hours. This method ensured that phase separation of the glass at the lower temperature occurred. This separation accelerated the nucleation rate and crystal growth (Duan & Liang, 1998). Materials with uniform and fine crystals are then produced during the high temperature heating phase.

Crystallized samples greenish white in colour and opaque were produced (Figure 4.11). From Figure *4.12* it was noted that the pyrophyllite powder with calcium oxide additives was mainly transformed into anorthite ($CaAl_2Si_2O_8$) and gehlenite (Ca_2Al [$AlSiO_7$]) phases.



Figure 4.11: Crystallized cast pyrophyllite.

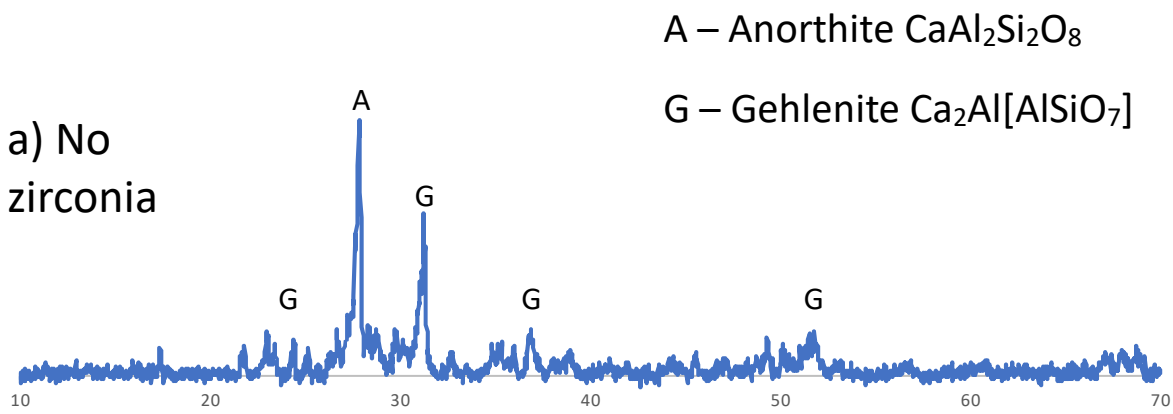

Figure 4.12: XRD pattern of crystallized cast pyrophyllite.

4.3.1. Yttria-stabilised zirconia

The procedure used to produce the crystallized samples was a heat and time intensive two-step process. Kingery's research showed that a nucleating agent such as zirconia, titanium oxide or chromia added to the CAS (CaO-Al_2O_3-SiO_2 - Calcium oxide alumino-silicate) system of ceramic glass can crystallize the whole body (Kingery, et al., 1983)

To remove the requirement of multiple further heating cycles yttria-stabilised zirconia was added to induce crystallization in the cast pyrophyllite samples during cooling. Using the compositions selected in Table 3.4 samples with increasing zirconia content (1 to 10%) were melted at 1400°C and cast into pyrophyllite moulds.

Upon casting, samples with 1 to 5% zirconia were transparent and amorphous when cast whilst samples with 8% zirconia showed a partial colour change. Although 10% zirconia samples were opaque with a whitish green colour, they were also not crystalline.

Recrystallization was subsequently attempted at 900°C, 950°C, 1000°C, 1050°C and 1100°C degrees for 2 hours. The results are presented in Table 4.3.

Table 4.3: Crystallization matrix.

		Compositions in wt. %				
Casting temperature	Crystallisation temperature and duration	Composition 1 1% Zirconia	Composition 2 3% Zirconia	Composition 3 5% Zirconia	Composition 4 8% Zirconia	Composition 5 10% Zirconia
1400°C Melt/Cast	No additional crystallisation	No Crystallization	No Crystallization	No Crystallization	Partial Colour Change/ No Crystallization	Colour Change/No Crystallization
1400°C Melt/Cast	+ 900°C for 2hr	No Crystallization	No Crystallization	No Crystallization	Partial Colour Change/ No Crystallization	Colour Change/No Crystallization
1400°C Melt/Cast	+ 950°C for 2hr	No Crystallization	No Crystallization	No Crystallization	Partial Colour Change/ No Crystallization	Colour Change/No Crystallization
1400°C Melt/Cast	+ 1000°C for 2hr	No Crystallization	No Crystallization	No Crystallization	Partial Colour Change/ No Crystallization	Colour Change/No Crystallization
1400°C Melt/Cast	+ 1050°C for 2hr	Surface Crystallization	Surface Crystallization	Surface Crystallization	Surface Crystallization	Surface Crystallization
1400°C Melt/Cast	+ 1100°C for 2hr	Full Crystallization	Full Crystallization	Full Crystallization	Full Crystallization	Full Crystallization

From Table 4.3 it was observed that the crystallization temperature was between 1050°C and 1100°C. Crystallization also occurred in all samples including the sample with 1 wt. % Zirconia. The XRD patterns of recrystallized samples crystallized with increasing zirconia content are presented in Figure 4.13.

A – Anorthite $CaAl_2Si_2O_8$

G – Gehlenite $Ca_2Al\ [AlSiO_7]$

W - Wollastonite $CaSiO_3$

a) No zirconia

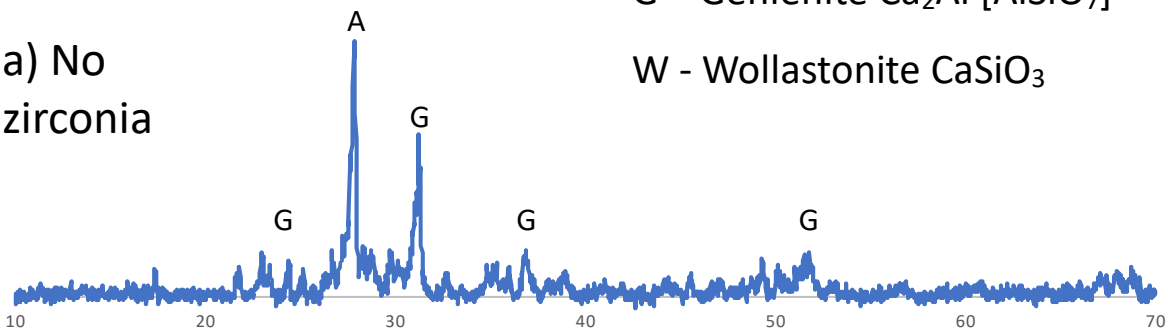

b) 1% added zirconia

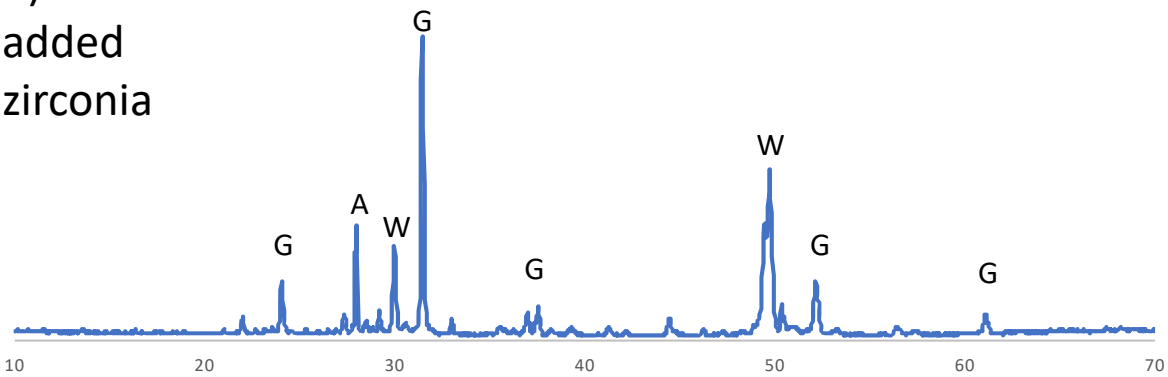

c) 3% added zirconia

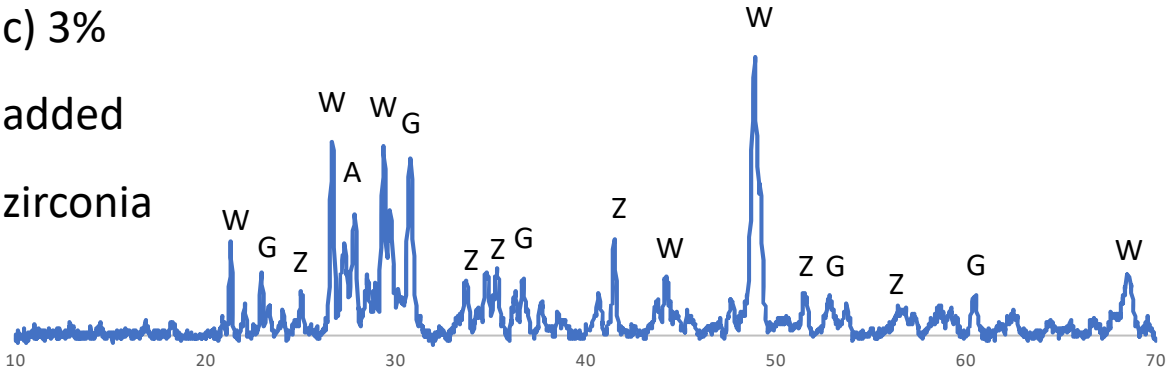

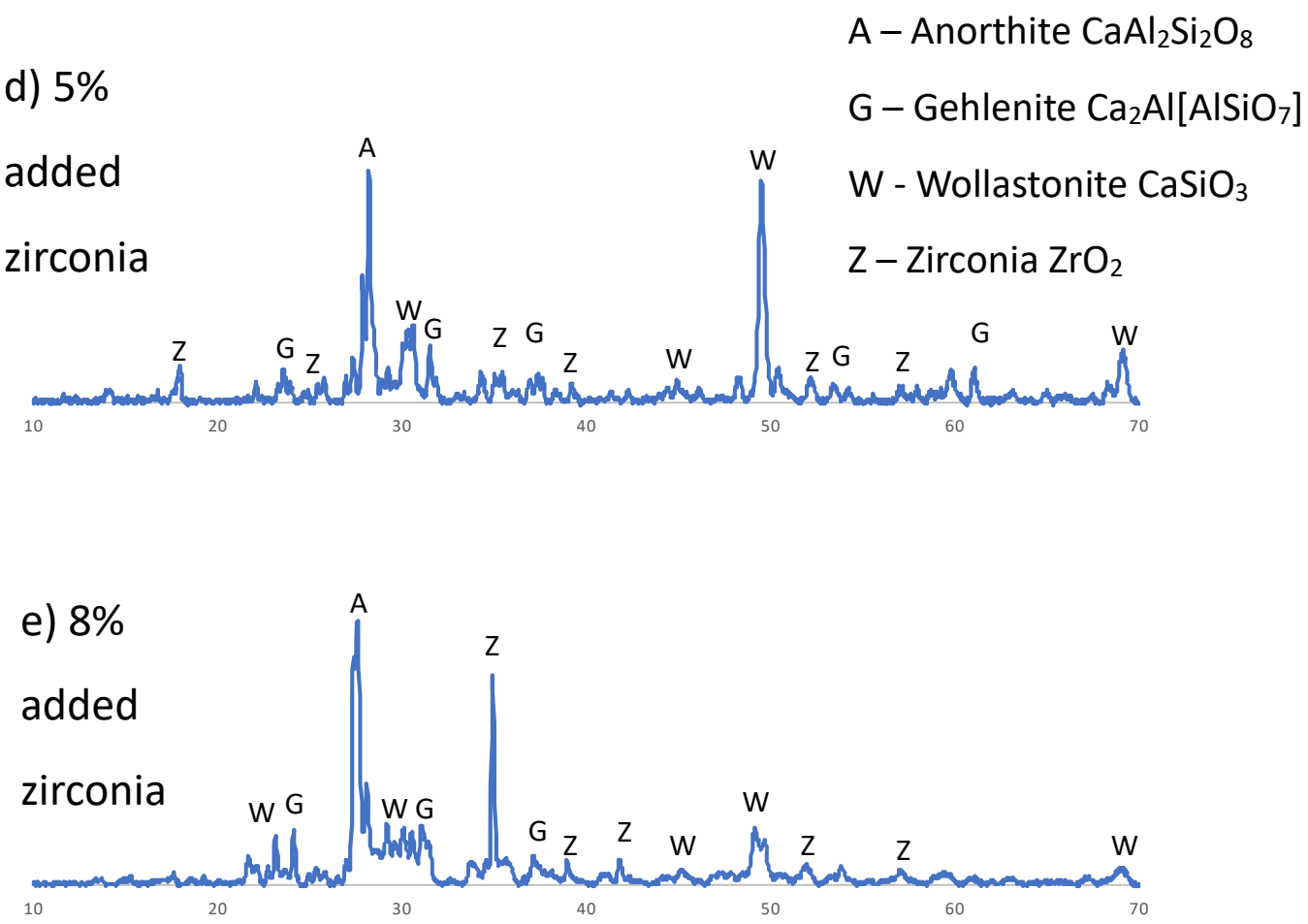

Figure 4.13: XRD pattern of crystallized cast pyrophyllite a) without zirconia and with added zirconia of b) 1 wt. % c) 3 wt. % d) 5 wt. % e) 8 wt. %.

From (Figure 4.13 a) the pyrophyllite powder with calcium oxide additives was mainly transformed into anorthite ($CaAl_2Si_2O_8$) and gehlenite (Ca_2Al [$AlSiO_7$]) phases. No pyrophyllite or calcium oxide peaks were evident after crystallization.

There is, however, a significant change in the diffractogram with the added zirconia. The gehlenite phase is dominant in the scan of the 1% zirconia sample (Figure 4.13 b) with a high peak at 32°. This gehlenite peak reduced in intensity with the added zirconia. A third phase of wollastonite ($CaSiO_3$) was also identified with a characteristic peak at 30° and 50°. The anorthite phase peaks maintain their relative intensity throughout all the diffractograms. At even higher zirconia content (5% and 8%) a characteristic zirconia peak increases in intensity at 35°.

Based on this information a single cycle process with melting followed by casting into a preheated pyrophyllite mould was attempted. The mould was heated to white hot using an oxy acetylene torch. Samples with 1% zirconia were then cast into the preheated mould and the oxyacetylene torch was held in place for an additional 30 minutes. Crystallization was however unsuccessful. This could have been due to the inaccuracy of the temperature profile produced using the oxyacetylene torch. Samples cast using this method therefore remained fully amorphous.

4.4. SEM

SEM micrographs of the crystallized pyrophyllite samples without zirconia are presented in Figure 4.14. Very little porosity was observed in the sample. At low magnification the microstructure was visible with small tightly packed grains (Figure 4.14a). Closely distributed needle like crystals were predominant with an average grain size of ≈60 µm and a crystal matrix in lighter grey (Figure 4.14b).

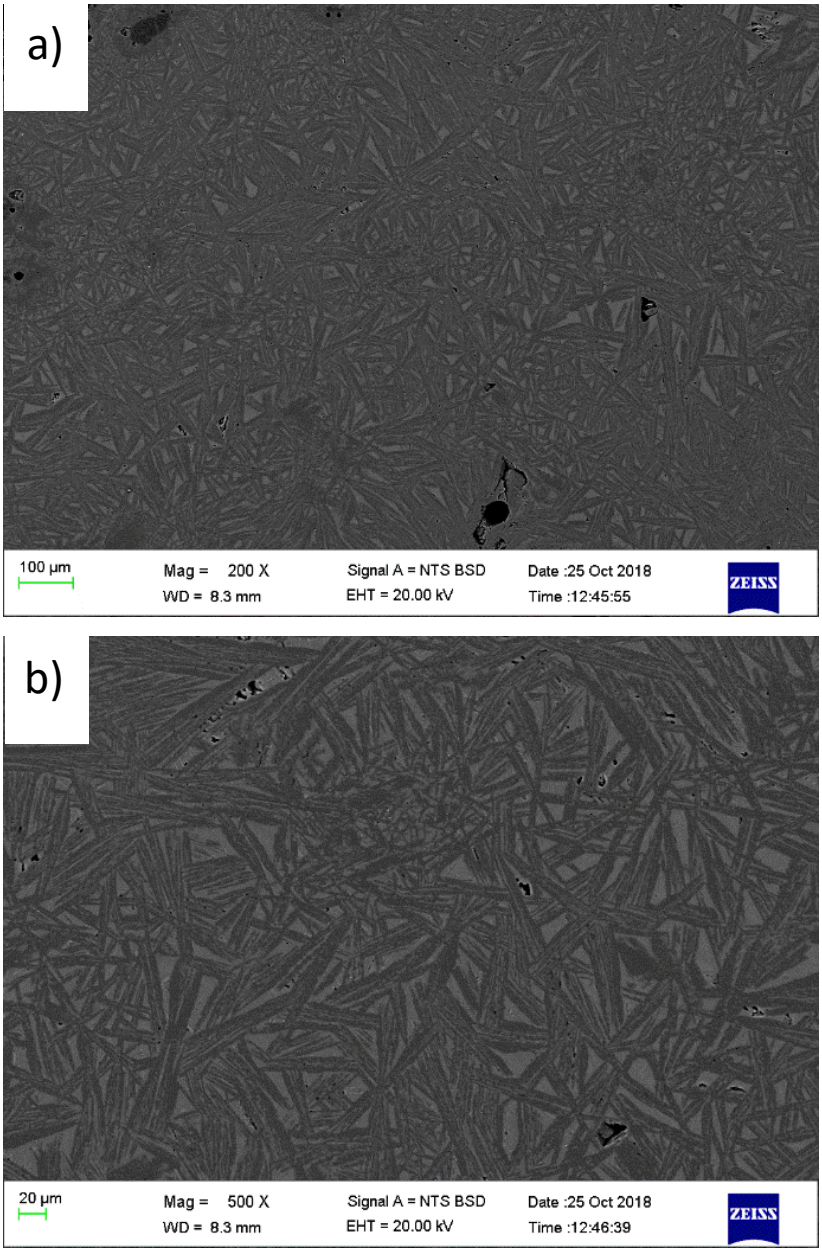

Figure 4.14: SEM Micrographs of crystallized cast pyrophyllite at a) low magnification b) high magnification.

To determine the crystals present, energy dispersive X-ray spectroscopy (EDX) analysis was carried out to identify the elemental composition of the sample. EDX area scan on a large area (Figure 4.15) revealed oxygen, aluminium, silicon and calcium which correlated to the base composition of the melt.

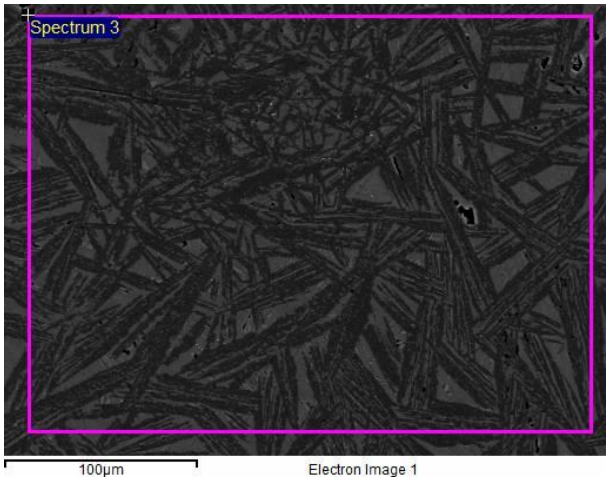

Element	EDX (wt. %)	Mix. (wt. %)
O	42,35	43,51
Al	13,38	10,32
Si	23,29	21,49
Ca	20,98	24,67
Total	100,00	100,00

Figure 4.15: Overall EDX analysis of crystallized cast pyrophyllite.

EDX point scan of the needle like crystals revealed an elemental composition that correlated with the composition of anorthite as shown in Figure 4.16a. Similarly, EDX analysis of the lighter grey phase correlated with the composition of gehlenite (Figure 4.16b).

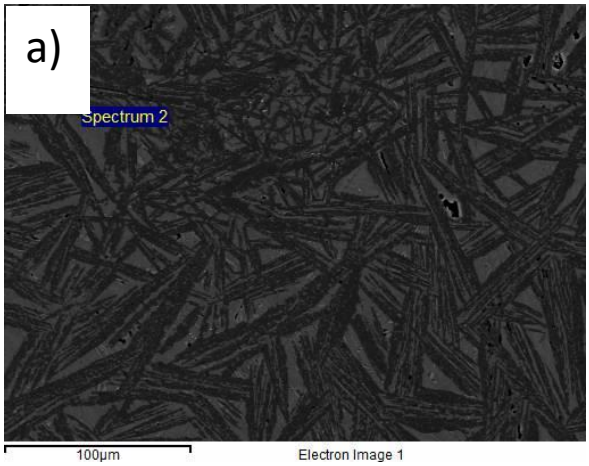

Element	EDX (wt. %)	Mix. (wt. %)
O	40,06	46,01
Al	19,91	19,40
Si	23,29	20,19
Ca	16,73	14,41
Total	100,00	100,00

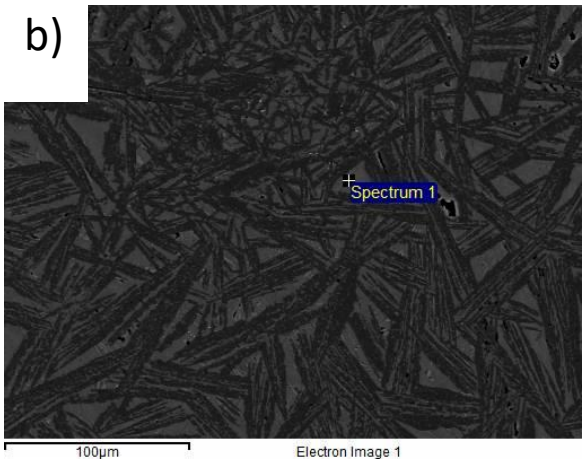

Element	EDX (wt. %)	Gehlenite (wt. %)
O	42,62	40,85
Al	17,10	19,68
Si	14,81	10,24
Ca	25,45	29,23
Total	100,00	100,00

Figure 4.16: EDX analysis of crystallized cast pyrophyllite at a) point scan of dark grey phase b) point scan of light grey phase.

The microstructure of the pyrophyllite samples crystallized with 1% zirconia was similar to the sample without zirconia (Figure 4.17a). This sample, however showed a population of more loosely distributed crystals when compared to the sample without zirconia. At higher magnification, (Figure 4.17b) dark grey needle like crystals were visible with an average grain size of ≈60 µm together with smaller light grey needle like grains visible in a light grey crystal matrix. Bright dots were also scattered throughout the backscatter image.

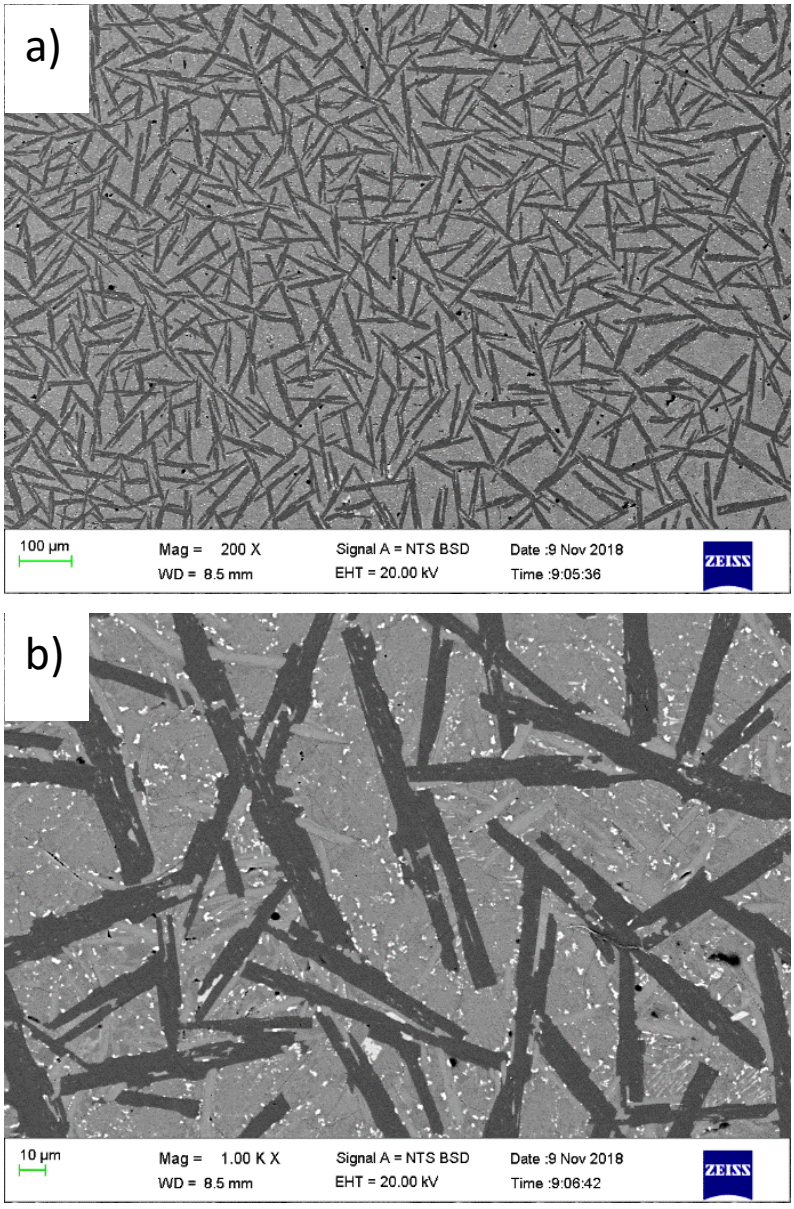

Figure 4.17: SEM Micrographs of cast pyrophyllite crystallized with 1% zirconia at a) low magnification b) high magnification.

EDX analysis was used to detect the composition of the visible phases. The bright spots were identified as having 20 weight % Zirconia (Figure 4.18a). They were therefore identified as the zirconia nucleating sites. The dark grey phase was identified as anorthite (Figure 4.18b) whilst the light was identified as gehlenite (Figure 4.18c). The light grey needle like crystals were identified as wollastonite and were not present in the samples crystallised without zirconia.

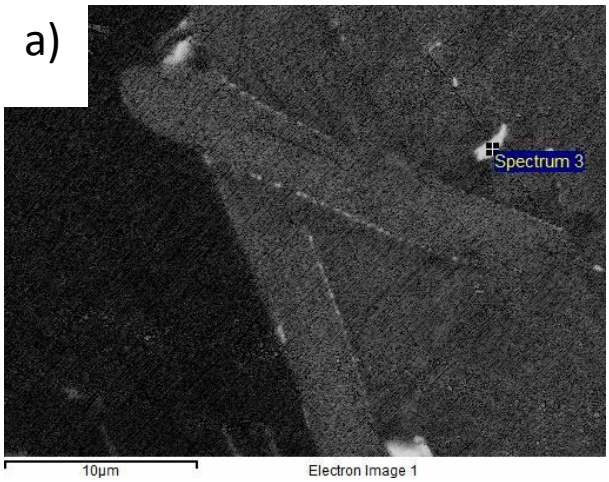

Element	EDX (wt. %)
O	35,63
Al	6,68
Si	14,16
Ca	22,96
Zr	19,67
Total	100,00

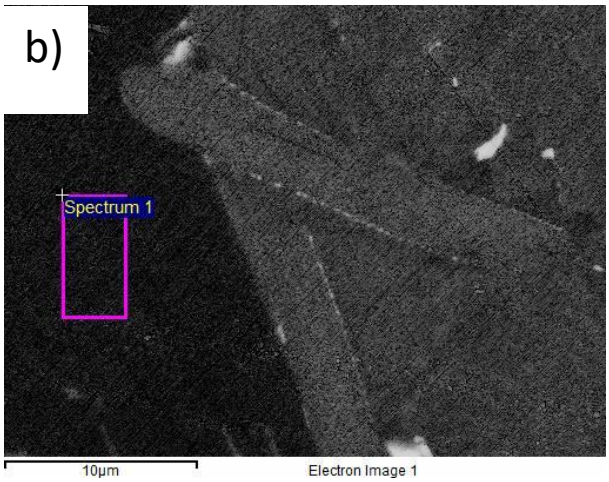

Element	EDX (wt. %)	Anorthite (wt. %)
O	41,87	46,01
Al	19,52	19,40
Si	23,18	20,19
Ca	15,43	14,41
Total	100,00	100,00

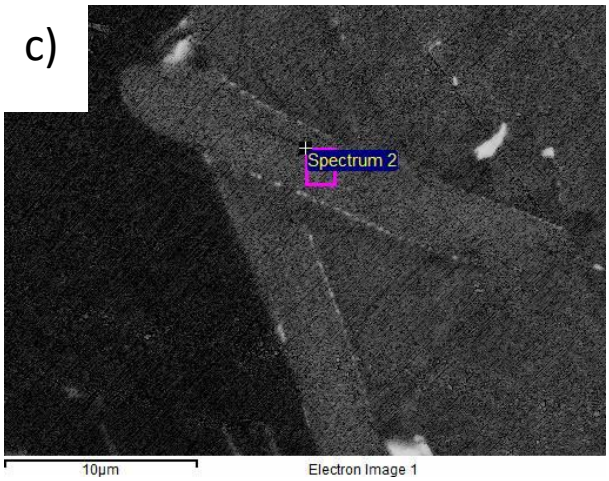

Element	EDX (wt. %)	Wollastonite (wt. %)
O	39,04	41,32
Al	10,44	0,00
Si	19,88	24,18
Ca	30,64	34,50
Total	100,00	100,00

Figure 4.18: EDX analysis of crystallized cast pyrophyllite with 1% zirconia at a) point scan of bright spot b) area scan of dark grey phase c) area scan of light grey phase.

Backscatter imagery of the sample cast with 10% zirconia before it was reheated showed that the sample remained amorphous. Only zirconia crystals were visible in the image and these were confirmed by both EDX (Figure 4.19a) and an XRD scan (Figure 4.19b).

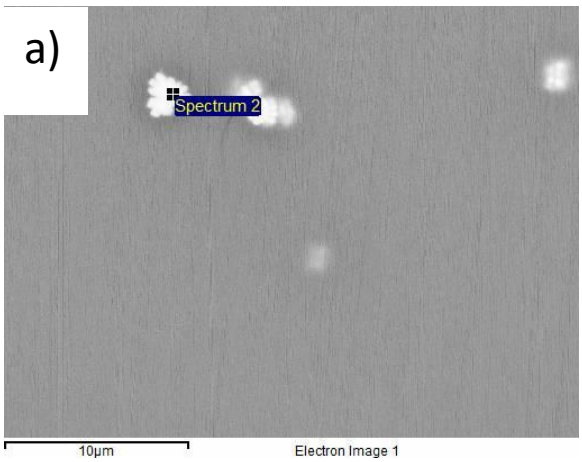

Element	EDX (wt. %)
O	35,63
Al	6,68
Si	14,16
Ca	22,96
Zr	19,67
Total	100,00

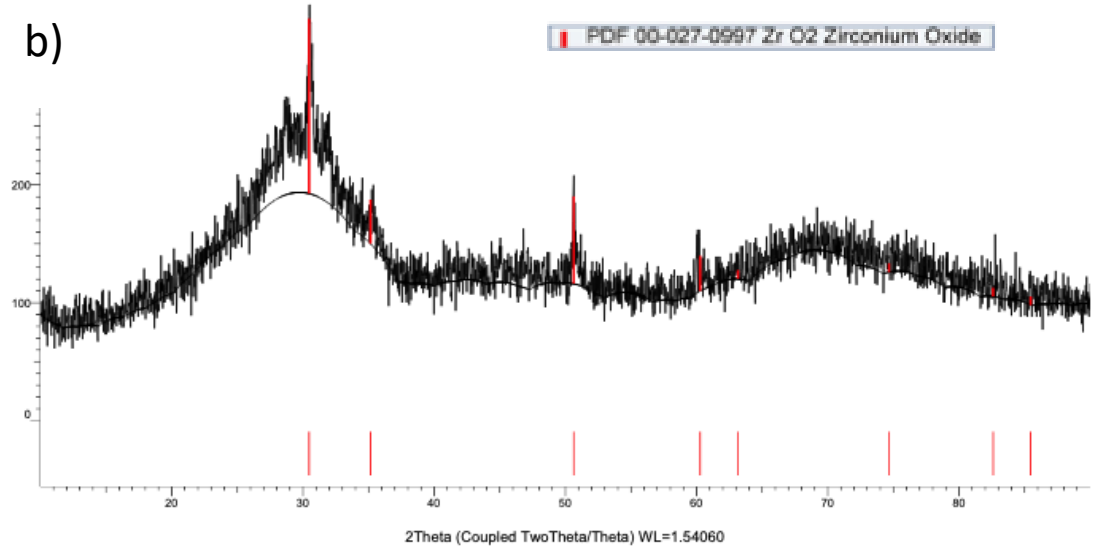

Figure 4.19: a) SEM backscatter of cast pyrophyllite with 10% zirconia b) XRD pattern of cast pyrophyllite sample 10% zirconia.

For the remaining recrystallised samples, with increased zirconia content an increase in the frequency and size of bright spots shown in Figure 4.20a and Figure 4.20b. The population and packing of the darker grey anorthite phase also increased with increased zirconia content (Figure 4.20). The size of these anorthite crystals, however, decreased.

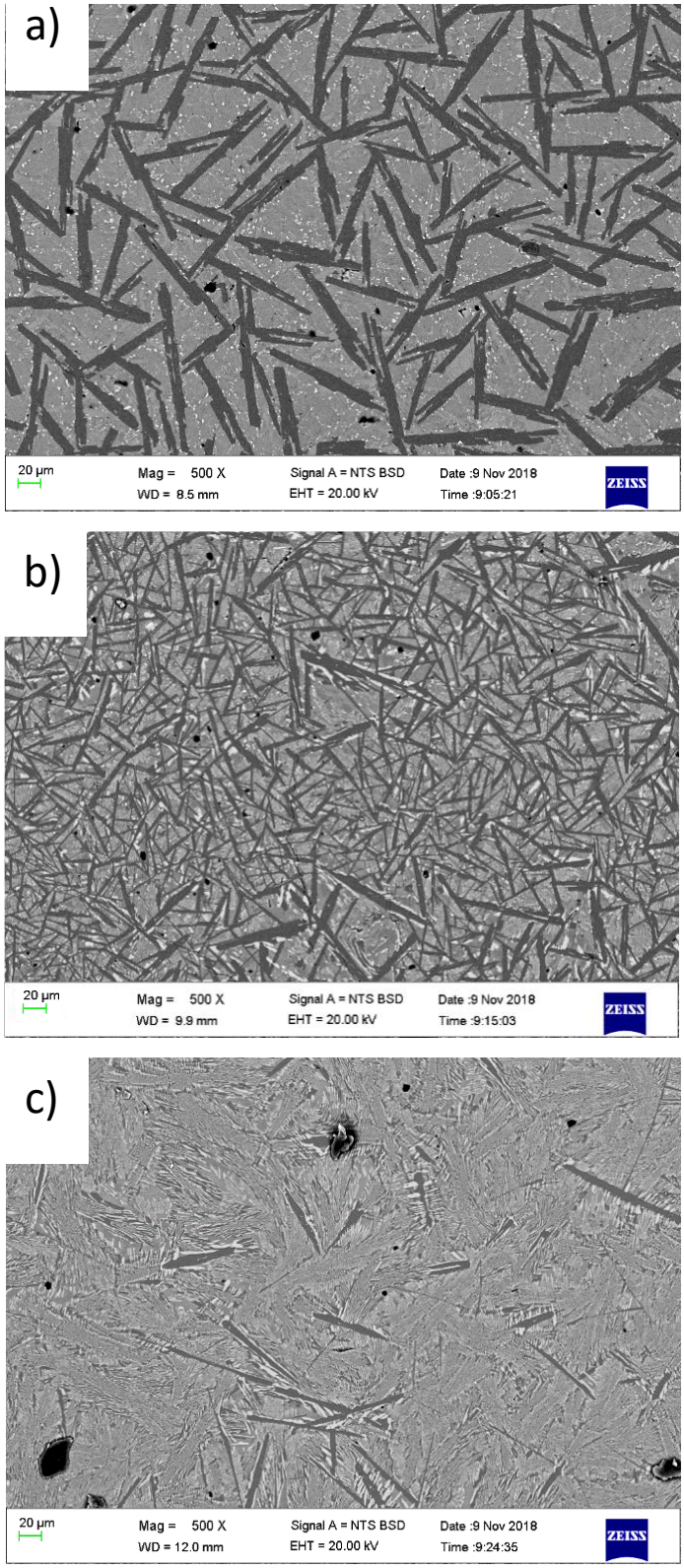

Figure 4.20: SEM Micrographs of crystallized cast pyrophyllite with added zirconia of a) 1 wt. %, b) 3 wt. % and c) 5 wt. %.

At higher magnification (Figure 4.21) the backscatter images showed the zirconia phase formed more elongated crystals with increased zirconia content.

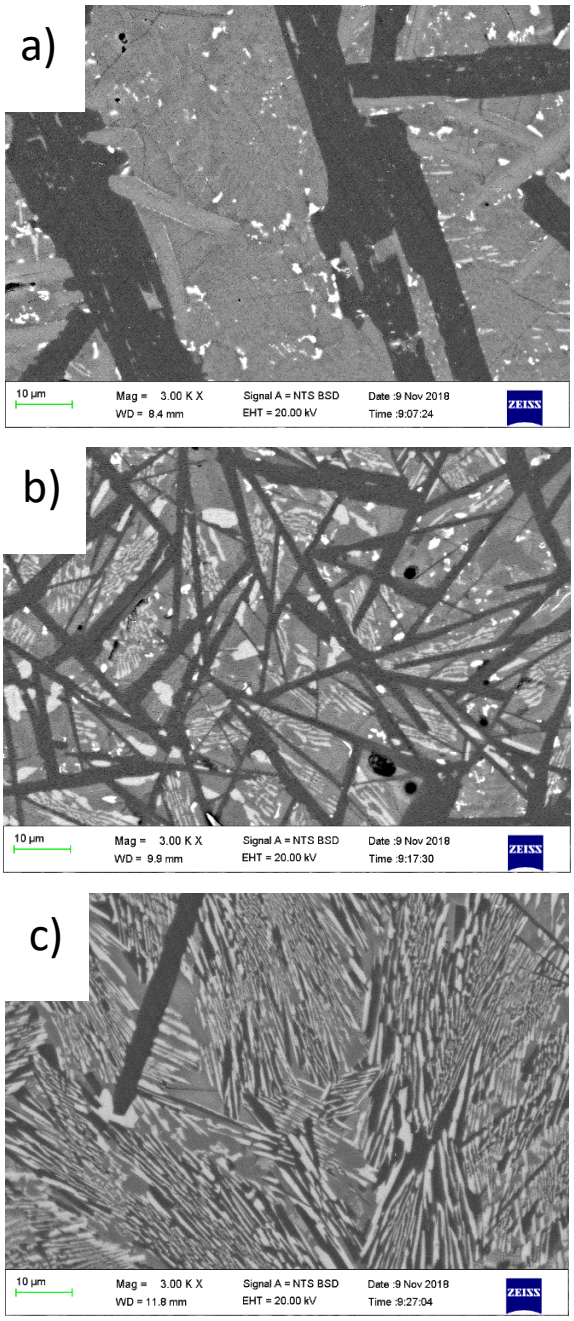

Figure 4.21: SEM Micrographs of crystallized cast pyrophyllite with added zirconia of a) 1 wt. %, b) 3 wt. % and c) 5 wt. %.

To determine the microstructural evolution with increased crystallization time the samples with 1% zirconia was crystallized at 1100°C for 3 and 4 hours. The SEM imagery was then compared to the sample crystallized for 2 hours. Very minor changes in the

population of anorthite grains was observed with increased heating time (Figure 4.22). The very light grey wollastonite grains, however, increased with increasing holding time (Fig. 4.22).

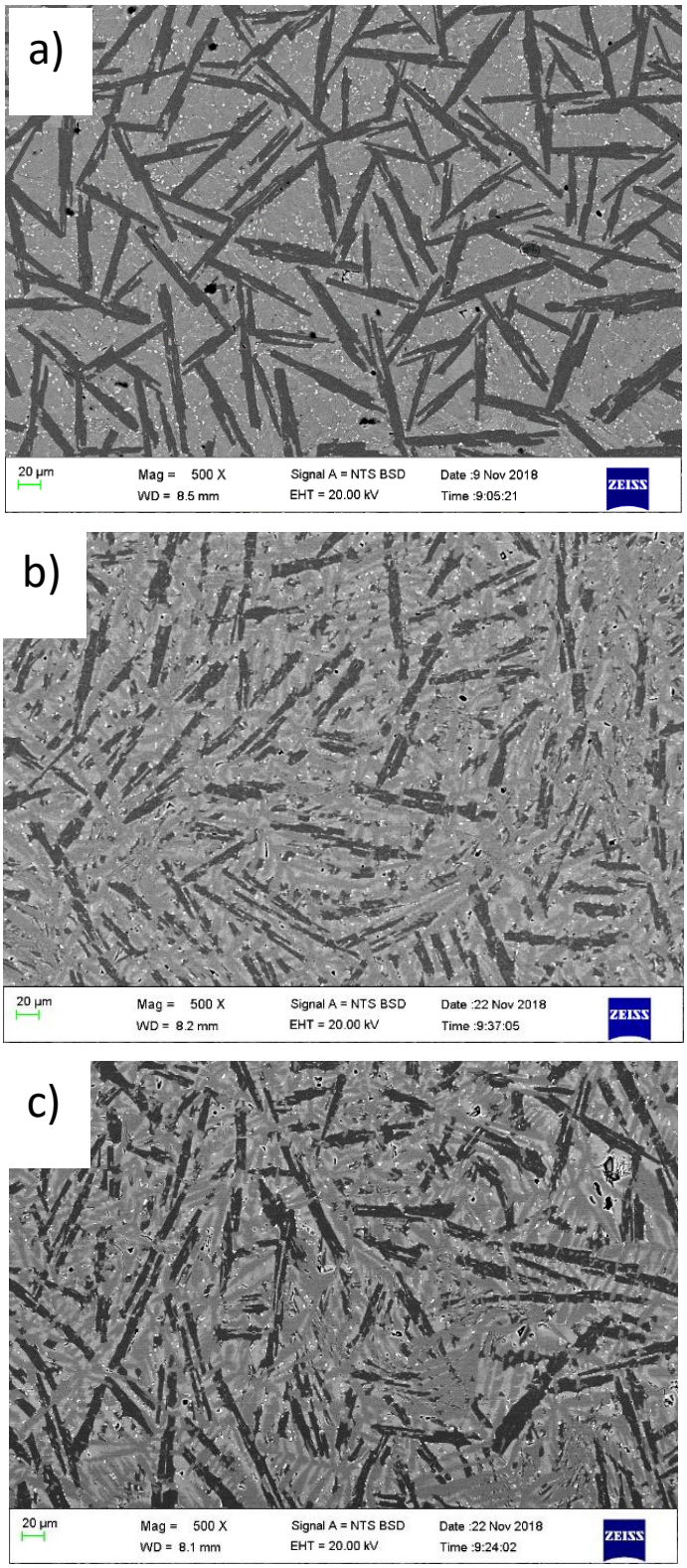

Figure 4.22: SEM Micrographs of crystallized cast pyrophyllite with 1% added zirconia heated at 1100°C for a) 2hr, b) 3 hr and c) 4hr.

The XRD patterns of these samples (Figure 4.23) confirmed this, revealing the characteristic gehlenite peak at 32° decreasing sharply with increased holding time and coinciding with an increased wollastonite peak. The Anorthite peaks, however, remain constant with increased holding time.

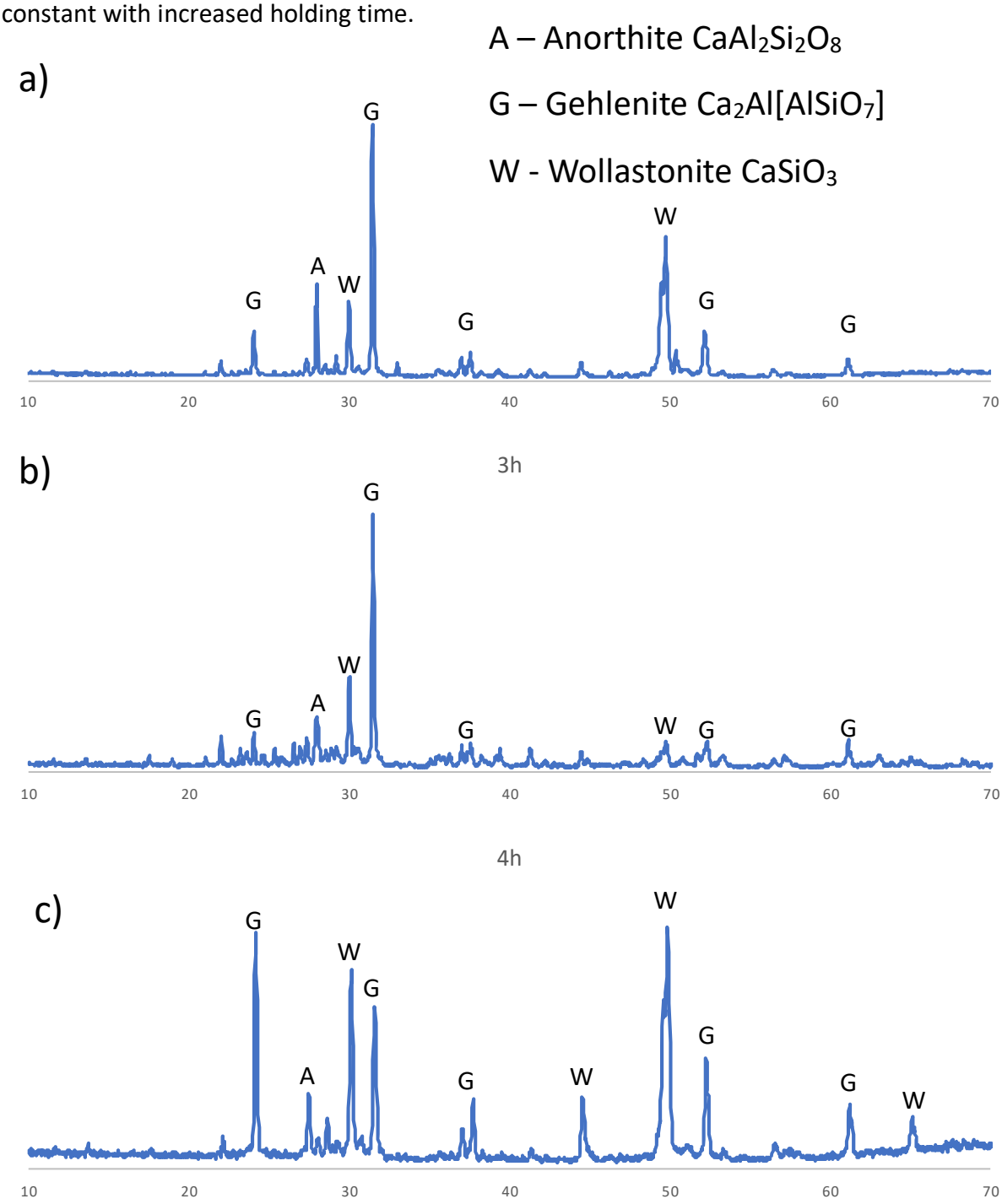

Figure 4.23: a) XRD pattern of crystallized cast pyrophyllite with added 1% zirconia and heated at 1100°C for a) 2hr, b) 3hr and c) 4hr.

4.5. Mechanical properties

The mechanical properties of both the crystallized and no crystallized samples were comparable to those of basalt reported in literature and determined experimentally. These results are presented in Table 4.4.

The Young's modulus used for calculating the fracture toughness of the cast pyrophyllite was calculated using the sheer wave, longitudinal wave and density measured using an Olympus 45MG thickness gauge. The Young's modulus value for basalt was obtained from literature (Schultz, 1993).

Table 4.4: Material properties of cast samples vs basalt.

Material	**Pyrophyllite samples with CaO additives, as cast**	**Crystallized cast pyrophyllite samples**	**Cast basalt tiles (from supplier)**	**Cast basalt (industrial standards)** (Schultz, 1993) (BMW Steels Ltd, n.d.)
Density (g/cm^3)	**2,89±0,09**	**2,85±0,01**	**4,83±0,07**	**2,8-3,00**
Hardness (GPa)	**5,77±0,31**	**6,95±0,20**	**7,35±0,42**	**6,87-7,85**
Fracture toughness ($Mpa.m^{1/2}$)	**0,99±0,08**	**2,74±0,19**	**0,94±0,12**	**---**

From Table 4.4 both the hardness and fracture toughness for the cast pyrophyllite samples increased when the samples were crystallized. For the crystallized samples the hardness obtained was comparable to both the theoretical and measured hardness of basalt. The fracture toughness of crystallized cast pyrophyllite without zirconia was significantly higher than the fracture toughness of the cast basalt tiles.

The material properties of the pyrophyllite samples crystallized using zirconia as a nucleating agent were also determined and are presented in Table 4.5.

Table 4.5: Material properties of cast samples crystallized with added zirconia.

Material	**Composition 1 1% Zirconia**	**Composition 2 3% Zirconia**	**Composition 3 5% Zirconia**	**Composition 4 8% Zirconia**	**Composition 5 10% Zirconia**
Density (g/cm^3)	**2,83±0,01**	**2,89±0,01**	**2,91±0,01**	**2,95±0,01**	**2,99±0,01**
Hardness (GPa)	**6,18±0,08**	**6,33±0,39**	**6,47±0,18**	**6,31±0,36**	**6,53±0,18**
Fracture toughness ($Mpa.m^{1/2}$)	**1,12±0,19**	**1,11±0,20**	**0,93±0,07**	**0,95±0,18**	**0,77±0,09**

Yttria stabilised zirconia has a high density of about 6,1 g/cm^3. This resulted in the density of the crystallized pyrophyllite material increasing with increased doping of zirconia. The hardness values obtained for the samples also increased with added weight percent of zirconia. This correlated with the decreasing size of the anorthite grains shown in the SEM micrographs (Figure 4.20).

With increased holding time at 1100°C there was no significant difference in the material properties of the sample cast with 1% zirconia. Both the hardness and fracture toughness of all the samples were, nonetheless, comparable to the industrial standards (Schultz, 1993) (BMW Steels Ltd, n.d.) and measured properties of cast basalt.

Table 4.6: Material properties of cast samples crystallized with 1% added zirconia at 1100°C with increasing time.

Material	**Composition 1 1% Zirconia**	**Composition 1 1% Zirconia**	**Composition 1 1% Zirconia**
Heat treatment time at 1100°C (hours)	**2**	**3**	**4**
Density (g/cm^3)	**2,83±0,01**	**2,83±0,01**	**2,83±0,01**
Hardness (GPa)	**6,18±0,08**	**6,14±0,38**	**6,13±0,28**
Fracture toughness ($Mpa.m^{1/2}$)	**1,12±0,19**	**1,17±0,22**	**1,06±0,30**

CHAPTER 5: DISCUSSION

This section presents a detailed discussion of the results presented in Chapter 4. This includes properties of the raw materials, morphology of the cast samples and their mechanical properties as compared to industrial basalt plates.

5.1. Properties of pyrophyllite raw material

5.1.1. Thermal behaviour

Pyrophyllite is a hydrous aluminosilicate with 5% of its mass on average being water (Mukhopadhyay, et al., 2010). When heated to temperatures above 500°C a dehydroxylation reaction occurs. This produces the dehydroxylated phase of pyrophyllite. Literature by Kwon and Newton observed the average dehydroxilation temperature of pyrophyllite as being around 560°C (Kwon & Newton, 2016). (Mukhopadhyay, et al., 2010) also concluded that the dehydroxylation reaction of pyrophyllite occurs between 560°C and 580°C. DTA analysis of the pyrophyllite powder sample used in this research, however, showed an endothermic peak at 526°C (Figure 4.1). This difference could be attributed to the reduced particle size of the pyrophyllite powder. In general grinding of the clay materials results in changes in their material properties (Pérez-Rodríguez, et al., 1988). Mechanical treatment of pyrophyllite in particular results in a shift of its endothermic peak from 760°C to 540°C according to work by Perez Maqueda et al. (Pérez-Maqueda, et al., 1993). This correlates with the data produced in this work for the pyrophyllite samples examined, Figure 4.1. In this figure the endothermic peak that was attributed to the dehydroxilation reaction has an onset at 493,7°C and ends at 551,7°C.

The dehydroxylation reaction by definition results in the loss of water from the pyrophyllite molecule. The chemical reaction for this process is:

$$\mathrm{Al_2Si_4O_{10}(OH)_2} \rightarrow \mathrm{Al_2Si_4O_{11}} + H_2O$$

Based on this reaction the theoretical mass loss of the dehydroxylation reaction is therefore 5% of the original pyrophyllite mass (Table 5.1). This correlates with the mass loss shown in the DTA curve for pure pyrophyllite (Figure 4.1).

Table 5.1: Calculation of weight loss due to dehydroxilation reaction.

Compound		Molecular weight	Molecular weight of compound/ Molecular weight of pure pyrophyllite
Pyrophyllite	$Al_2Si_4O_{10}(OH)_2$	360.31	100%
Dehydroxylated Pyrophyllite	$Al_2Si_4O_{11}$	342.30	95%
Water	H_2O	18,02	5%

5.1.2. Effects of admixtures on thermal behaviour

The DTA curves presented with admixtures all showed three similar endothermic peaks (Figure 4.2 and Figure 4.5). The first peak occurred at temperatures around 526°C. This peak was similar to the peak described in section 5.1.1. and correlated to the dehydroxylation reaction of the pyrophyllite.

The second set of peaks occurred between 600°C and 850°C. Research by Galan et al., has shown that calcium carbonate decomposes at elevated temperatures to calcium oxide and carbon dioxide (Galan, et al., 2013). This decomposition occurs at temperatures from 680°C to 875°C (Rao, 1996) and is an endothermic reaction (Galan, et al., 2013). The second endothermic peak in the thermograph therefore correlated to this decomposition reaction. Similarly, in the samples with sodium carbonate additive the second endothermic peak correlated with the decomposition reaction to sodium oxide which completes at around 800°C.

The third peaks at 1300°C (Figure 4.2 and Figure 4.5) correlated to the melting reactions of each additive mixture as determined from their ternary phase diagrams (Figure 3.2).

The thermographs showed that the melting point temperatures decreased with increased concentrations of both calcium carbonate and sodium carbonate additives.

This implies that the eutectic point of the mixtures was closer to higher concentrations of the admixtures and also correlated with the ternary phase diagrams (Figure 3.2) for the admixtures. From the literature reviewed the lowest melting point possible of different compositional mixtures of the two solids is known as their eutectic point (Nordlie, 1989). For the materials examined in this work the eutectic temperature is 1300°C.

5.2. Phase and Microstructural analysis

5.2.1. XRD Analysis

To confirm the hypothesis that the as cast pyrophyllite samples were amorphous XRD analysis was carried out. The diffractogram produced showed a broad and shallow peak (Figure 4.9a). This is characteristic of an amorphous glass material which was also observed by Marques et al., (2006).

Strength is an important factor in glass ceramics (Wang, et al., 2020). Duan and Liang proved that heat treatment has a significant effect on the structure and function of glass-ceramics, and by controlling the process of heat-treatment, materials having high strength and good toughness can be manufactured (Duan & Liang, 1998) .

In this research the recrystallisation technique chosen involved heating the samples to 900°C for 2 hours followed by an increase of temperature to 1040°C for 2 hours. This followed the work of Duan and Liang who's two step crystallisation method ensured that phase separation of the glass at the lower temperature occurred. This separation accelerated the nucleation rate and crystal growth (Duan & Liang, 1998). Materials with uniform and fine crystals could then be produced during the high temperature heating phase.

At about 900°C the CaO-Al_2O_3-SiO_2 (or CAS) composite system glasses initially goes through a transition temperature for the glass T_g (Lo, et al., 2002). This temperature is determined by a change in the expansion behaviours of the CAS system resulting in a shift in its associated heat capacity behaviour. The expansion results from an increase in the mean atomic vibration amplitude between atoms which is a mechanism of thermal storage (Lo, et al., 2003).

The T_g for this specific CAS system was identified from the DTA as an endothermic trend with increasing temperature. At this temperature a typical non crystalline XRD pattern was generated with no significant peaks apparent indicating the glass remained amorphous. Instead, in this region, phase separation occurs in the structure of the glass with O^{2-} ions attracted to the Si^{4+} ions to form $(SiO_4)^{4-}$. Network modifiers also attract O^{2-} with a partial negative charge (non-bridge oxygen), and there is a tendency for these to bond with all available oxygens (Warren & Pincus, 1940).

These ions diffuse together from the uniform glass base and are arranged to become the structure of the crystals. The complex formed from this nucleation requires sufficient energy to become the crystal phases (Duan & Liang, 1998). This energy required corresponds to the crystallisation peak temperature T_p or T_x.

According to literature the ideal crystallization temperature for CAS systems is 1040°C (Duan & Liang, 1998). The diffractogram produced at this temperature showed major peaks at 28° and 32° corresponding to the characteristic peaks of anorthite and gehlenite (Figure *4.12*). This observation is also in agreement with Lo et al.'s study that showed that the predominant and major crystal phase in crystallised glass in the CAS system is Anorthite (Lo, et al., 2003).

Bhatty, Gard and Glasser also showed that in glass with compositions of 24% CaO; 35% Al_2O_3 and 42% SiO_2 anorthite and gehlenite were the phases present in the composite after crystallization (Bhatty, et al., 1970). This explains the similar phases observed in

Figure *4.12* as this study used almost similar compositions of 24% CaO; 23% Al_2O_3 and 53% SiO_2.

Additionally, ternary phase diagrams of the CAS system generated by Ball, et al., (1993) and Mao, et al., (2006) (Figure 5.1) show in detail the crystal phases that may be obtained using different compositions. With pyrophyllite as the base material in this study the ratio of alumina to silica was fixed. This study therefore varied the amount of calcium oxide present in the mixture. Different calcium oxide concentrations are represented by the lines running from the AL_2O_3-SiO_2 edge to the CaO vertex. The intersection of these lines with the line parallel to the AL_2O_3-SiO_2 edge represents the composition used in this study (24% CaO; 23% Al_2O_3 and 53% SiO_2).

The ternary phase diagram (Figure 5.1 a) shows that the composition selected corresponds to a region with the crystalline phases of anorthite and gehlenite (alternately named melilite) having vertices nearest to the composition. Anorthite is also notably the nearest crystalline phase to the selected composition. The second ternary phase diagram (Figure 5.1 b) shows that this composition also corresponds to a region where anorthite is the expect phase. Higher composition of CaO in this diagram correspond to gehlenite phase being the expected composition.

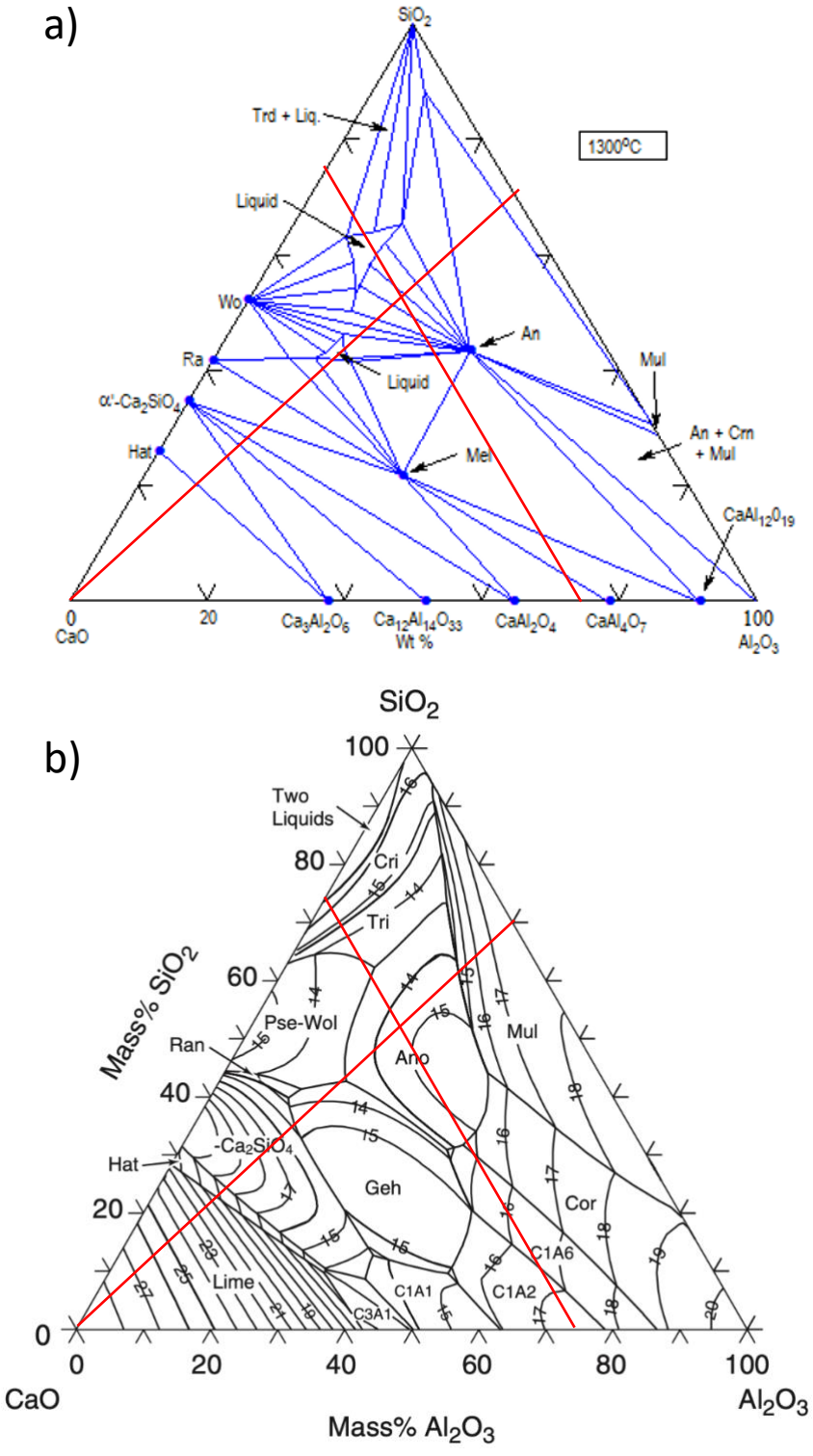

Figure 5.1: Ternary phase diagrams of the CAS system at a)1300C isotherm (Ball, et al., 1993) b) three phase equilibria (Mao, et al., 2006). An/Ano – anorthite; Pse-Wol/Wol – wollastonite; Geh/Mel gehlenite; Cor/Crn – corundum; Cri – cristobalite; Ran/Ra – rankinite; Mul – mullite; Tri/Trd – tridymite; Hat – hatrurite.

The two-step crystallization profile used to obtain these crystalline phases is both energy and time consuming and adds to increased manufacturing costs. It is, however, fairly typical of anorthite based ceramics which are known to be difficult to crystallise and require the addition of nucleating agents for crystallization (Lo, et al., 2002). Kingery's research also showed that glasses crystallize only on the surface when the content of SiO_2 is high, but if some nucleation agent, such as TiO_2, Cr_2O_3, SO_3, ZrO_2 or P_2O_5 are added to the glasses, they can crystallize in the whole body (Kingery, et al., 1983). These additions may also decrease the crystallization time and temperature of the phases (Ceylan, et al., 2010).

With the introduction of zirconia as a nucleating agent, the resulting diffractogram shows the anorthite peak almost disappearing (Figure 4.13) in comparison to the sample crystallised with no zirconia (Figure *4.12*). At the same time oxide phases such as gehlenite and wollastonite appear. The gehlenite peak in particular is most pronounced in the diffractogram. Lederer et al. observed similar behaviour in zirconia doped Mg-Ca-Al-Si-O-N glasses (Lederer, et al., 1998). Their study identified the main oxide phases of anorthite and spinel with gehlenite and zirconia phases formed with increased zirconia content. Similarly, Feng et al. used a CaO-Al_20_3-SiO system doped with zirconia but only up to 2,4 wt. % and obtained wollastonite as the main crystalline phase (Feng, et al., 2005).

For all the crystallised samples the crystallization temperature in this study was found to be between 1050°C and 1100°C (Table 4.3). At temperatures below 1050°C no crystallisation was found and diffractograms produced showed amorphous patterns. Surface crystallisation was observed at 1050°C with full crystallisation at 1100°C (Table 4.3). Research by Feng et al. working on a CAS system doped with zirconia had also similarly observed no obvious crystallisation below 950°C, weak wollastonite diffraction peaks at 1000°C, considerable peaks at 1050°C and the highest peak intensity at 1080°C (Feng, et al., 2005). Thus, the conclusion was that the addition of zirconia promoted crystallisation at relatively lower temperatures (Feng, et al., 2005).

It is of note that Feng et al. used a sintering method and a concentration of zirconia up to only 2,4 wt. %. Their research showed a small change with increased zirconia in the main crystalline phase formed (wollastonite). Similarly, in this research, increasing the zirconia content increased the wollastonite peak up to 3 % zirconia content (Figure 4.13). At higher zirconia contents however, the wollastonite peaks decreased. In contrast to that a significant peak at 35°, however, developed. This peak is a characteristic monoclinic zirconia peak (Lederer, et al., 1998) and increased in intensity with increased zirconia content. Research by Banijamali et al. using zirconia and titanium oxide as nucleating agents explains this as the precipitation of the zirconia compounds during the cooling phase, which are rendered as heterogeneous nuclei sites (Banijamali, et al., 2009).

At 10 wt. % the diffractogram showed a broad shallow peak indicating another amorphous state (Figure 4.19). Major peaks for zirconia were still identifiable at 32°, 35° and 51°. These peaks suggest that the material was not fully amorphous and crystalline zirconia particles were formed. Similarly, Lederer (1998) obtained crystalline samples only up to 8 wt. % Zirconia doped Mg-Ca-Al-Si-O-N glasses. Furthermore, DTA profiles of glass samples with increasing doping of nucleating agents including zirconia (SZ6), titanium oxide (ST) and calcium fluoride (SF) (Figure 5.2) showed that the increase in the nucleation agents decreased the melting point temperature from 1200°C at 6 wt. % in SF6 down to 1050°C at 12 wt. % in SF12 (Banijamali, et al., 2009). It can therefore be extrapolated that the increase of zirconia in the CAS system used in this study decreased the melting point temperature of the compound. This resulting in the samples with 10 wt. % zirconia melting when heat treated at 1100°C.

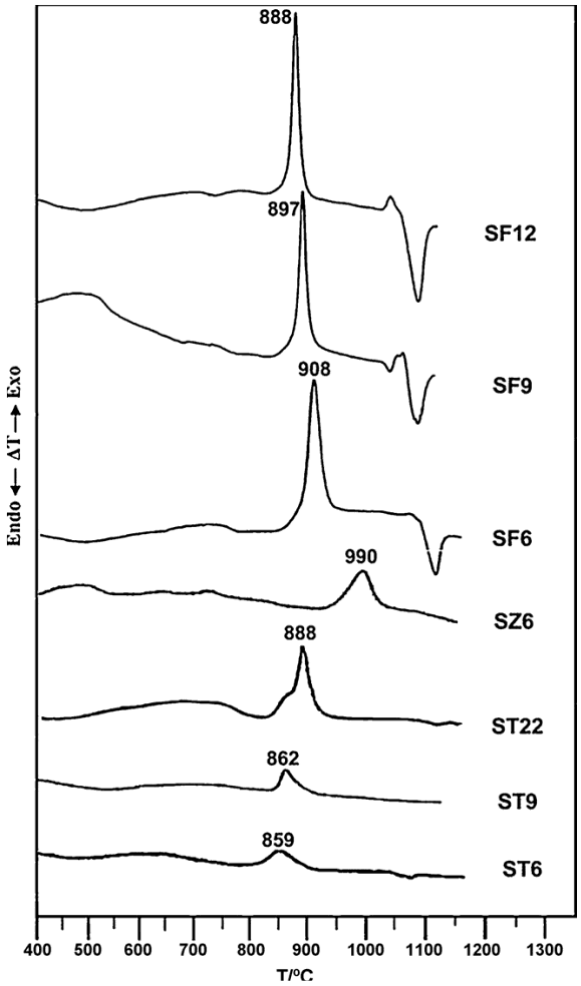

Figure 5.2: DTA profiles of glass samples doped with 6 wt. % zirconia (SZ6); 6, 9 & 22 wt. % titanium oxide (ST6, ST9 & ST22); 6, 9 & 12 wt. % calcium fluoride (SF6, SF9 & SF12) (Banijamali, et al., 2009).

The final set of diffractograms show the effect of heat treatment time on crystallisation. Using samples crystallised with 1 wt. % zirconia, increasing the holding time from 2 hours to 4 hours led to a decrease in the characteristic gehlenite peak at 32° (Figure 4.23). This coincided with an increase in both the triclinic wollastonite peaks and monoclinic ß-Wollastonite (27.5°, 45.6°, and 32°). By fixing the crystallisation time and increasing the temperature Abdul-Azam et al., obtained similar results with gehlenite phase at a lower temperature (800° and 1 000°C) and wollastonite phase at the higher temperatures (1150°C) (Abdul-Azam, et al., 2017). In this study however, the anorthite peaks remained constant with increased holding time (Figure 4.23).

5.2.2. SEM analysis

After pyrophyllite was successfully cast using calcium oxide as an additive SEM images were taken of the as cast samples. The SEM micrographs showed no visible crystals or microstructure (Figure 4.9 b). This meant that the samples had not crystallised during cooling. The ternary phase diagram for the calcium-alumino-silicate (CAS) system (Figure 5.1) indicated that the composition used in this research lay in the region where anorthite crystals were expected. As detailed in Section 5.2.1 however anorthite based ceramics are generally known to be difficult to crystallise (Lo, et al., 2002). This micrograph therefore further correlated the XRD pattern presented in Section 4.3.1 that showed a typical non crystalline pattern.

After heat treating the samples, based on the method described by Duan and Liang of a two-step crystallization process, at 900°C for 2 hours followed by an increase of temperature to 1040°C for 2 hours (Duan & Liang, 1998), crystalline samples were generated. Their SEM micrographs (Figure 4.14) showed a defined microstructure typical of the CAS compositions investigated. Needle like crystals were visible (Figure 4.14) and intertwined in a lighter grey crystal matrix. EDX spot analysis enabled chemical analysis of the crystals. The results showed that the estimated oxide content of the needle like grains corresponded approximately to stochiometric anorthite. Similarly, the light grey crystals corresponded to stoichiometric gehlenite. This corresponded to both the phases identified in the diffractograms produced by these samples (Figure *4.12*) and the ternary phase diagrams of the CAS systems presented in Figure 5.1.

To facilitate crystallization in the CAS system of glasses different nucleating agents could be employed (Banijamali, et al., 2009) and in this study zirconia was added to the samples to improve the crystallization. Samples generated with zirconia showed a similar heterogenous crystal makeup to the samples crystallised without zirconia (Figure 4.17). At 1 wt. % zirconia however XRD diagrams of these, however, identified a new crystal phase in the form of wollastonite (Figure 4.13). From the backscatter images these were identified using EDX analysis. The estimated oxide content of these new

grains corresponded to stoichiometric wollastonite (Figure 4.18). Zirconia was also identified as the white dots in the crystal matrix. Their presence in the residual crystal matrix serves as the heterogeneous nucleation sites and improves crystallization (Banijamali, et al., 2009).

Notably these zirconia nucleation sites were smaller than 2 microns in size and this resulted in the EDX point scan identifying Al, Si, and Ca ions in the surrounding crystals. This is because EDX analysis acquired on particles smaller than approximately 2 microns in size will often reflect the composition of the substrate supporting the particles as well as particles in close proximity (Kanegsberg & Kanegsberg, 2011). Also, of note in the SEM image was that the anorthite grains were noticeably fewer. This was due to the addition of zirconia changing the composition of the base melt and consequently the expected phase based on the ternary phase diagrams. Instead of anorthite the expected phases were wollastonite (Feng, et al., 2005) and gehlenite (Lederer, et al., 1998). This further corroborated the phases obtained in the diffractogram which showed a smaller anorthite peak in the samples crystallized with zirconia as compared to samples crystallized without (Figure 4.13).

With increasing zirconia content, the ZrO_2 crystals elongated and increased in population forming dendritic phases around the anorthite crystals (Figure 4.21). This was because the increased zirconium precipitated out as zirconia crystals (Banijamali, et al., 2009). This correlated with the increse in intensity of the characteristic zirconia peak observed in the diffractograms produced (Figure 4.13) for the samples with increased zirconia content. Concurrently, smaller grains of wollastonite and gehlenite also increased in population with increased zirconia replacing the larger anorthite crystals observed in samples crystallised without zirconia (Figure 4.20) and this was also correlated by the diffractograms produced (Figure 4.13).

At 10 wt. % zirconia content the glass was amorphous and only small acicular crystals could be observed (Figure 4.19). These were determined to be zirconia by EDX analysis

and correlated to the XRD diffractogram generated for the sample. Feng et al. described how the increase in zirconia content increased the crystallisation of the zirconia doped samples at lower temperatures (Feng, et al., 2005). Banijamali, et al. however also concluded that the increase in the nucleation agents including zirconia and titanium oxide decreased the melting point temperature from 1200°C at 6 wt. % down to 1050°C at 12 wt. % (Banijamali, et al., 2009). This implies that the samples with 10 wt. % zirconia heat treated at 1100°C melted instead of crystallised resulting in an amorphous glass with precipitated zirconia being formed. The ternary phase diagram for the CaO-SiO_2-ZrO_2 system (Figure 5.3), further confirms this as the composition used in this study correlated to a solid line which represents a point of 3 phase equilibrium/melting point (Mirhadi & Mehdikhani, 2011).

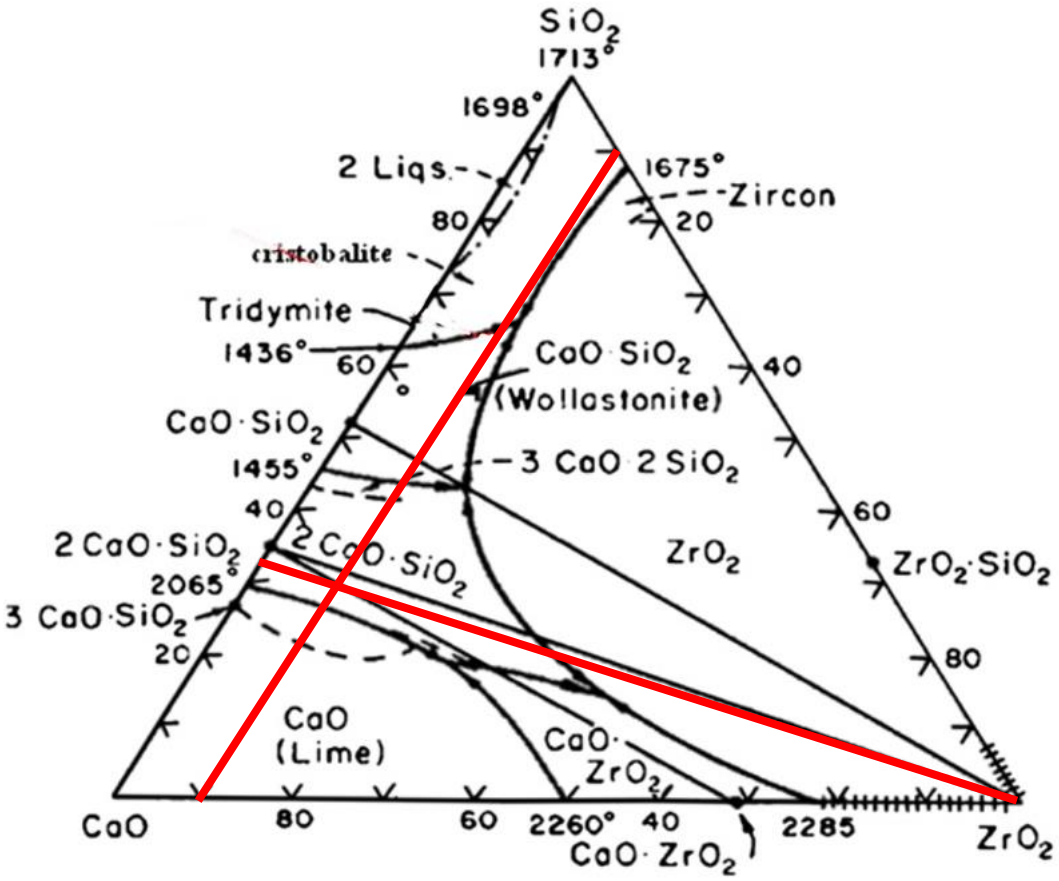

Figure 5.3: Ternary phase diagram of the CaO-SiO_2-ZrO_2 system (Mirhadi & Mehdikhani, 2011).

Increasing the heat treatment time of samples doped with 1 wt. % zirconia resulted in minor differences in the SEM micrographs produced (Figure 4.22). Lighter grey crystals identified by EDX analysis as wollastonite phase increased marginally with increased heat treatment time. XRD analysis showed similar results with an increase in the intensity of the wollastonite peaks produced (Figure 4.23). This means that the samples were fully crystallised at 2 hours and further heat treatment had negligible effect on the morphology of the samples. The DTA traces presented in Figure 5.2 show how the sample doped with zirconia produces the shortest exothermic peak of the nucleating agents tested. This means that less energy or enthalpy of crystallization (ΔH_c) is required to crystallise samples (Brittain & Bruce, 2006) doped with zirconia and consequently less holding time is required at the crystallisation temperature.

5.3. Mechanical Properties

The fracture toughness and hardness values of the as cast samples, crystallised and doped with zirconia are presented in Table 4.4 and Table 4.5. The as cast samples (before crystallization) showed comparable fracture toughness to cast basalt. The hardness values, however, of 5,77 GPA were significantly lower than the hardness values obtained from the industrially sourced basalt tiles.

Upon heat treating the cast samples using the procedure described by Duan and Liang (Duan & Liang, 1998), the hardness and fracture toughness for the cast samples increased as they crystallised. This direct correlation was expected based on the behaviour of glass ceramics which show increased strength and toughness with heat treatment (Duan & Liang, 1998). This is presented graphically in Figure 5.4.

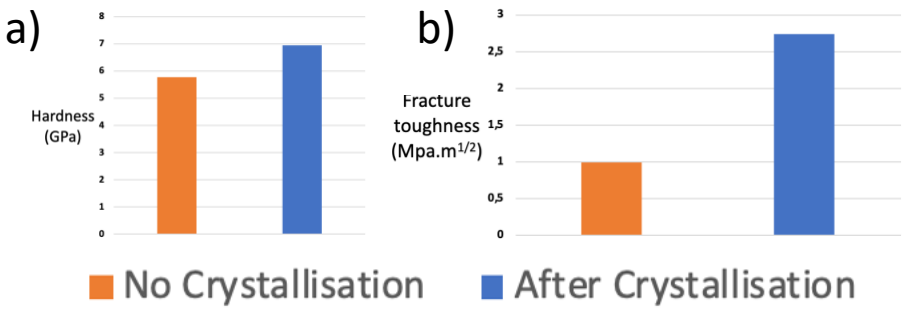

Figure 5.4: a) Hardness and b) Fracture toughness of cast pyrophyllite samples (without zirconia) before and after crystallisation.

For the crystallised samples the hardness obtained was comparable to both the industrial standard and measured hardness of basalt (Table 4.4). The fracture toughness of these samples was also significantly higher than the fracture toughness of the cast basalt tiles (Table 4.4). As discussed however in Section 5.2.1, the lengthy crystallisation profile required was fairly typical of anorthite based ceramics which are known to be difficult to crystallise and usually require the addition of nucleating agents for crystallization which was in agreement with the work by Lo, (Lo, et al., 2002).

With the introduction of zirconia as the nucleating agent the required time and steps for successful crystallisation were reduced (Table 4.3). The samples produced, however showed a slight decrease in the measured hardness with the initial introduction of the zirconia additive (Figure 5.5). The decrease in hardness with the introduction of zirconia was attributed to the morphological change in the resultant crystallised samples. Introducing zirconia changed the dominant phase (Figure 4.13) from being the harder anorthite phase (7,1 GPa) (Harabi, et al., 2017) to the softer gehlenite (5,2 GPa) (Teixeira, et al., 2014).

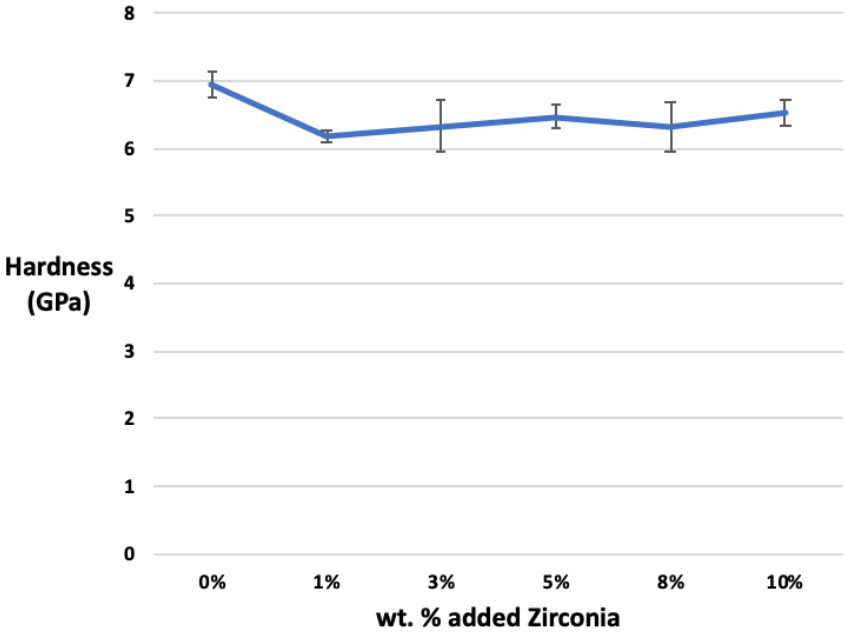

Figure 5.5: Hardness values of cast samples crystallized with added zirconia.

Further increases in the zirconia content (Figure 5.5) caused a slight though statistically insignificant increase in the hardness with increased zirconia, as shown by the error bars in the graph. Based on phase analysis in Section 5.2.1 this could also be attributed to the decrease in gehlenite no longer being the dominant phase with increased zirconia, with anorthite and wollastonite instead becoming the more prominent phases.

The effect of increasing zirconia content on the Fracture toughness is shown in Figure 5.6. An inverse and negative effect was produced with increased zirconia content. This was because the smaller grains of wollastonite and gehlenite which increased in population with increased zirconia encouraged crack propagation as opposed to the long needle like grains in the samples with less zirconia content as was also found by (Eberhardt, et al., 1999). The initial decrease in fracture toughness with the addition of 1 wt. % zirconia was very significant but thereafter further additions of zirconia up to 10 wt. % did not show such a dramatic toughness decrease although a small decreasing trend was observed.

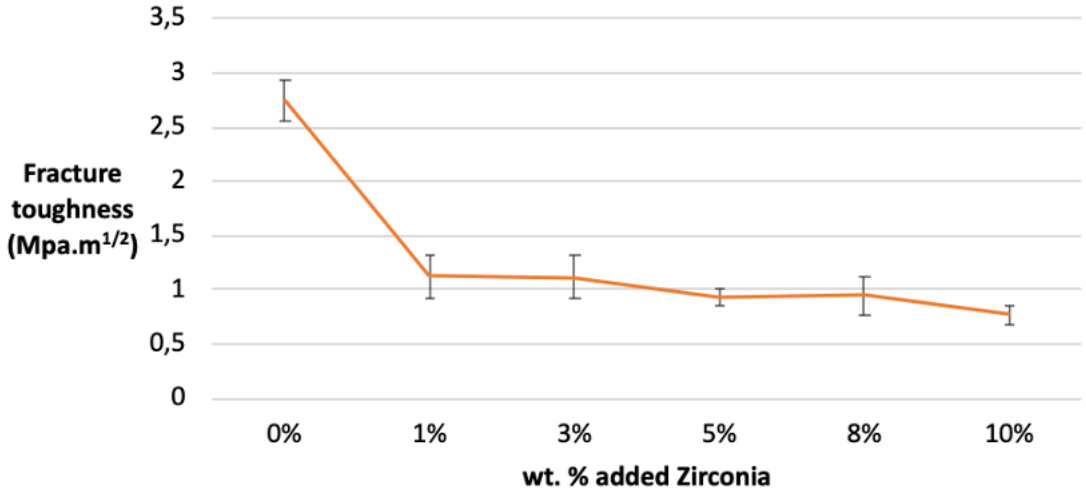

Figure 5.6: Fracture toughness of cast samples crystallized with added zirconia.

This decreased fracture toughness is more clearly shown in SEM images of the indentations made in the samples (Figure 5.7). As the zirconia content increased the samples became more brittle (Table 4.5) and the cracks around the hardness indent became longer and wider. The first sample with 1 wt. % zirconia (Figure 5.7 a) showed small sub-micron cracks clustered around the diamond indentation. Figure 5.7 b) with 3 wt. % zirconia showed more significant cracks of up to 1 micron in width radiating from the points of the diamond indentation. Of note in this image was that a corner of the diamond indenter was not fully impressed and this resulted in a variance in the results for this sample which had the highest hardness of all the samples measured hardness values (Figure 5.6). The final fracture toughness values however were comparable to the results obtained for the other samples doped with zirconia.

Similarly, the crack in structure in the top right-hand side of Figure 5.7 c) was also notable, however, it is sufficiently far from the indentation site not to affect the results as no cracks were deflected by it. This sample doped with 5 wt. % zirconia and showed more pronounced cracks of up to 1,5 microns width at the vertices of the diamond indentation. The 10 wt. % zirconia shows significant cracks that are 340 microns in length and approximately 3 microns in width at the root.

From the above observations it was established that increasing the zirconia content of the samples increased their hardness and decreased their fracture toughness after crystallisation. Banijamali et al. concluded that the increased presence of Zr^{4+} ions increases the strength from a hardness point of view (Banijamali, et al., 2009). The fracture toughness on the other hand was decreased due to the finer structure resulting in a lack of various strengthening mechanisms such as crack pinning and crack deflection (Banijamali, et al., 2009).

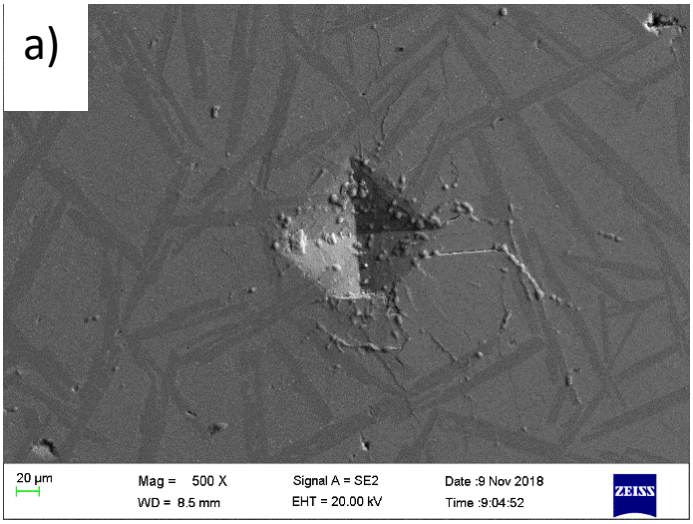

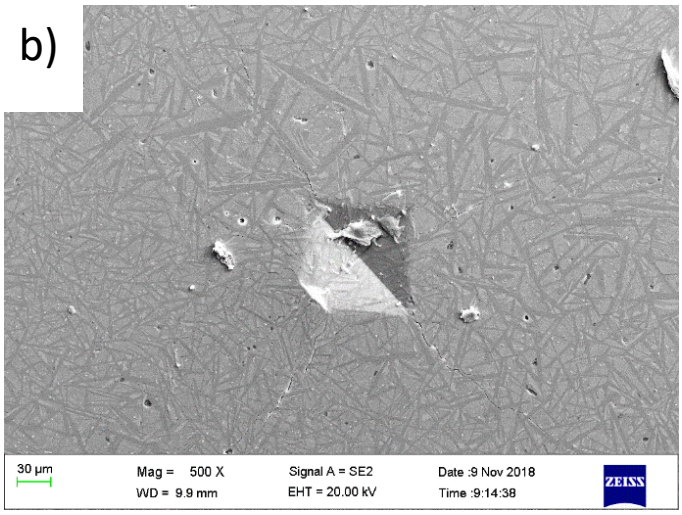

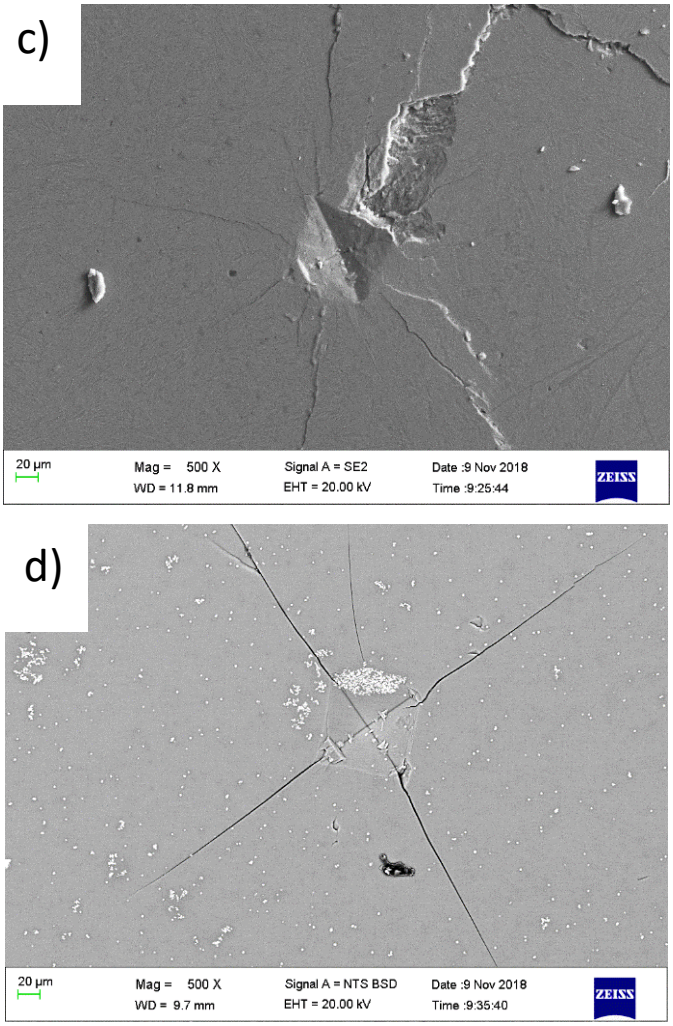

Figure 5.7: SEM Micrographs of indentations made to crystallized cast pyrophyllite with added zirconia of a) 1 wt. %, b) 3 wt. %, c) 5 wt. % and d) 10 wt. %.

The increase in the crystallisation time at 1100°C from 2 to 4 hours resulted in statistically insignificant changes in the density, hardness and fracture toughness (Table 4.6 & Figure 5.8). This is based on the small but overlapping error bars for the hardness and the significantly large but overlapping error bars found for the toughness measurements. This implied that the material was fully crystallised after 2 hours. The XRD patterns produced correlated to this, with gehlenite being the major crystalline phase for all three crystallisation times (Figure 4.23). SEM imagery also showed minor changes in the micrographs produced (Figure 4.22). Similarly, at higher zirconia contents Feng et al. also found little effect on crystallisation and instead observed a relatively small gain in the crystallization at low temperatures (Feng, et al., 2005).

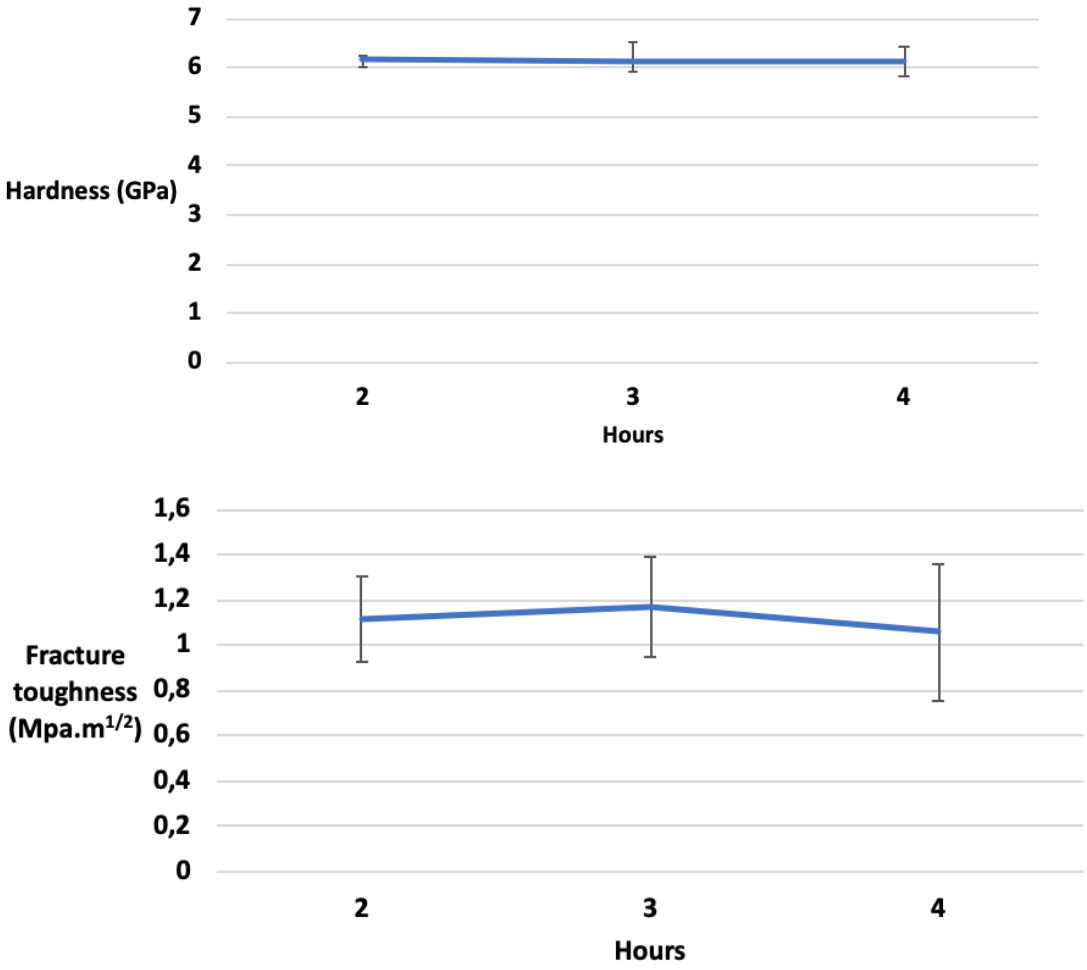

Figure 5.8: Mechanical properties of crystallized cast pyrophyllite with added 1% zirconia and heated at 1100°C from 2 to 4 hours.

CHAPTER 6: CONCLUSION

Cast pyrophyllite samples of comparable fracture toughness to cast basalt were successfully produced using calcium oxide additions to lower viscosity and casting temperature to 1400°C, approximately 350°C lower than the melting point of pyrophyllite. The cast material produced was transparent and yellow green in colour. Due to the material formed being an anorthite based a calcium alumino silicate, which are commonly difficult to crystallise the material was amorphous which meant it had a lower hardness when compared to basalt.

Crystallized cast pyrophyllite samples of comparable hardness and superior fracture toughness to cast basalt were further produced by implementing 2 additional heating and cooling cycles. The resultant material had a greenish white opaque appearance and a density of 2,89±0,09 g/cm^3 with a fracture toughness 1,8 Mpa.m$^{1/2}$ higher than that of cast basalt.

Zirconia was successfully used as a nucleating agent to reduce the complexity of crystallising the cast samples down to a single heating step at 1100°C for 2 hours. Samples were successfully produced using 1, 3, 5, 8 and 10 wt. % added zirconia. At 1 wt. % zirconia however, both the hardness and fracture toughness values obtained decreased as compared to samples crystallised without zirconia. By adding up to 10 wt. % zirconia hardness values were gradually increased again but fracture toughness values decreased. At 10wt. % zirconia addition, the material becomes amorphous, indicating the dissolution of the majority of the ZrO_2 particles in the silicate matrix and a reduction in the melting point of the mix to 1100°C.

In addition to this, further work may be done to explore additional additives to eliminate the nucleation step entirely and produce crystallised samples as cast. This study recommends future work with similar testing apparatus to be done using crucibles with

generally thin walls during as these experienced the least amount of thermal shock during the casting phase this study.

CHAPTER 7: REFERENCES

- Abdul-Azam, F. A. et al., 2017. Compression Behaviour of Pseudowollastonite-Mullite Biocomposite. *International Journal of Current Science, Engineering & Technology,* 1(SI), pp. 313-318.
- Adcock, R., 1853. Nouvelle matiere fusible.. *Le genie industriel,* 5(111), p. 239.
- Anstis, G. R., Chantikul, P., Lawn, B. R. & Marshall, D. B., 1981. A Critical Evaluation of Indentation Techniques for Measuring Fracture Toughness: I, Direct Crack Measurements. *Journal of the American Ceramic Society,* 64(9), pp. 533-538.
- Auborg, P. & Wolf, W., 1997. Glass fibers. In: D. Boyd & J. MacDowell, eds. *Commercial Glasses, Advances in Ceramics.* Ohio: The American Ceramic Society, pp. 51-64.
- Augustyn, A. et al., 2018. *Monoclinic system.* [Online] Available at: https://www.britannica.com/science/monoclinic-system [Accessed 26 December 2020].
- Ball, R. G. J., Mignanelli, M. A., Barry, T. I. & Gisby, J. A., 1993. The calculation of phase equilibria of oxide core-concrete systems. *Journal of Nuclear Materials,* 201(2), pp. 238-249.
- Banijamali, S., Yekta, B. E., Rezaie, H. & Marghussian, V., 2009. Crystallization and sintering characteristics of CaO–Al2O3–SiO2 glasses in the presence of TiO2, CaF2 and ZrO2. *Thermochimica Acta,* Volume 488, pp. 60-65.
- Barresi, T., Nelson, J. L. & Dostal, J., 2014. Geochemical constraints on magmatic and metallogenic processes: Iskut River Formation, volcanogenic massive sulfide-hosting basalts. *Canadian Journal of Earth Sciences,* 52(1).
- Bentayeb, A. et al., 2003. XRD and HRTEM characterization of pyrophyllite from Morocco and its possible applications. *Applied Clay Science,* April, 22(5), pp. 211-221.
- Bhadauria, N., Pandey, S. & Pandey, P., 2020. Wear and enhancement of wear resistance – A review. *Materials Today: Proceedings.*
- Bhatty, M. S. Y., Gard, I. J. A. & Glasser, F. P., 1970. Crystallization of anorthite from CaO-AI O -Si02 glasses. *MINERALOGICAL MAGAZINE,* 37(291), pp. 780-789.
- Bickford, D. F. & Jantzen, C. M., 1986. Devitrification of defense nuclear waste glass: role of melt insolubles. *Journal of Non-Crystalline Solids,* Volume 84, pp. 299-307.
- BMW Steels Ltd, n.d. *BMW Steels Ltd.* [Online] Available at: http://www.bmwsteels.com/bmw-profile-new-1.pdf [Accessed 25 October 2018].
- Bownes, F. F. & Beadle, J. D., 1971. Sand Casting. In: *Castings.* London: Macmillan Publishers Limited, pp. 63-64.
- Brandt, M. J. & Ratnayaka, D. D., 2017. Chemical Storage, Dosing and Control. In: *Twort's Water Supply (Seventh Edition).* Amsterdam: Elsevier.

- Brindley, G. W. R., 1970. Monoclinic and triclinic forms of pyrophyllite and pyrophyllite anhydride. *Am. Miner.*
- Brittain, H. G. & Bruce, R. D., 2006. Chapter 4 Thermal analysis. In: S. Ahuja & N. Jespersen, eds. *Comprehensive Analytical Chemistry.* s.l.:s.n., pp. 63-109.
- Campbell, J. S., 1984. *Principles of manufacturing materials and processes.* London: McGraw-Hill Education.
- Ceylan, U., Akin, I. & Goller, G., 2010. The Effect of Zirconia Addition on Crystallization Behaviour and Machinability of Potassium Mica and Fluorapatite Glass- Ceramics. *High Temperature Materials and Processes,* 29(4), pp. 305-311.
- Chartrand, P. & Pelton, A. D., 1999. Coupling phase Diagrams Thermochem. *Calphad,* 23(2), pp. 219-130.
- Chunlin, C., 2015. Application of MPE Model to Iron Ore Sintering, Ironmaking and Steelmaking Processes. *steel research international,* 86(6), pp. 612-618.
- Davis, J., 2010. Surface engineering for corrosion and wear resistance. In: *Surface engineering for corrosion and wear resistance.* Materials Park, OH: ASM International, pp. 1-10.
- Dong, H., 2010. 3 - Tribological properties of titanium-based alloys. *Surface Engineering of Light Alloys Aluminium, Magnesium and Titanium Alloys ,* pp. 50-58.
- Duan, R. & Liang, K., 1998. A study on the crystallization of CaO-Al2O3-SiO2 system glasses. *Journal of Material Processing Technology ,* Volume 75, pp. 253-239.
- Eberhardt, E., Stimpson, B. & Stead, D., 1999. Effects of Grain Size on the Initiation and Propagation Thresholds of Stress-induced Brittle Fractures. *Rock Mechanics and Rock Engineering,* 32(2), pp. 81-99.
- Feng, H., Feng, N. & Guang-hui, L., 2005. Influence of ZrO2 on sintering and crystallization of CaO-Al203-SiO glass-ceramics. *J. CENT. SOUTH UNIV. TECHNOL.,* 12(5), pp. 511-514.
- Gaidoumi, A. E. et al., 2019. Catalytic Efficiency of Cu-Supported Pyrophyllite in Heterogeneous Catalytic Oxidation of Phenol. *Arabian Journal for Science and Engineering.*
- Galan, I., Glasser, F. P. & Andrade, C., 2013. Calcium carbonate decomposition. *Journal of Thermal Analysis and Calorimetry,* 111(2), pp. 1197-1202.
- Garcia-Cordovilla, C., Narciso, J. & Louis, E., 1996. Abrasive wear resistance of aluminium alloy /ceramic particulate composites. *Wear,* Volume 192, pp. 170-177.
- Groover, M. P., 2011. In: *Fundamental of modern manufacturing Materials, Processes and systems.* s.l.:John Wiley .
- Gruner, J. W., 1934. The crystal structures of talc and pyrophyllite. *Zeitschrift für Kristallographie - Crystalline Materials,* 88(1-6), pp. 412-419.
- Guedes, M., Ferro, A. & Ferreira, J., 2001. Nucleation and crystal growth in commercial LAS compositions. *Journal of the European Ceramic Society,* 21(9), pp. 1187-1194.

- Han, Z. et al., 2013. Erosion-Resistant Surfaces Inspired by Tamarisk. *Journal of Bionic Engineering,* 10(4).
- Harabi, A. et al., 2017. Mechanical properties of anorthite based ceramics prepared from kaolin DD2 and calcite. *Cerâmica,* Volume 63, pp. 311-317.
- Harben, P., 1995. Pyrophyllite. In: *Industrial Minerals HandyBook.* London: Industrial Minerals Information, pp. 143-145.
- Inglesi, R. & Pouris, A., 2010. Forecasting electricity demand in South Africa: a critique of Eskom's projections. *South African Journal of Science,* 106(2), pp. 50-53.
- Jackson, M., 1992. A review of the late archean volcan-sedimentary dominion group and implications for the tectonic setting of the witwatersrand supergroup, south africa. *Journal of earth sciences,* pp. 86-169.
- Jia, D. & Kriven, W. M., 2007. Sintering Behavior of Gehlenite, Part II. Microstructure andMechanical Properties. *Journal of the American Ceramic Society,* 90(9), p. 2766–2770.
- Kanegsberg, B. & Kanegsberg, E., 2011. Particle Analysis. In: B. Kanegsberg & E. Kanegsberg, eds. *Handbook for Critical Cleaning: Applications, processes, and controls.* 2nd Edition ed. s.l.:CRC Press, p. 142.
- Karamanov, A., Arrizza, L. & Ergul, S., 2009. Sintered material from alkaline basaltic tuffs. *Journal of the European Ceramic Society,* Volume 29, p. 595–601.
- Keenan, M. J. et al., 1997. Comparison of Bone Density Measurement Techniques: DXA and Archimedes' Principle. *Journal of Bone and Mineral Research,* 12(11), pp. 1903-1907.
- Kingery, W., Vandiver, P. & Huang, I., 1983. Liquid–liquid immiscibility and phase separation in the quaternary systems K2O– Al2O3 –CaO–SiO2 and Na2O–Al2O3 –CaO–SiO2. *Journal of Non-Crystalline Solids,* Volume 54, p. 163.
- Ko, P., 1987. Metallic wear a review with special references to vibration- induced wear in power plant components. *Tribology International,* 20(2), pp. 66-78.
- Kopecky, L., 1965. The cast basalt industry. *Annals New York Academy of Sciences,* 123(2).
- Kwon, K. D. & Newton, A. G., 2016. Structure and stability of pyrophyllite edge surfaces: Effect of temperature and water chemical potential. *Geochimica et Cosmochimica Acta,* Volume 190, pp. 100-114.
- Lederer, K., Deckwerth, M. & Russel, C., 1998. Zirconia-doped Mg-Ca-A1-Si-O-N glasses: crystallization. *Journal of Non-Crystalline Solids,* Volume 224, pp. 109-121.
- Lee, K., Hirschfeld, D. & Brown, J., 1993. In situ reinforced glass ceramic in the lithia-alumina-silica system. *Ceramic Transactions: Nucleation and Cristalization in Liquids and Glasses,* Volume 30, p. 293.
- Li, L., Tang, Z., Sun, W. & Wang, P., 1999. Phase diagram estimation of the Al2O3–SiO2–Gd2O3 system. *Physics and Chemistry of Glasses,* 40(3), pp. 126-129.
- Lo, C.-L., Duh, J.-G. & Chiou, B.-S., 2003. Low temperature sintering and crystallisation behaviour of low loss anorthite-based glass-ceramics. *JOURNAL OF MA TERIALS SCIENCE,* Volume 38, pp. 693-698.

- Lo, C.-L., Duh, J.-G., Chiou, B.-S. & Lee, W.-H., 2002. Microstructure characteristics for anorthite compositeglass with nucleating agents of TiO2undernon-isothermal crystallization. *Materials Research Bulletin ,* Volume 37, pp. 1949-1960.
- Locsei, B., 1970. *Molten Silicates and their Properties.* Budapest: Akademiai Kiado.
- Mallick, P., 2000. Polymer Matrix Composites. In: *Comprehensive Composite Materials.* Amsterdam: Elsevier.
- Mao, H., Hillert, M., Selleby, M. & Sundman, B., 2006. Thermodynamic Assessment of the CaO–Al2O3–SiO2 System. *Journal of the American Ceramic Society,* 89(1), pp. 298-308.
- Marques, V. et al., 2006. Low temperature synthesis of anorthite based glass-ceramics viasintering and crystallization of glass-powder compacts. *Journal of the European Ceramic Society,* Volume 26, pp. 2503-2510.
- Medvedovski, E., 2001. Wear-resistant engineering ceramics. *Wear,* Volume 249, pp. 821-828.
- Micronz Ltd, 2019. *Wear Resistant Parts.* [Online] Available at: http://www.micronz.co.uk/dr-kaiser/wear-resistant-parts [Accessed 18 January 2020].
- Mirhadi, B. & Mehdikhani, B., 2011. Crystallization behavior and microstructure of (CaO·ZrO2·SiO2)–Cr2O3 based glasses. *Journal of Non-Crystalline Solids,* Volume 357, p. 3711–3716.
- Motzfeldt, K., 1955. The Thermal Decomposition of Sodium Carbonate by the Effusion Method. *The Journal of Physical Chemistry,* 59(2), pp. 139-147.
- Mukhopadhyay, T., Ghatak, S. & Maiti, H., 2010. Pyrophyllite as raw material for ceramic applications in the perspective of its pyro-chemical properties. *Ceramics International,* 26(3), pp. 909-916.
- Multotec, 2019. *Multotec.* [Online] Available at: https://www.multotec.com/en/cast-basalt-wear-resistant-material [Accessed 8 March 2020].
- Myra, C., 2016. *Use of Ceramics as Good Refractory Material.* [Online] Available at: http://forums.jlconline.com/forums/forum/jlc-online-expert-forums/ceramic-tile/1063105-use-of-ceramics-as-good-refractory-material [Accessed 2 July 2017].
- Nelson, S. A., 2014. *Weathering & Clay Minerals.* [Online] Available at: https://www.tulane.edu/~sanelson/eens211/weathering&clayminerals.htm [Accessed 14 March 2020].
- NGL, 2020. *Pyrophyllite.* [Online] Available at: https://nationalgemlab.in/25291-2/ [Accessed 8 March 2020].
- Nichols, L., 2019. *Melting Point Theory.* [Online] Available at: https://chem.libretexts.org/Bookshelves/Organic_Chemistry/Book%3A_Organi

c_Chemistry_Lab_Techniques_(Nichols)/6%3A_Miscellaneous_Techniques/6.1%3A_Melting_Point/6.1C%3A__Melting_Point_Theory
[Accessed 15 January 2020].

- Nordlie, B., 1989. Eutectic melting. In: Petrology. In: *Encyclopedia of Earth Science.* Boston: Springer.
- Partridge, G., 1994. An overview of glass ceramics: Part 1 — development and principal bulk applications. *Glass Technology,* 35(3), pp. 116-127.
- Pawelec, B. & Fierro, J., 2003. Applications to Inorganic and Miscellaneous Materials. In: *Handbook of Thermal Analysis and Calorimetry.* s.l.:s.n.
- Pérez-Maqueda, L. et al., 1993. Thermal analysis of ground kaolinite and pyrophyllite. *Journal of thermal analysis,* 29(8-9), pp. 1055-1067.
- Pérez-Rodríguez, J. L., Madrid Sánchez del Villar, L. & Sánchez-Soto, P., 1988. Effects of dry grinding on pyrophyllite. *Clay Minerals,* 23(4), pp. 399-410.
- PerkinElmer, Inc., 2015. *Thermogravimetric Analysis (TGA).* [Online] Available at: https://www.perkinelmer.com/lab-solutions/resources/docs/FAQ_Beginners-Guide-to-Thermogravimetric-Analysis_009380C_01.pdf
[Accessed 11 January 2020].
- Prime, B. R. & Bair, H. E., 2009. THERMOGRAVIMETRIC ANALYSIS (TGA). In: J. D. Menczel & R. B. Prime, eds. *Thermal Analysis of Polymers: Fundamentals and Applications.* s.l.:John Wiley & Sons, Inc, p. 241.
- Rao, T. R., 1996. Kinetics of calcium carbonate decomposition. *Chem. Eng. Technol,* Volume 19, pp. 373-377.
- Ribbe, F., 1914. *Manufacture of industrial objects from volcanic or other fusible rock..* United States, Patent No. US1108007A.
- Rieger, K., 1997. Pyrophyllite. Minerals review. *American Ceramic Society,* 76(6), pp. 124-125.
- Rocha-Rangel, E., 2011. Fracture Toughness Determinations by Means of Indentation Fracture. In: D. J. Cuppoletti, ed. *Nanocomposites with Unique Properties and Applications in Medicine and Industry.* México City: Universidad Politécnica de Victoria, pp. 21-37.
- Sanchez-Soto, P. & Perez-Rodriguez, J., 1989. Thermal analysis of pyrophyllite transformations. *Thermochimica Acta,* 138(2), pp. 267-276 .
- Schultz, R. A., 1993. Brittle strength of basaltic rock masses with applications to Venus. *Journal of geophysical research planets,* 98(E6), pp. 10883-10895.
- Sharma, S. K., 2010. *Manufacturing Processes (as Per The Uptu New Syllabus).* New Delhi: I.K. International Pub..
- Sheth, H. C., Torres-Alvarado, I. S. & Verma, S. P., 2002. What Is the “Calc-alkaline Rock Series”?. *International Geology Review,* Volume 44, p. 86–701.
- SigmaAldrich, 2020. *SigmaAldrich.* [Online] Available at: https://www.sigmaaldrich.com/catalog/product/aldrich/481807?lang=en&region=ZA
[Accessed 8 March 2020].

- Singha, S. K. & Singh, S. J., 2015. ANALYSIS AND OPTIMIZATION OF SAND CASTING DEFECTS WITH THE HELP OF ARTIFICIAL NEURAL NETWORK. *International Journal of Research in Engineering and Technology,* 4(5), pp. 2319-1163.
- Švec, P., Brusilová, A. & Kozánková, J., 2008. EFFECT OF MICROSTRUCTURE AND MECHANICAL PROPERTIES ON WEAR RESISTANCE OF SILICON NITRIDE CERAMICS. *Materials Engineering,* 16(1), pp. 34-40.
- Teixeira, S. R. et al., 2014. Characterization of a wollastonite glass-ceramic material prepared using sugar cane bagasse ash (SCBA) as one of the raw materials. *Materials Characterization,* Volume 98, p. 209–214.
- The University of Auckland, 2005. *Basalt.* [Online] Available at: https://flexiblelearning.auckland.ac.nz/rocks_minerals/rocks/basalt.html [Accessed 15 January 2020].
- Uygun, A. & Solakoglu, E., 2002. GEOLOGY AND ORİGİN OF THE PYROPHYLLITE - DEPOSİTS IN THE PÜTÜRGE MASSIF (MALATYA - EASTERN TURKEY). *Bulletin of The Mineral Research and Exploration,* Volume 123, pp. 13-19.
- Voldan, J., 1964. Prehled o vyvoji a soucasnem stavu petrurguckeho prumyslu. *Informativni prehled,* 7(1).
- Wang, G., Fu, K., Wang, S. & Yang, B., 2020. Optimization of mechanical and tribological properties of a dental SiO2–Al2O3–K2O–CaO–P2O5 glass-ceramic. *Journal of the Mechanical Behavior of Biomedical Materials,* Volume 102.
- Warren, B. & Pincus, A., 1940. Atomic consideration of immiscibility in glass systems. *Journal of the American Ceramic Society,* Volume 23, p. 301.
- Winkler, H., 2005. Renewable energy policy in South Africa : policy options for renewable electricity. *Energy Policy,* 33(1), pp. 27-38.